Applications of dynamic photoluminescence measurements to metallised silicon solar cells

Robert William Dumbrell

A thesis in fulfilment of the requirements for the degree of

Doctor of Philosophy

School of Photovoltaic and Renewable Energy

Faculty of Engineering

May 2019

Thesis/Dissertation Sheet

Surname/Family Name	:	**DUMBRELL**
Given Name/s	:	**ROBERT WILLIAM**
Abbreviation for degree as give in the University calendar	:	**PhD**
Faculty	:	**ENGINEERING**
School	:	**PHOTOVOLTAIC AND RENEWABLE ENERGY**
Thesis Title	:	**Applications of dynamic photoluminescence measurements to metallised silicon solar cells**

Abstract 350 words maximum: (PLEASE TYPE)

Deployment of photovoltaic power generation is expected to accelerate over the next 10-20 years under the influence of reduced cost and increased power conversion efficiency. An important limiting factor to cell efficiency is carrier recombination at metal contacts, thus, to aid further improvements, an accurate and reliable measurement technique for this recombination is required.

This recombination is challenging to measure in isolation from other sources because measurements at the cell terminals convolve many types of recombination into a single measurement, and simplified test structures are not easily measured using traditional photoconductance based techniques for surface recombination measurement because the metal interferes with the conductance measurement. Photoluminescence (PL) measurements are ideally suited to studying recombination of metallised cells and test structures because they are contactless, applicable to arbitrarily size areas and minimally influenced by the presence of metal. Following other studies which apply PL imaging to this problem, this thesis investigates dynamic PL measurement techniques which are faster, simpler and do not require external calibration.

A dynamic PL measurement system is first developed and tested. The system is then used for detailed investigation of silicon-metal interface recombination.

A detailed study comparing dynamic open circuit voltage measurements (called Suns-V_{oc}) and implied open circuit voltage measurements obtained from the developed PL system (called Suns-PL) shows that Suns-V_{oc} data fail to accurately represent all of the recombination in a device at high illumination conditions due to lateral resistive effects but Suns-PL is unaffected by this effect and thus is well suited to measuring metallised cells and test structures.

Metal contact recombination measurements using dynamic PL and the subsequent data analysis are also investigated. It is concluded that because of the non-uniform recombination introduced by metal contacts, excess carriers tend to become non-uniformly distributed, and analysis techniques that assume uniform distribution are inaccurate. Analysis techniques that are based on the simulating the full device geometry such as the methods presented in this thesis can better account for the non-uniformity and are thus more accurate.

FOR OFFICE USE ONLY   Date of completion of requirements for Award:

ORIGINALITY STATEMENT

'I hereby declare that this submission is my own work and to the best of my knowledge it contains no materials previously published or written by another person, or substantial proportions of material which have been accepted for the award of any other degree or diploma at UNSW or any other educational institution, except where due acknowledgement is made in the thesis. Any contribution made to the research by others, with whom I have worked at UNSW or elsewhere, is explicitly acknowledged in the thesis. I also declare that the intellectual content of this thesis is the product of my own work, except to the extent that assistance from others in the project's design and conception or in style, presentation and linguistic expression is acknowledged.'

Signed:…………………………………………………

Date:…………………………………………………

INCLUSION OF PUBLICATIONS STATEMENT

UNSW is supportive of candidates publishing their research results during their candidature as detailed in the UNSW Thesis Examination Procedure.

Publications can be used in their thesis in lieu of a Chapter if:

- The student contributed greater than 50% of the content in the publication and is the "primary author", ie. the student was responsible primarily for the planning, execution and preparation of the work for publication
- The student has approval to include the publication in their thesis in lieu of a Chapter from their supervisor and Postgraduate Coordinator.
- The publication is not subject to any obligations or contractual agreements with a third party that would constrain its inclusion in the thesis

Please indicate whether this thesis contains published material or not.

☐   *This thesis contains no publications, either published or submitted for publication*

☒   *Some of the work described in this thesis has been published and it has been documented in the relevant Chapters with acknowledgement*

☐   *This thesis has publications (either published or submitted for publication) incorporated into it in lieu of a chapter and the details are presented below*

CANDIDATE'S DECLARATION

I declare that:

- I have complied with the Thesis Examination Procedure
- where I have used a publication in lieu of a Chapter, the listed publication(s) below meet(s) the requirements to be included in the thesis.

Name	Signature	Date (dd/mm/yy)

To Susu and Audrey

ABSTRACT

Deployment of photovoltaic power generation is expected to accelerate over the next 10-20 years under the influence of reduced cost and increased power conversion efficiency. An important limiting factor to cell efficiency is carrier recombination at metal contacts, thus, to aid further improvements, an accurate and reliable measurement technique for this recombination is required.

This recombination is challenging to measure in isolation from other sources because measurements at the cell terminals convolve many types of recombination into a single measurement, and simplified test structures are not easily measured using traditional photoconductance based techniques for surface recombination measurement because the metal interferes with the conductance measurement. Photoluminescence (PL) measurements are ideally suited to studying recombination of metallised cells and test structures because they are contactless, applicable to arbitrarily size areas and minimally influenced by the presence of metal. Following other studies which apply PL imaging to this problem, this thesis investigates dynamic PL measurement techniques which are faster, simpler and do not require external calibration.

A dynamic PL measurement system is first developed and tested. The system is then used for detailed investigation of silicon-metal interface recombination.

A detailed study comparing dynamic open circuit voltage measurements (called Suns-V_{oc}) and implied open circuit voltage measurements obtained from the developed PL system (called Suns-PL) shows that Suns-V_{oc} data fail to accurately represent all of the recombination in a device at high illumination conditions due to lateral resistive effects but Suns-PL is unaffected by this effect and thus is well suited to measuring metallised cells and test structures.

Metal contact recombination measurements using dynamic PL and the subsequent data analysis are also investigated. It is concluded that because of the non-uniform recombination introduced by metal contacts, excess carriers tend to become non-uniformly distributed, and analysis techniques that assume uniform distribution are inaccurate. Analysis techniques that are based on the simulating the full device geometry such as the methods presented in this thesis can better account for the non-uniformity and are thus more accurate.

ACKNOWLEDGEMENTS

CONTENTS

CHAPTER 1: INTRODUCTION

1.1 MOTIVATION

The global energy system is presently in transition from a fossil fuel based system towards a renewable energy based system. Dramatic cost reductions (e.g. approximately 70 % reduction in crystalline silicon (Si) photovoltaic (PV) module prices since January 2013 [1]) have seen PV electricity emerge as a leader in this transition. From a base of approximately 300 GW of installed capacity in 2018, global PV capacity is expected to grow to between 2-4 TW by 2040 according to conservative estimates by the International Energy Agency [2]. This growth will be fuelled by numerous improvements across the PV value chain. To drive the necessary cell efficiency improvements, the International Technology Roadmap for Photovoltaics predicts that front and rear surface saturation current density ($J_{0,front}$ and $J_{0,rear}$), key metrics for the cell surface recombination, must reduce by approximately a factor of three for p-type cells and a factor of between three and four for n-type cells in the next ten years (see Fig. 1-1) [1].

Recombination losses at the metal contacts on the cell surfaces are an important limiting factor for overall surface recombination reduction and further efficiency improvements [3], [4]. Common approaches to mitigate these losses are to either reduce the contact area fraction [5] or passivate the contacted area [6]. Further improvements will be required to meet the ten year targets, which necessitates reliable and accurate methods for measuring such recombination. Investigation of such measurement techniques is the subject of this thesis.

1.2 CHARACTERISING RECOMBINATION IN CELLS

Quasi-steady-state photoconductance (QSSPC) lifetime is a widely used recombination characterisation technique in research and industry, and well suited to non-metallised samples [7]. However, it is difficult to use with metallised samples. Contacted techniques, like illumination intensity dependent open circuit voltage (Suns-V_{oc}) [8] can characterise overall cell recombination but are difficult to analyse with respect to specifically attributing recombination to certain parts of the cell, like metal contacts.

Photoluminescence (PL) measurements, the capture of characteristic radiation emitted when a sample is illuminated, are ideally suited to measuring this recombination because the measurement technique is contactless and easily applied to both metallised and unmetallised test structures and cells [9]. PL imaging is a well-established and powerful method of characterisation for solar cells because it shows poorly performing parts of

samples with high spatial resolution [10]. Several studies have shown useful approaches to studying metal induced surface recombination that use PL imaging [11]–[13]. Quasi-steady-state PL (QSSPL) uses a comparatively simpler measurement setup but has not been widely applied to surface recombination measurements. It uses the well-established theory of quasi-steady-state lifetime measurements [14] with extra attention paid to the calibration [15].
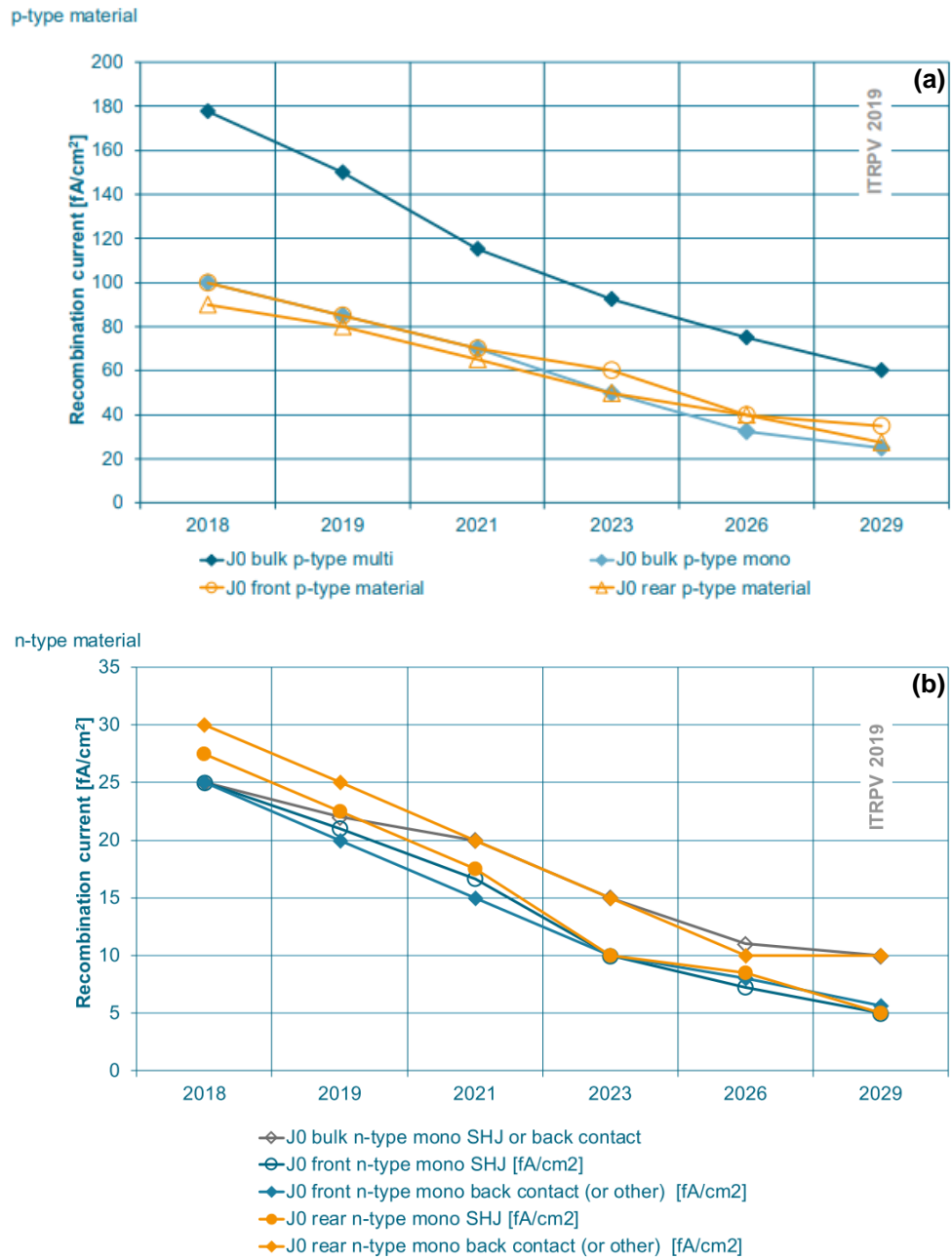
Fig. 1-1: Predicted change in recombination saturation densities for (a) p-type and (b) n-type cells for ten years to 2029. Reproduced from Ref. [1].

Each of the above mentioned characterisation techniques make assumptions about the uniformity of the voltage within a cell differently. QSSPL and QSSPC are area averaged techniques, so assume it is uniform everywhere. Suns-V_{oc} is a terminal measurement, so non-uniformity is ignored and only the terminal characteristics are measured. PL images capture lateral non-uniformity but average depth-wise non-uniformity.

The principal aim of this thesis is to investigate the use of QSSPL lifetime measurements for measuring recombination of metallised test structures and cells, with particular focus on measuring the surface recombination at the metal contact. In the context of accurate measurements of local surface recombination, a further objective of this thesis is to test the assumptions inherent in the various characterisation and analysis techniques through simulation and experiment and make specific recommendations about appropriateness of each technique for different sample designs.

1.3 THESIS OUTLINE

This thesis presents a simplified approach, which uses QSSPL. This approach combines the simplicity of the QSSPC approach with the versatility of PL.

Chapter 2 reviews and analyses these previously studied recombination measurements and the previously established QSSPL theory. A comparison between and evaluation of the various existing methods for metal surface recombination measurement is presented.

Chapter 3 outlines the development of the measurement instruments used for the experimental work. The instruments enable dynamic PL measurements such as QSSPL or Suns-PL to be performed on metallised test structure samples or cells. Dynamic calibration procedures are outlined, and validation experimental data are presented.

Chapter 4 presents a comparative study of PL and contacted Suns-V_{oc} measurements, with particular reference to their usage for lifetime measurements and surface recombination measurements of solar cells. It is shown that in many practical cases, Suns-V_{oc} measurements suffer from a lateral series resistance loss that leads to inaccuracies if the measurements are interpreted as lifetimes. This establishes the QSSPL approach as an appropriate technique to study surface recombination on metallised samples and cells.

Chapter 5 presents experimental measurements of metal induced surface recombination using the developed system. A technique to extract the metal recombination parameters from the measurements is demonstrated on a simplified test structure where one side of a sample is uniformly coated with metal. The measurements are supported by

simulations, which demonstrate the importance of accounting for the non-uniformity of the excess carrier density during the measurements.

Having established the extraction technique in the simplified case, Chapter 6 expands the technique to measurements of samples with partial metallisation, which are more representative of the likely use case of such measurements (e.g. front side metal fingers or rear side point contacts). Simulations are used to discuss and identify limitations of previously published approaches from the literature. Measurements with the new instrument and parameter extraction are demonstrated.

Chapter 7 summarises the conclusions of this thesis. It also presents future research directions.

CHAPTER 2: LITERATURE REVIEW

At a basic level, a solar cell operates under two competing processes, generation of charge carriers through absorption of photons, and recombination of those charge carriers through one of several different pathways. If charge carriers of opposite type are separated in the cell, a voltage results at the cell terminals and current will flow out of the cell to do work in an external circuit. All cell improvement activities can be classified as contributing to one these activities:

1. Maximising generation
2. Minimising recombination in the cell itself
3. Minimising transport losses to the external circuit

This thesis is primarily concerned with the second category, though some consideration will also be given to the third.

2.1 RECOMBINATION

Depending on the local conditions, the charge carrier density will tend to return to equilibrium as excess carriers annihilate each other by releasing their energy via one of several pathways. This process is called recombination. It is desirable for that energy to be released into an external circuit rather than back to the cell itself or the external environment. Minimising local recombination is an important goal of good cell design. This recombination is classified as either: ***intrinsic***, an unavoidable property of the absorber material itself; or ***extrinsic***, caused non-ideal material properties (e.g. structural or atomic defects) or non-ideal device properties (e.g. surface recombination, metal contact recombination).

Radiative recombination is an intrinsic process by which excess charge carriers recombine and spontaneously emit photons [16]. Because silicon has an indirect bandgap a relatively small proportion of carriers recombine this way [16]. Radiative recombination primarily occurs between the conduction and valence bands, though can also occur between any discreet energy levels in the bandgap if defect levels are present . Photon emission from radiative recombination between the conduction and valence bands under excitation is known as luminescence, an important measurable quantity for solar cell characterisation discussed further in Section 2.2.1.3.

Auger recombination is an intrinsic recombination process where an excited charge carrier transfers its energy to another carrier in the same band as it when it recombines

[16]. Auger recombination is the dominant form of intrinsic recombination in most Si solar cells under normal operation [17].

Most practical samples of silicon contain impurities or crystallographic defects that create allowed energy levels within the bandgap [16]. Recombination where a carrier recombines through these energy levels is known as trap-assisted or **Shockley-Read-Hall (SRH) recombination** [18], [19]. This recombination occurs within the bulk of a sample and at its surfaces.
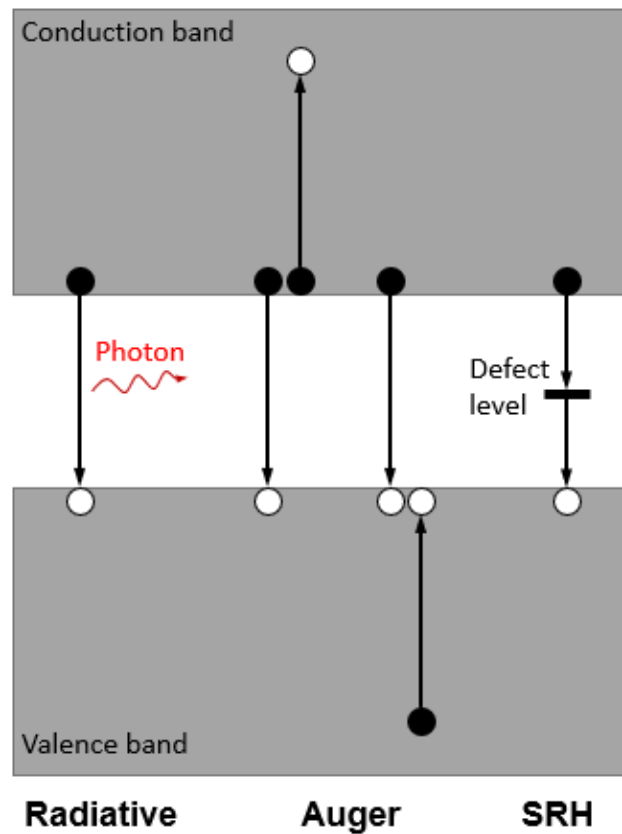
Fig. 2-1: Movement of electrons during recombination processes. Black dots indicate electrons, white dots indicate holes and arrows indicate electron movement. Adapted from Ref. [20].

SRH recombination in the bulk can be caused by the presence of non-silicon impurities in the lattice, e.g. metallic impurities like iron are known to be strong causes of bulk recombination [21]. Interruptions in the crystal lattice, like grain boundaries and dislocations in multicrystalline silicon are also causes of bulk recombination [22].

The surfaces of a silicon wafer, and any place where the silicon interfaces with another material (e.g. the metal contact of a solar cell) also create allowed energy states within the bandgap of silicon and thus creates another type of SRH recombination [23].

Engineering the cell surfaces and interfaces to reduce recombination is an important factor for solar cell efficiency improvement [24].

The recombination in a solar cell can be described in two different but related ways, either using a charge carrier model or a device model.

2.1.1 CHARGE CARRIER MODELS

Charge carrier models consider the generation and recombination of carriers and can be used to derive several useful parameters related to the recombination in any semiconductor sample. Here the basic equations that are used to derive these parameters are defined.

In thermal equilibrium, the equilibrium electron density (n_0) and the hole density (p_0) are defined by a single Fermi level (E_F) such that [16]

$$n_0 = N_c \exp\left(\frac{-[E_c - E_F]}{kT}\right)$$

$$(2\text{-}1)$$

$$p_0 = N_v \exp\left(\frac{-[E_F - E_v]}{kT}\right)$$

$$(2\text{-}2)$$

where N_c and N_v are the effective densities of state in the conduction and valence bands, E_c and E_v are the energy levels of conduction and valence band edges, k is Boltzmann's constant and T is the absolute temperature, respectively. The product of the equilibrium carrier densities defines a constant called the intrinsic carrier density (n_i) defined as [16]

$$n_i^2 = n_0 p_0 = N_c N_v \exp\left(\frac{-[E_c - E_v]}{kT}\right).$$

$$(2\text{-}3)$$

Under external excitation, excess carriers are generated such that [16]

$$np = [n_0 + \Delta n][p_0 + \Delta p] > n_i^2$$

$$(2\text{-}4)$$

where n and p are the total electron and hole densities, and Δn and Δp are the excess electron and hole densities, respectively.

Under these conditions electrons and holes are defined by separate distributions defined by *quasi* Fermi levels as

$$\Delta n = N_c \exp\left(\frac{-[E_c - E_{QF,e}]}{kT}\right)$$

$$(2\text{-}5)$$

$$\Delta p = N_v \exp\left(\frac{-[E_{QF,h} - E_v]}{kT}\right)$$
(2-6)

where $E_{QF,e}$ and $E_{QF,h}$ are the electron and hole quasi Fermi levels, respectively. Thus, Eq. (2-4) can be written as

$$np = n_i^2 \exp\left(\frac{\Delta E_{QF}}{kT}\right)$$
(2-7)

where $\Delta E_{QF} = E_{QF,e} - E_{QF,h}$ is the splitting of the quasi Fermi levels. When modelling solar cells, it is also instructive to define the **implied open circuit voltage**, iV_{oc} as

$$iV_{oc} = \frac{\Delta E_{QF}}{q} = \frac{kT}{q}\ln\left(\frac{np}{n_i^2}\right)$$
(2-8)

where q is the elementary charge. As will be discussed in Section 2.2.2.4, iV_{oc} is a useful parameter that can be directly measured from the luminescence of a sample and quantifies its recombination.

Typically, silicon solar cells are doped with impurities of either acceptor or donor type to a concentration several orders of magnitude higher than n_i. From Eq. (2-3), it can be seen that this has the effect of increasing the equilibrium concentration of one type of charge carrier (called the *majority carrier*) and reducing the equilibrium concentration of the opposite type charge carrier (called the minority carrier). Then under excitation conditions where $\Delta n = \Delta p$, Eq. (2-8) can be rewritten as

$$iV_{oc} = \frac{kT}{q}\ln\left(\frac{\Delta n[N_{dop} + \Delta n]}{n_{i,eff}^2}\right)$$
(2-9)

where Δn is the excess minority carrier density, N_{dop} is the dopant density (assuming 100% of dopants are ionised) and $n_{i,eff}$ is the effective intrinsic carrier density, which accounts for bandgap narrowing caused by the dopants, excess carriers and temperature.

Under steady-state excitation and open circuit conditions, generation (G) and recombination (U) rates are equal and a certain Δn is maintained. When recombination rate is modelled as a particle density per unit of volume per unit time this is expressed as [23]

$$G = U = \frac{\Delta n}{\tau_{eff}}$$
(2-10)

where τ_{eff} is called the effective lifetime and is a characteristic parameter that describes the total recombination occurring in a sample. The total recombination rate is given by the sum of each type of recombination and therefore τ_{eff} is given by the sum of the inverse lifetimes of each type of recombination [23].

$$\tau_{eff}^{-1} = \tau_{Auger}^{-1} + \tau_{rad}^{-1} + \tau_{ext}^{-1} \qquad (2\text{-}11)$$

where τ_{ext} is the lifetime of extrinsic types of recombination. Since τ_{eff} is the experimentally accessible parameter, this can allow each source of recombination to be quantified if the others are known. The different sources of recombination have differing carrier injection level dependencies, which further facilitates this separation of recombination sources. Equation (2-11) facilitates the concept of the lifetime limiting recombination. The recombination type with the lowest lifetime limits τ_{eff} and thus limits the overall voltage of the device. This concept is illustrated in Fig. 2-2 which shows that SRH recombination tends to limit τ_{eff} at lower injection levels, whereas Auger recombination limits τ_{eff} at high injection levels.
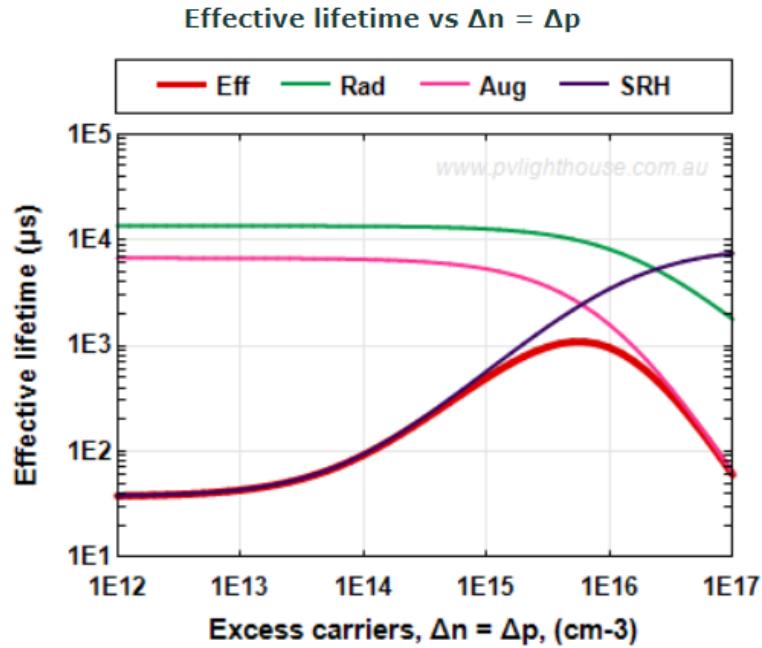
Fig. 2-2: Example injection dependent lifetimes of radiative [25], Auger [17] and SRH [18] recombination and the calculated τ_{eff} according to Eq. (2-11), simulated on PVLighthouse [26]. The SRH recombination is modelled using published defect parameters for the interstitial iron (Fe) defect [27] with Fe concentration of 10^{11} cm^{-3} in 1 Ωcm p-type Si.

Lifetimes represent recombination in terms of a volume, so are well suited to characterising bulk recombination. However, surface recombination is more commonly represented as a current density per unit area as [28]

$$J_{rec} = J_{0d} \left(\frac{n(x_d)p(x_d)}{n_{i,eff}^2} - 1 \right)$$ (2-12)

where J_{rec} is the recombination current density, J_{0d} is the **recombination saturation current density** and $n(x_d)$ and $p(x_d)$ are the minority and majority carrier densities at distance x_d from the front surface of a sample. This formulation is commonly used to model surface recombination where J_{0d} is the parameter that describes the recombination. In this thesis '*d*' is replaced with a meaningful letter based on what type of surface is being measured. E.g. J_{0e} is the emitter saturation current density, J_{0s} is the passivated surface saturation current density and J_{0m} is the metallised surface saturation current density.

An alternative model to describe the recombination current at a surface is as an **effective surface recombination velocity**, S_{eff}, given by [29]

$$J_{rec} = qS_{eff}\Delta n_d$$ (2-13)

where Δn_d is the excess carrier density at distance x_d. McIntosh and Black [30] reported that J_{0d} and S_{eff} can both be used to parametrise surface recombination but should be used in different cases. In this thesis, which is mostly concerned with measuring recombination at metal contacts (see Chapters 5 and 6), J_{0m} is the preferred parameter because S_{eff} is non-constant at intermediate and high level injection and can show some dependence on N_{dop}.

Finally it is noted that although the particle density lifetime model tends to be used to describe recombination in the bulk volume and the current density J_{0d} model of recombination is usually used to describe recombination into a two-dimensional surface, the parameters can be converted freely between each other but care must be taken to ensure Δn is uniform [31].

2.1.2 DEVICE MODELS

Another model of solar cell generation and recombination is formed based on considering measurements of the output current and voltage at the device terminals. In the ideal case a solar cell is described by [32]

$$J = J_L - J_0 \left[\exp\left(\frac{V}{kT/q} \right) - 1 \right]$$ (2-14)

where J_L is the light generated current density, J_0 is the saturation current density, V is the terminal voltage and J is the terminal current density. From this definition we can see that the first term (J_L) represents generation and the second term recombination.

Real solar cells are not ideal though so a lumped series resistance (R_s), lumped shunt resistance (R_{sh}) and an ideality factor (m) are added to the model to create the implicit equation [32]

$$J = J_L - J_0 \left[\exp\left(\frac{V + JR_s}{mkT/q}\right) - 1 \right] - \frac{V + JR_s}{R_{sh}}.$$

(2-15)

This is called the **one-diode model**, which separates losses into a recombination term and a shunt term. This model can be extended by dividing the recombination loss into ideal and non-ideal terms by introducing a second diode with m = 2, called the **two-diode model** [32],

$$J = J_L - J_{01} \left[\exp\left(\frac{V + JR_s}{kT/q}\right) - 1 \right] - J_{02} \left[\exp\left(\frac{V + JR_s}{2kT/q}\right) - 1 \right] - \frac{V + JR_s}{R_{sh}}$$

(2-16)

where J_{01} is the saturation current density of ideal recombination and J_{02} is the saturation current density of the $m = 2$ recombination. Depending on which model is used, it can be seen from the equations that the recombination in a device can be completely described by either J_0 and m or J_{01} and J_{02}.

2.2 CHARACTERISING RECOMBINATION

2.2.1 MEASURABLE QUANTITIES

2.2.1.1 OPEN CIRCUIT VOLTAGE

Several current-voltage (J-V) measurement techniques exist, the associated data can be fit using the device models from Section 2.1.2 such as light J-V, dark J-V and J_{sc}-V_{oc} as reported by Wolf and Rauschenbach [33]. The light and dark J-V measurements to some degree incorporate the non-idealities of the parasitic resistances, which makes isolation of the recombination characteristics difficult. However, V_{oc} measurements allow the lumped series resistance to be neglected. By setting $J = 0$ in Eq. (2-15) and assuming high R_{sh} such that the shunt term can be neglected, the open circuit voltage, V_{oc}, is defined as

$$V_{oc} = \frac{mkT}{q} \ln\left(\frac{J_L}{J_0} + 1\right)$$

(2-17)

This shows that it is directly related to J_0 and m and thus is a good metric for recombination in a device. Higher J_0 results in lower V_{oc}.

V_{oc} is also defined in terms of Δn at the junction underneath the metal contact of a cell as

$$V_{oc} = \frac{kT}{q} \ln\left(\frac{\Delta n(0)\left[N_{dop} + \Delta n(0)\right]}{n_{i,eff}^2}\right) \tag{2-18}$$

From these definitions we can understand V_{oc} as a measurable terminal characteristic that provides information about the amount of recombination in a device.

2.2.1.2 CONDUCTANCE

The recombination properties of a sample can also be indirectly accessed through measurements of the conductance, σ, given by [23]

$$\sigma = qW[n\mu_e + p\mu_h] \tag{2-19}$$

where W is the sample thickness, and μ_e and μ_h are the electron and hole mobilities, respectively. If the equilibrium conductance σ_{dark} is known, an excess conductance under excitation, $\Delta\sigma = \sigma_{light}$ - σ_{dark}, can be calculated as

$$\Delta\sigma = qW\Delta n[\mu_e + \mu_h] \tag{2-20}$$

assuming $\Delta n = \Delta p$. Thus, with sufficiently accurate models for the mobility (as are known for Si) measurements of the excess photoconductance can directly probe Δn in a sample and therefore measure recombination [23]. This is the basis for the well-known and widely used QSSPC technique [34].

2.2.1.3 LUMINESCENCE

When electrons directly recombine from the conduction to the valence band, a proportion of them transfer the excess energy to an emitted photon [16]. The spectral rate of spontaneous photon emission $dr_{sp}(\hbar\omega)$ per photon energy interval $d(\hbar\omega)$ and volume element is given by the generalised Planck equation [35] as

$$dr_{sp}(\hbar\omega, T) = \frac{(\hbar\omega)^2\kappa^2}{\pi^2\hbar^3 c_0^2}\alpha(\hbar\omega, T)\frac{1}{\exp\left(\frac{\hbar\omega - \Delta E_{QF}}{kT}\right) - 1}d(\hbar\omega) \tag{2-21}$$

where κ is the refractive index, c_0 is the vacuum speed of light, α is the absorption coefficient for band-to-band transitions and $\hbar\omega$ is the energy of the emitted photon. The

spectrum of radiative emission from crystalline silicon at room temperature is shown in Fig. 2-3.
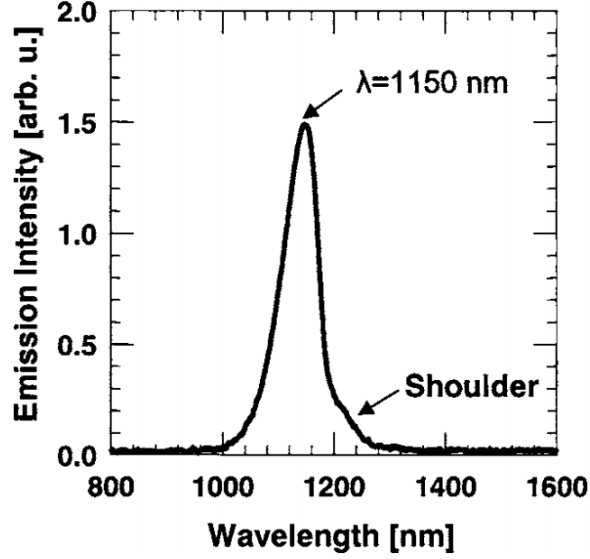
Fig. 2-3: Typical spectrum of emitted luminescence from Si at room temperature. Reproduced from [36].

Note that r_{sp} is a microscopic quantity that describes emission from an infinitesimal volume element. The actual measurable emission of photons from a surface, I_{PL}, is a complex function of the integrated r_{sp}, reabsorption probability, specific optical geometry of the sample surfaces and carrier injection level. By assuming that Δn is uniform in the sample, I_{PL} can be expressed as [37]

$$I_{PL} = A_i B_{rad}(\Delta n, T) n_i^2 \exp\left(\frac{\Delta E_{QF}}{kT}\right)$$ (2-22)

or alternatively via Eq. (2-7)

$$I_{PL} = A_i B_{rad}(\Delta n, T) np$$ (2-23)

where A_i is a sample dependent constant of proportionality which accounts for the sample optical properties and B_{rad} is the radiative recombination co-efficient which accounts for the high injection change in radiative emission [25], [38]. Note that in the case of significantly non-uniform Δn, photon reabsorption could cause A_i to be non-constant [39] but this is not a consideration for the experimental measurements in this thesis. Under excitation, Eq. (2-23) is expressed as [37]

$$I_{PL} = A_i B_{rad}(\Delta n, T) \Delta n [N_{dop} + \Delta n]$$ (2-24)

Thus, I_{PL} can be viewed as a function of either Δn or iV_{oc} and thus be used to study the sample recombination.

When the external excitation underlying the luminescence emission is caused by an external electrical current this is referred to as electroluminescence (EL) and when caused by illumination it is called photoluminescence (PL) [40].

2.2.2 MEASUREMENT TECHNIQUES

There are steady-state techniques and dynamic techniques for measuring recombination of excess charge carriers. Considering carriers being excited in a laterally uniform way, the general expression used to describe the dynamics of excess carriers is given by the continuity equation in one dimension [23]

$$\frac{\partial \Delta n}{\partial t} = G - U - \frac{1}{q}\frac{\partial J_n}{\partial x} \tag{2-25}$$

where x is the distance in direction perpendicular to the surfaces and J_n is the electron current in this direction. Nagel *et al.* [14] showed that in the case of uniform generation and uniform recombination given by $U = \Delta n / \tau$ the third term on the right side vanishes and Eq. (2-25) simplifies to

$$\tau = \frac{\Delta n}{G - \dfrac{d\Delta n}{dt}} \tag{2-26}$$

and further, that in the case of non-uniform generation and recombination an effective lifetime can still be obtained by first finding the average excess carrier density, Δn_{av},

$$\Delta n_{av} = \frac{1}{W}\int_0^W \Delta n(x)dx \tag{2-27}$$

and average generation rate,

$$G_{av} = \frac{1}{W}\int_0^W G(x)dx \tag{2-28}$$

giving

$$\tau_{eff} = \frac{\Delta n_{av}}{G_{av} - \dfrac{d\Delta n_{av}}{dt}} \tag{2-29}$$

This is a useful form to consider the equation because many real world samples conform to the case of non-uniform generation and recombination and the quantities Δn_{av} and G_{av} are accessible through experiment.

Kerr *et al.* [41] described the denominator of Eq. (2-29) as the net generation rate, G_{net}, with the first term describing the instantaneous generation rate and the second term describing the "carrier history" of a sample. They recognised that the same analysis can be applied to dynamic measurements of V_{oc}. G_{net} is obtained by solving Eq. (2-18) for $\Delta n(0)$ and differentiating. Importantly, the excess carrier history of interest from a V_{oc} measurement is $\frac{d\Delta n(0)}{dt}$, the excess carrier density at the contact [41].

Eq. (2-29) lends itself to discussion of several modes of measurement. *Steady-state* measurements occur when $\frac{d\Delta n_{av}}{dt} = 0$. *Transient* decay measurements can be obtained when $G_{av} = 0$. A *quasi-steady-state* (QSS) measurement is obtained when both denominator terms are non-zero. In this thesis, the term 'dynamic' is used to describe measurements in both the QSS and transient mode. In dynamic measurements, the excitation is modulated during the measurement such that Eq. (2-29) must be used to calculate τ_{eff}.

For certain sample types where Δn is significantly non-uniform or τ_{eff} is significantly injection dependent, the transient lifetime and QSS lifetime are different [42]. The QSS lifetime is the relevant lifetime for solar cells because of their steady-state operation. This is discussed further in Section 3.3.1.

The simplification of considering Δn_{av} and G_{av} instead of actual Δn and G can lead to measurement errors in many cases as is discussed in more detail in Chapters 4, 5 and 6. The above theoretical framework can be applied to several different specific measurement techniques.

2.2.2.1 QUASI-STEADY-STATE PHOTOCONDUCTANCE

A widely used characterisation technique in Si PV is quasi-steady-state PC (QSSPC) [7], owing to its simplicity and resulting ubiquity of the Sinton Instruments WCT-120 measurement systems [43] in research laboratories and PV companies around the world. In these systems, a radio frequency (RF) circuit is attached to a coil which is inductively coupled to a sample placed above it. The sample is illuminated with a xenon flash lamp with a controlled decay time. The changing $\Delta\sigma$ of the sample during excitation is detected by the RF coil, which can be directly converted to Δn_{av} using Eq. (2-20) and thus can be used to measure τ_{eff} via Eq. (2-29) or iV_{oc} via Eq. (2-9).

The technique is used for a wide range of PV applications on unmetallised samples such as lifetime spectroscopy [44], surface passivation [45], bulk lifetime degradation studies [46]. Though in certain cases, the usefulness of the technique can be limited by the effects of trapping [47] and depletion region modulation [48]. These effects are caused by the fact that the excess conductance is proportional to the *sum* of the carriers and usually result in erroneous data at low injection level.

Finally, and importantly for this thesis, PC measurements are not easily applied to samples with metal contacts already applied. The significantly higher conductance of metal dominates the overall conductance of the sample and makes detecting the PC signal difficult or impossible. Attempts to do PC measurements of metallised samples usually must deposit extremely thin metal layers or try to account for the extra conductance with a complex physical model [49].

These limitations can be addressed in large part by using photoluminescence instead of PC, discussed in Section 2.2.2.3.

2.2.2.2   SUNS-OPEN CIRCUIT VOLTAGE

By setting $J = 0$ in Eq. (2-15) the following is obtained

$$J_L = J_0 \left[\exp\left(\frac{V_{oc}}{mkT/q} \right) - 1 \right] - \frac{V}{R_{shunt}} \tag{2-30}$$

Thus, by varying the illumination intensity and measuring V_{oc}, a pseudo $J - V$ curve can be obtained that excludes the effects of series resistance and describes the recombination and shunt behaviour of a device [8]. The data can be used to extract J_0 and m. Alternatively, this method can be applied in true steady state mode, i.e. by measuring a device's J_{sc} and V_{oc} as the light intensity is changed step by step. This is called a $J_{sc} - V_{oc}$ measurement [33].

The Suns-V_{oc} approach [8] also results in data that follows Eq. (2-30). In these measurements the illumination level is varied in the QSS regime using a decaying flash lamp and an external reference detector is used to measure the illumination intensity instead of the cell's own J_{sc}. This limits series resistance and heating problems associated with high intensity steady-state J_{sc}-V_{oc} measurements [33].

Suns-V_{oc} measurements have wide applications in PV such as pseudo efficiency measurements [8], voltage loss analysis [50] and series resistance estimation, by

comparison with light *J-V* measurements [33]. It has also been used to diagnose problems with metal contacts such as formation of Schottky barriers [51].

Because of the relationship between V_{oc} and Δn at the cell contact (Eq. (2-18)), with knowledge of $N_{dop,}$ Suns-V_{oc} measurements can also be converted to implied τ_{eff} ($\tau_{eff,i}$) data under the assumption that Δn at the contact is equal to Δn_{av} [8]. In this thesis $\tau_{eff,i}$ is used to refer to τ_{eff} calculated from a Suns-V_{oc} measurement. This makes the technique potentially useful for measurements of surface recombination and contact recombination though several assumptions that are made in this conversion. The suitability of Suns-V_{oc} for these applications in explored in detail in this thesis (see Chapters 4 and 6).

2.2.2.3   QUASI-STEADY-STATE PHOTOLUMINESCENCE

As discussed in the previous section, PL is converted to Δn_{av} through Eq. (2-24). Therefore, it can also be used to perform dynamic measurements of τ_{eff} (typically called QSSPL [37] [52] in the literature) and iV_{oc}.(typically called Suns-PL [53] in the literature).

A typical QSSPL setup involves an illumination source to excite excess carriers and a photodiode to detect emitted PL photons [9]. The illumination source wavelength is usually selected such that it is shorter than the wavelengths of the emitted band-to-band PL.

While PC is proportional to the sum of the minority and majority carriers, PL is proportional to the product (Eq. (2-23)). This makes PL more robust against the limitations of trapping and DRM discussed in Section 2.2.2.1 and therefore enables more reliable measurement data at low to intermediate injection conditions.

Another advantage of using PL is that measurements of metallised samples are more easily obtained. This enables direct comparison of iV_{oc} and V_{oc}, and use of iV_{oc} to monitor voltage loss throughout cell processing [54]. Comparison of terminal voltage measurements and implied voltage measurements from dynamic PL are discussed in detail in Chapter 4.

The trade-off is that the calibration procedure for a PL setup is comparatively more complex. The sample-dependent linear constant of proportionality, A_i, must be obtained. This is achieved by either simultaneous measurement of the PL with an absolute metric for Δn such as PC or V_{oc} [9]; or a dynamic calibration method. Two important dynamic calibration methods are the so-called *self-consistent* method [15] and *self-sufficient* method [55]. These methods were rigorously examined and compared by Giesecke in Ref. [56], who concluded that lifetime data obtained from self-consistently calibrated

measurements can be directly interpreted as actual lifetimes whereas self-sufficiently calibrated data should be interpreted as differential lifetimes and must be converted.

2.2.2.4 SUNS-PHOTOLUMINESCENCE

Recognising the relationship between area averaged PL signal and iV_{oc}, the suns-PL technique was proposed by Trupke *et al.* [53] as a contactless alternative to Suns-V_{oc}. It is noted that Suns-PL data can equivalently be called Suns-iV_{oc} data or even implied J-V curves. An equivalent measurement can also be obtained from a QSSPC measurement by converting the injection dependent Δn_{av} to iV_{oc} using Eq. (2-9) [34]. Suns-PL is preferable in many cases though; because it is insensitive to metal conductance of a metallised cell, it can be applied at any stage of device processing from wafer to cell. In addition, the above mentioned artefacts that affect QSSPC at low to medium injection levels can limit the range of voltages that can be reliably measured.

All the above makes Suns-PL a useful technique for voltage loss analysis. It can also be made sensitive to larger or smaller area samples by using steady-state PL images at varied illumination intensities rather than a dynamic measurement, making it adaptable to full cells or more elaborate test structure designs [50].
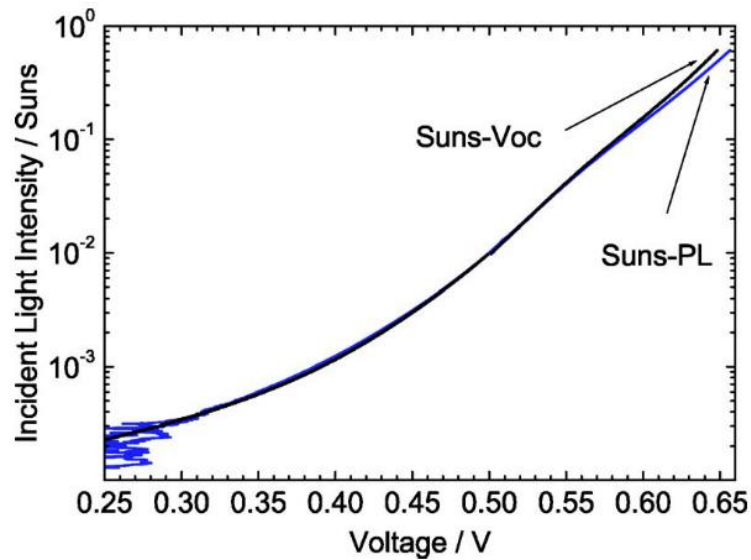
Fig. 2-4: Simultaneous Suns-V_{oc} and Suns-PL measurement of bifacial buried contact solar cell. Reproduced from Ref. [53].

Trupke *et al.* reported excellent agreement between Suns-PL and Suns-V_{oc} measurements of the same device up to illumination levels of approximately 0.1 suns and some divergence of the V_{oc} and PL data for higher illumination intensities (see Fig. 2-4). This deviation was not analysed in detail by Trupke *et al.* but has been reported

briefly by others [82]. It is investigated for the first time in detail using simulation and experiment in Chapter 4.

2.2.2.5 LUMINESCENCE IMAGING

Luminescence imaging involves steady-state excitation of a sample either electrically through contacts (EL imaging) [36] or optically (PL imaging) [10] and capture of the emitted luminescence with a camera. This results in a high resolution spatially resolved image of the radiative recombination in a sample. Calibrated images can give spatially resolved data of the local iV_{oc}, τ_{eff}, R_s [40]. Even uncalibrated images at open-circuit can be used to show relative differences in sample iV_{oc}, which is useful for studying spatially resolved cell defects [58].

2.3 CHARACTERISING METAL SURFACE RECOMBINATION

Measuring surface recombination at metal contacts is challenging because of the variety of metallisation approaches that exist. The contact can cover the full cell area or be deposited in lines or points with widely varying sizes and spacing, depending on the cell design. Also, a wide variety of deposition methods are studied. The challenge is to establish a simple to apply technique that is also versatile. In this section, several existing techniques to characterise the metal contact saturation current density, J_{0m}, are discussed and assessed.

2.3.1 KANE-SWANSON TECHNIQUE

A widely used approach to measuring surface recombination is based on a method originally proposed by Kane and Swanson [59] to extract J_{0e} from PC decay measurements. The method was improved by several authors over the years to account for Auger recombination [60], bandgap narrowing [61], and inhomogeneous minority carrier density profile [62]. A detailed examination of the assumptions in the method and various improvements was made by Mäckel *et. al.* [63]. The present methodology allows extraction of J_{0s} from injection dependent lifetime data using the expression

$$J_{0s,tot} = qW \frac{d}{d\Delta n_{av}} \left(\frac{n_{i,eff}^2}{\tau_{corr}} \right) \tag{2-31}$$

where q is the elementary charge, τ_{corr} is the effective lifetime corrected for Auger recombination and $J_{0s,tot}$ is the sum of the of the front and rear surface J_{0s}, respectively. It is noted that in this thesis, application of Eq. (2-31) to injection dependent lifetime data is referred to as the modified Kane-Swanson method. This is also the method implemented in the Sinton Instruments WCT-120 lifetime tester as described by Blum *et*

al. [61]. Further improvements to this approach were proposed by Kimmerle *et al.* [62] to account for finite Shockley-Read-Hall bulk lifetime (τ_{SRH}) and deviations from a uniform carrier profile resulting from a finite diffusion length. Importantly, the proposed iterative procedure to account for τ_{SRH} still assumes the bulk lifetime to be independent of injection level, but the additional correction improves the accuracy of the method's ability to account for the injection dependence of bandgap narrowing. It is also notable that the approach to account for finite diffusion length uses an analytical expression for the surface recombination velocity that assumes identical front and rear surface passivation and a uniform generation rate [64]. This thesis is chiefly concerned with measurements of samples that do not meet these assumptions, such as samples with highly recombinative metallised surfaces. Thus, given the apparent simplicity of the methods both Blum's and Kimmerle's approaches are analysed in Chapter 5 to establish the conditions under which they can and cannot be applied accurately.

The general approach of these slope-based methods is to perform a linear fit to a plot of inverse corrected lifetime as a function of Δn_{av} at an injection level where τ_{eff} is dominated by surface recombination. Kane and Swanson suggested to use an injection level equivalent to ten times the doping density, though others have suggested five times the doping density can be more appropriate [65]. Below this injection level, τ_{eff} is heavily convolved with the impact of the bulk lifetime. However, when bulk doping densities of typical industrial Czochralski (Cz) wafers are used, this range is impacted by a reduced diffusion length caused by Auger recombination preventing carrier recombination at the surface [62].

The method in its original conception is designed to extract J_{0s} of passivated or diffused surfaces, usually using PC measurements. Some attempts have been made to expand the technique to measure J_{0m} of metallised surfaces using other measurement techniques. In References [66] and [67], Müller *et al.* reported J_{0m} data obtained from metallised test samples using the modified Kane-Swanson method. They obtained injection dependent lifetime data from calibrated PL images taken at different intensities. J_{0m} of samples with single side full metallisation are reported in Ref. [66]. In Ref. [67], busbar and finger metallisation pattern is measured. Using device modelling, they identified contact width and sheet resistance as impacting the accuracy of their approach.

The modified Kane-Swanson method is used to determine $J_{0s,tot}$, which is a parameter that combines the surface recombination from different regions into a single parameter. Therefore, it can also potentially be applied in the context of a metal area fraction (f_{met}) based approach as discussed in Section 2.3.3 below. This approach is evaluated for the

first time through simulations and experiment in Chapter 6. Given the strict assumptions employed in the modified Kane-Swanson method, the approaches employed in References [61] and [62] are critically evaluated in the context of metallised samples using simulation and measurement in Chapters 5 and 6.

2.3.2 ANALYTICAL TECHNIQUES

Fischer reported an analytical model [68], which relates an effective area-averaged rear surface recombination velocity, S_{eff}, to the metallised and non-metallised area surface recombination velocities and f_{met}. The model was applied to lifetime measurements of point contacted structures [69] and screen-printed line contacts [70] by Müller *et al.* where the lifetime measurements were obtained by dynamic infrared lifetime mapping (DILM) [71]. However, as discussed in Ref. [12], the model has limited practical use because of the assumption of low level injection and uniform Δn. It also assumes constant or infinite bulk lifetime, injection independent surface recombination velocity values. These assumptions are unlikely to be met in many practical cases. The assumption of uniform Δn, which also applies to many other techniques, is evaluated thoroughly in Chapters 4, 5 and 6.

2.3.3 METAL AREA FRACTION BASED TECHNIQUES

Another class of techniques involve making measurements of multiple identically processed samples where f_{met} is varied and thus nominally the only difference between the samples.

This approach was first reported by Fellmeth *et al.* [72] to measure J_{0m} of screen-printed front line contacts on phosphorus diffusions. Fellmeth *et al.* created samples with a full area rear contact and multiple mini-cell front contacted regions where the front f_{met} was varied by changing the pitch of the line contacts within a square border contact (see Fig. 2-5). Each mini-cell was measured with Suns-V_{oc} and had J_0 extracted from a fit of Eq. (2-30) at one sun illumination intensity.

The following relation asserts that J_0 is simply equal to the sum of all area normalised recombination current densities in the device,

$$J_0 = J_{0,bulk} + J_{0,rear} + f_{met}J_{0m} + [1 - f_{met}]J_{0s} \qquad (2\text{-}32)$$

where $J_{0,bulk}$ is the bulk recombination saturation current density, $J_{0,rear}$ is the rear surface recombination saturation current density and J_{0s} is the passivated front surface recombination saturation current density. In particular, it asserts that J_{0s} and J_{0m} simply

add in proportion to f_{met} to make up a total effective front surface J_0. Then, given that J_{0s} is known from a separate measurement of the passivated surface, and $J_{0,bulk}$ and $J_{0,rear}$ are constant across the sample, J_{0m} is obtained from the slope of a linear fit of J_0 against f_{met}. Fellmeth *et al.* identified that Eq. (2-32) only applied given the assumption that all of the recombination processes occurred with unity ideality factor.
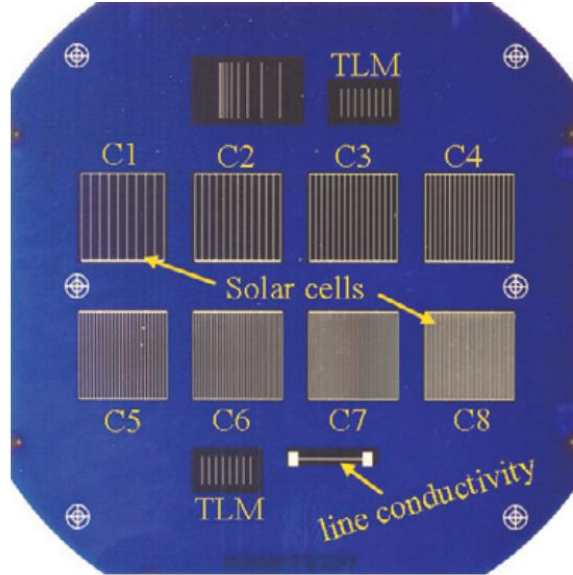
Fig. 2-5: Sample design for *f_{met}* varied sample (reproduced from Ref. [72])

This method was investigated further by Inns and Poplavskyy [73] who performed simulations using Quokka [74] to investigate optimal sample design. Based on the simulations they conclude that varying f_{met} by modulating the metal finger width rather than the finger pitch is preferable because of the effect of the lateral sheet resistance. They also state that better signal-to-noise ratio is obtained for samples with larger f_{met} or larger J_{0m} so if possible larger f_{met} than a typical cell metallisation pattern is preferable. Finally, they also identify that, because of the full area diffusion on the samples, the mini-cells are not electrically isolated from each other and thus current generated between the mini-cells can "leak" into the mini-cell regions and cause erroneous measurements. They place an extra metallised square around each mini-cell in an attempt to isolate it.

The method was further developed by Comparotto *et al.* [11] who follow the same J_{0m} extraction procedure as Fellmeth *et al.*, but instead of using mini-cells, they use a symmetrically diffused and passivated test sample with metal deposited in several regions of interest with f_{met} varied. Instead of using Suns-V_{oc} measurements, they use voltage calibrated open circuit PL images taken at different intensities (effectively steady-state Suns-PL measurements). In their experiments, f_{met} is varied by changing the pitch of constant width line contacts.

Shanmugam *et al.* also reported an expanded f_{met} based model in the context of their full device model approach [13], discussed in Section 2.3.4 below. Instead of fitting a simple ideal diode J_0 they used non-linear curve fitting to fit a two-diode model to Suns- PL images. However, they concluded that this model was inaccurate compared to their full device model.

The differences between the cell based Suns-V_{oc} method and test structure based Suns-PL method is not immediately apparent though we know from above that V_{oc} and iV_{oc} are defined differently. This is explored is greater detail in Chapter 6.

2.3.4 FULL DEVICE MODEL TECHNIQUES

Whereas other J_{0m} extraction techniques use simplifying assumptions to enable J_{0m} to be extracted, another class of techniques attempt to minimise assumptions by using finite element device modelling to construct an accurate model of a particular sample and measurement and solve for the unknown J_{0m}.

Fell *et al.* [12] apply this approach using Quokka version 2 [74] for samples with laser doped point contacts. The samples are double side passivated float zone (FZ) silicon wafers with multiple regions of different f_{met}, where f_{met} is varied by varying the contact pitch. The samples are measured with PL images at multiple light intensities. A region of the sample is left without metal contacts so a QSSPC measurement can be used to determine J_{0s} of the passivated surfaces and calibrate the PL counts of the images to the simulated PL from Quokka. The τ_{bulk} is assumed to be limited by Auger recombination. Thus, all the relevant recombination parameters are known except J_{0m}. The calibrated PL image is fitted with J_{0m} as the fit parameter. To test the assumption of the metal recombination occurring with unity ideality factor, the local recombination current and Δn at the contact are extracted from the finite element model for each PL image and plotted against each other.

The method minimises assumptions compared to other techniques and results in a J_{0m} parameter that is independent of the substrate conditions, however, the method is also more complex than other methods owing to the careful measurement required to completely characterise the optical capture of emitted PL. It is also unclear if the method can be applied to samples with full area diffusions because of the potential for lateral currents to flow between the various metallised regions of interest. These currents are not presently accounted for in the Quokka version 2 model, though an upgrade to Quokka version 3 might make this possible.

A different device modelling approach, which uses the Griddler [75] cell simulation package, is reported by Shanmugam *et al.* [13]. As in the Quokka based approach, samples with multiple regions of varied metal area fraction are PL imaged at different illumination intensities. However, using the known geometry of the metallisation pattern Griddler is able to fit to the whole PL image at once, which includes parasitic lateral currents from the non-metallised into the metallised and edge regions of the sample. This allows using full area diffused regions in the sample. Because the Quokka based approach only simulates a unit cell, it cannot easily be used for samples where lateral current flow is high. Furthermore, Griddler assumes a model of interconnected two-diode model nodes and doesn't simulate the local carrier physics with a high level of rigour. Thus, the method has limited ability to simulate the metal recombination in the device if it occurs non-ideally. It also does not simulate the depth dependence of the excess carrier profile or resulting band-to-band emission. It makes the assumption that the exponential of the voltage given by the two-diode model at each node is proportional to the detected PL signal. Thus, subtle effects related to short wavelength illumination and high local recombination causing non-uniform excess carrier distributions may not be accurately accounted for in this method. This issue is explored in detail in Chapter 5.

Another important difference between the two methods is that they report different parameters. The Quokka based method of Fell *et al.* [12] reports J_{0m} independent of sample geometry with an ideality factor *m* assuming a model of

$$J_{rec,cont} = J_{0m} \left[\left[\frac{\Delta n_{cont} [\Delta n_{cont} + N_{dop}]}{n_i^2} \right]^{\frac{1}{m}} - 1 \right] \tag{2-33}$$

where $J_{rec,cont}$ is the recombination current density into the contact, Δn_{cont} is the excess carrier density at the contact. On the other hand, the Griddler based method of Shanmugam *et al.* [13] reports $J_{01,metal}$ and $J_{02,metal}$, which are actually the saturation current densities of the metallised nodes in the model, which includes recombination from the metallised surface as well as the bulk and non-metallised surface. Thus, the values obtained from each method are not directly comparable.

2.3.5 EVALUATION

A variety of methods to extract J_{0m} have been presented, each with varying assumptions and levels of complexity and it is not clear from the existing literature which, if any, is most accurate or reliable. In different contexts it may be desirable to sacrifice accuracy for simplicity or speed.

The modified Kane-Swanson approach and analytical approaches contain the most assumptions, and both approaches also appear to be trying to apply a technique that was proposed for a particular purpose into another context for which it wasn't originally intended. The Kane-Swanson approach was proposed to measure J_{0e} on very high lifetime, unmetallised wafers that were symmetrically processed. It is unlikely that the same approach can be applied to metallised, asymmetrically processed samples with arbitrary bulk lifetime. Its relative simplicity makes it an attractive option but its accuracy for the particular problem of measuring metallised surface recombination needs to be assessed. The analytical model of Fischer was originally designed to estimate area averaged properties given certain local recombination properties under a series of assumptions, but it is unclear that the reverse operation is possible. The modified Kane-Swanson extraction approach is investigated using simulations and experiment in Chapters 5 and 6 of this thesis.

The techniques based on varying f_{met} and the full device model techniques take very different approaches to measuring the same parameter. The f_{met} approach uses many simplifying assumptions that make it easier to apply but it is unclear if these assumptions reduce accuracy. The full device model techniques make the least assumptions and therefore might be assumed to be most accurate, but are the complications of applying the full device models always necessary? These approaches have also been applied to different types of samples by different authors. Some have full area diffusions, some do not have full area diffusions, some vary the contact width while the contact pitch is constant to change f_{met}, others vary the contact pitch to and keep the contact size constant to change f_{met}, some measurements are performed on full cells while others are on passivated test structures. It is unclear if any of these differences between samples make a difference to the applicability or accuracy of the different methods. A simple method that is as widely applicable as possible is thus desirable and needed. These questions are investigated using simulations and experiment in this thesis.

CHAPTER 3: METHODOLOGY

It was established in Chapter 2 that QSSPL is a potentially useful technique to study metal contact recombination. It was also established that τ_{eff} and iV_{oc} measurements are essentially two different ways to interpret the same raw measurement. This Chapter details the development of the QSSPL measurement systems that are used for the experimental work in this thesis.

3.1 INTRODUCTION

QSSPL for the characterisation of silicon wafers to be used in solar cells was first demonstrated by Trupke *et al.* [37]. The same measurement setup was used to demonstrate Suns-PL with the addition of voltage probes [53]. The system used by Trupke *et al.* consisted of a modified Sinton Instruments QSSPC system [43] where the PC coil was mounted on a transparent window and a Si photodiode was mounted underneath the coil to detect emitted PL. The PC measurement allowed calibration of the PL signal and mounting the detector under the sample simplifies the filtering arrangement because shorter wavelength illumination light is completely absorbed in the sample. However, it does make measuring metallised samples more difficult. Only partially metallised or bifacial samples can be measured using this setup. Trupke *et al.* also developed a *self-consistent* calibration procedure [15], which potentially negates the need for separate calibration to a PC or V_{oc} measurement. This procedure was used in this thesis and is discussed in Section 3.3.1.

QSSPL was developed further by Giesecke, whose work is best summarised in Ref. [56]. The theoretical understanding of the measurement was significantly developed, but also the measurement setup was improved. Giesecke *et al.* demonstrated the technique in reflectance mode, where the PL detector was placed on the front side of the sample, the same side as the light source [76]. They also reported another calibration procedure, which negated the need for knowledge of the bulk doping density of the sample, called *self-sufficient* calibration [55]. Both self-consistent and self-sufficient calibration rely on accurately measuring the time dependence of the PL and incident illumination signals. Giesecke showed that the faster response time of indium gallium arsenide (InGaAs) detectors compared to Si detectors results in higher accuracy for low lifetime samples when dynamic calibration is used [77]. InGaAs detectors also have other advantages for use with metallised samples due to their sensitivity to longer wavelength light, which is discussed further in Section 3.2.1.3.

These developments make QSSPL a useful technique to study metal surface recombination. The QSSPL measurement systems used in this thesis are described in Section 3.2. The calibration procedures that were applied are described in Section 3.3 and experimental data that validates that the system and calibration were working correctly are presented in Section 3.4.

3.2 EXPERIMENTAL SETUPS

The experimental setup used in this thesis evolved considerably over the course of this thesis. The two key experimental setups are described below along with the reasoning behind the changes that were made.

3.2.1 NARROW ILLUMINATION SETUP

3.2.1.1 DESCRIPTION

The initially developed measurement setup is shown schematically in Fig. 3-1. The cell is illuminated from above with a xenon flash lamp, filtered such that light in the silicon band-to-band emission spectrum is blocked. Emitted PL is reflected off a filter mounted at 45° towards an appropriately filtered InGaAs photodiode, which is mounted at a fixed relative position to the angled filter. The relative illumination intensity is detected by a silicon reference cell that is separately mounted off-centre from the PL setup. The detectors that monitor the illumination intensity and the PL intensity are connected to separate low noise current pre-amplifiers. The system is computer controlled with a National Instruments data acquisition card, which triggers the illumination pulse and records the detect signals.

In the experiments discussed in Chapter 4, the samples are placed on a contacting stage that allows the terminal voltage to be measured. In this case, the angled filter and PL detector setup was placed on top of the voltage contacting stage.

3.2.1.2 ILLUMINATION COMPONENTS

The flash lamp is a Q-Flash xenon flash lamp, the standard lamp supplied with the Sinton Instruments WCT-120 [43]. It is mounted such that the maximum intensity is equivalent to approximately 50 suns at the sample surface.

Unlike the standard long pass filter used in a WCT-120 system, for this setup, a 150 mm × 150 mm and 4 mm thick Schott KG3 absorptive short pass filter is placed in front of the flash lamp. Fig. 3-2 shows a standard representation of the emission spectrum from a Q-Flash lamp [78], [79] overlaid with the transmission of the KG3 filter.
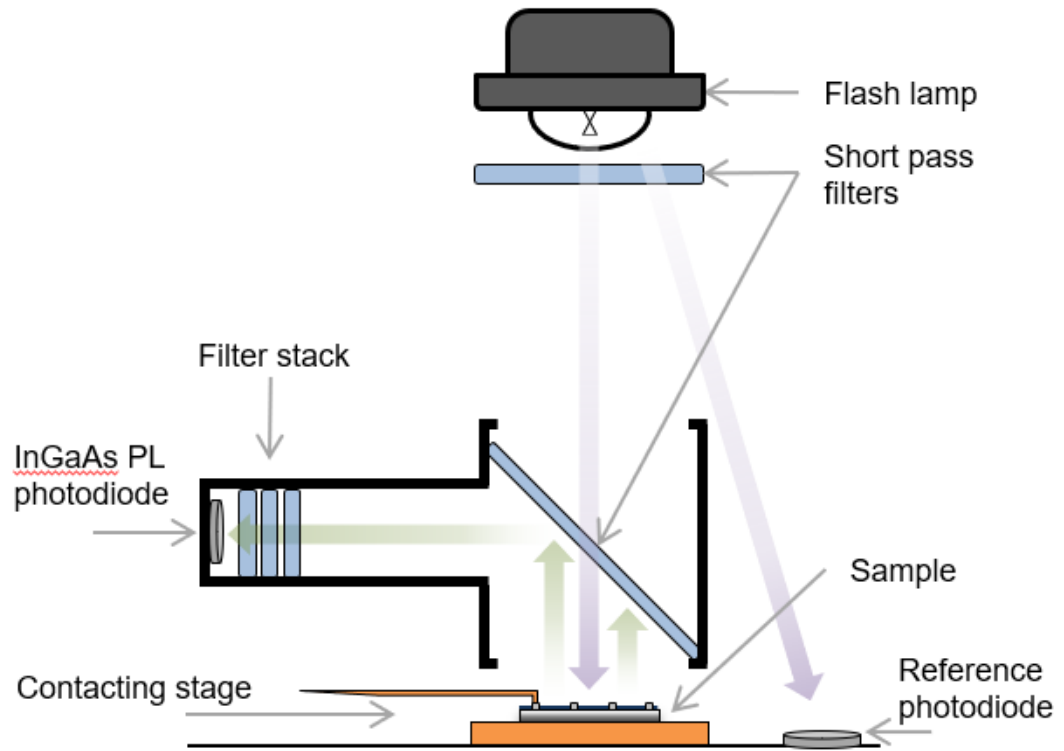
Fig. 3-1: Schematic layout of the system used to obtain simultaneous measurements of Suns-V_{oc} and Suns-PL. Purple arrows indicate incident light and green arrows indicate the collected PL.
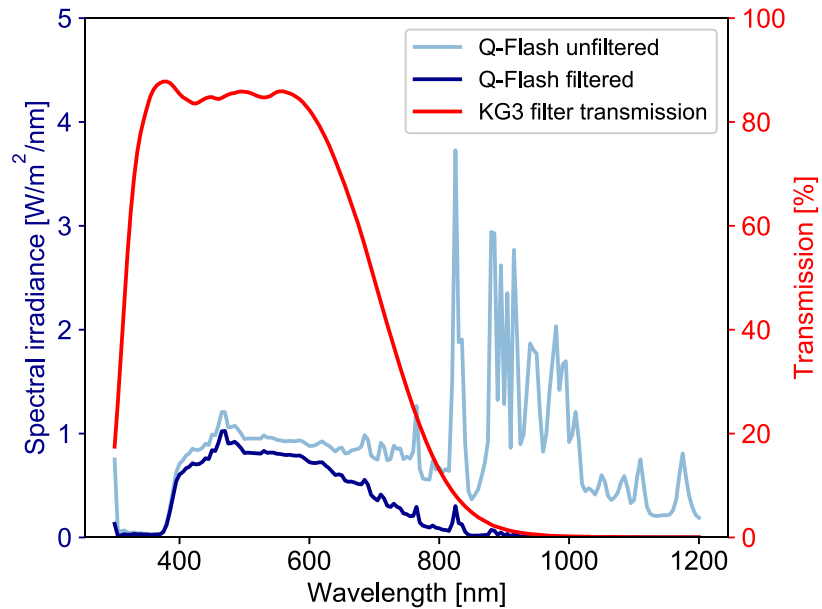
Fig. 3-2: Spectral emission of the Q-Flash overlaid with the spectral transmission of the KG3 filter. Unfiltered data from Ref. [78].

3.2.1.3   DETECTION COMPONENTS

The PL detector is a Thorlabs SM05PD5A InGaAs photodiode with circular active area diameter 2 mm [80]. Although it is possible to use Si detectors for PL measurements of Si samples, an InGaAs detector was chosen for this thesis for a couple of critical reasons. Most importantly, as described in Ref. [77], using an InGaAs detector is critical to ensure the accuracy of the dynamic calibration for low τ_{eff} samples. Si detectors are unable to respond fast enough to dynamic excitation to ensure that the sample lifetime is the only thing affecting the measured PL signal. See Section 3.3.1 for further discussion of dynamic calibration.

An additional benefit is that InGaAs has a lower bandgap than Si so it is sensitive to the entire band-to-band emission spectrum whereas Si is only sensitive to wavelengths shorter than approximately 1050 nm (see Fig. 3-3). This is particularly useful for measurements of metallised samples where reflections from metal on a sample can cause optical artefacts, unrelated to the recombination properties of the sample. By using an InGaAs detector, though, the PL signal is dominated by longer wavelength luminescence which bounces multiple times in the sample and smears out the effect of the rear optics.
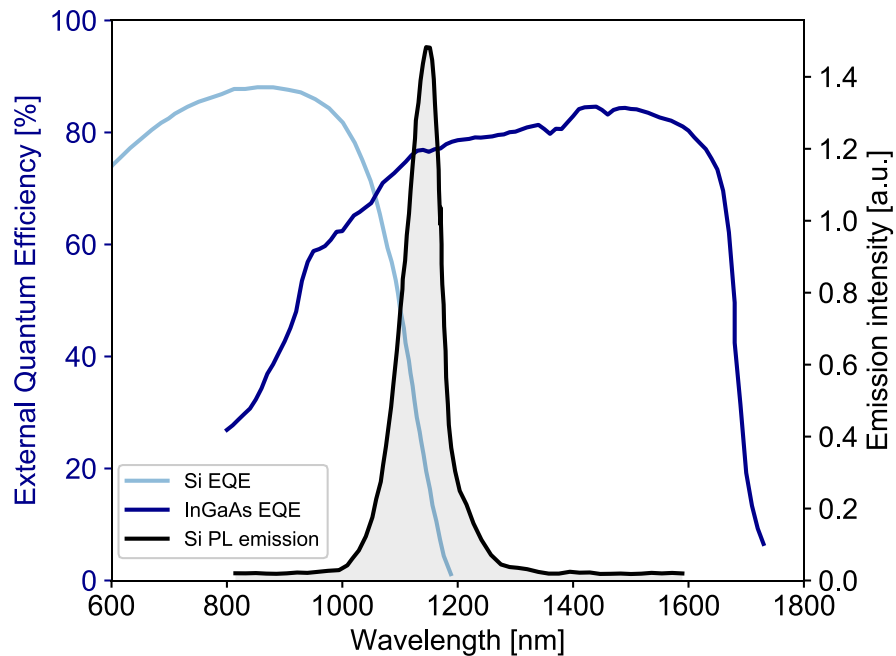
Fig. 3-3: EQE of Si detector, InGaAs detector (left axis) and emission intensity of typical PL spectrum [36] (right axis). InGaAs has high quantum efficiency across the entire PL spectrum while Si is only sensitive to shorter wavelength PL emission less than 1050 nm.

A stack of three 1-inch diameter circular glass filters is placed directly in front of the PL detector: an absorptive 850 nm long pass filter, a reflective 950 nm long pass filter and

a 1250 nm short pass filter. This stack of filters blocks light in the wavelength range of the incident light and infrared light with wavelength longer than the characteristic band-to-band emission of Si. The detector and filter stack were separated from the incident light path by a 5 cm length of tube to minimise the amount of incident light that could enter the detector. PL is reflected towards the PL detector by a 5 × 5 cm reflective glass 850 nm short pass filter.

The reference illumination intensity detector is the standard reference cell of a Sinton Instruments WCT-120 system. Because the flash lamp is positioned closer than typical operation and the usual filter is not used, an aperture is placed on top of the cell to ensure it is operating in its linear range.

The PL detector is connected to a Femto DLPCA-200 transimpedance pre-amplifier [81]. Frequency response of the pre-amplifier is critically important for dynamically calibrated PL measurements for the same reasons as described above for the PL detector. Any lag in the response time of the pre-amplifier to a dynamic signal will cause an error in the calibration and result in incorrect data.

In general, it is desirable to increase amplifier gain to improve signal to noise ratio in a measurement. However, by design, the cut-off frequency reduces (and thus the phase lag increases) with increased gain. Therefore, care has been taken during measurements to ensure the measured lifetime is the same at different gains. This is particularly important for low lifetime samples, which have weaker PL signal.

3.2.1.4 LIMITATIONS

The box-shaped mount for the detector setup limited the area of illumination to small samples with area less than approximately 5 × 5 cm. This presented a problem for measuring large 156 cm^2 samples. Even large wafers with multiple smaller regions of interest such as those described in Section 6.3 could not be accurately measured because the mounting box would shade the rest of the sample.

Using the xenon flash lamp largely rules out using a dynamic calibration approach, due to the limited control over the light pulse profile. These measurements were thus limited to using an external calibration, such as a voltage probe as is used in the experiments in Chapter 4. Metallised test structures that are typically used to measure metal surface recombination are obviously metallised, which limits the usefulness of external calibration using PC; but in many cases are not completed cells either, making contacted V_{oc} measurements impossible. Thus, a dynamic calibration of the PL measurement is

required for these samples. Such calibration techniques rely on a light source that can have its intensity precisely modulated with a controller like an LED or laser.

These limitations were addressed in the second measurement setup described in the next section.

3.2.2 FULL AREA ILLUMINATION SETUP

The following system was developed to address the limitations of the previously described system and enable convenient measurement of metallised samples. A schematic diagram of the setup is shown in Fig. 3-4. The sample is uniformly illuminated from above with either an 808 nm diode laser capable of a maximum intensity equivalent to approximately one sun in the sample plane; or a Q-Flash xenon flash lamp with maximum intensity equivalent to approximately 30 suns which is filtered in the same way as the system described in Section 3.2.1 (see Fig. 3-2) to block light in the Si band-to-band emission spectrum. As in the previously described setup, an InGaAs photodiode is used to detect PL (PL sensor). In this system it is mounted above the sample at the end of a tube behind a lens that focuses luminescence from a small spot on the sample surface onto the PL sensor. The same filter stack as the first system are placed in front of the lens to ensure that only Si band-to-band emission is detected. A calibrated photodiode mounted beside the sample measures the incident photon flux during measurements. The photodiodes are connected to Femto DLPCA-200 transimpedance pre-amplifiers [81] and the final signals are captured using a National Instrument data acquisition card.

The time dependent measurements of relative illumination and PL intensity are converted into injection dependent τ_{eff} data using the established QSSPL theory with self-consistent calibration [15], [76] as described in Section 3.3.1. The PL signal is calibrated by modulating the laser intensity sinusoidally at an intensity below one sun. The flash lamp is used for high intensity illumination to enable higher injection level lifetime data to be obtained.

Notably, self-consistent calibration using an InGaAs detector elegantly addresses the issue of variable rear optics when analyzing samples with partial rear metallization. [76] The PL signal is dominated by longer wavelength luminescence which bounces multiple times in the sample and smears out the effect of the rear optics. This is not the case with the Si detector used in other PL based techniques [12], [13].
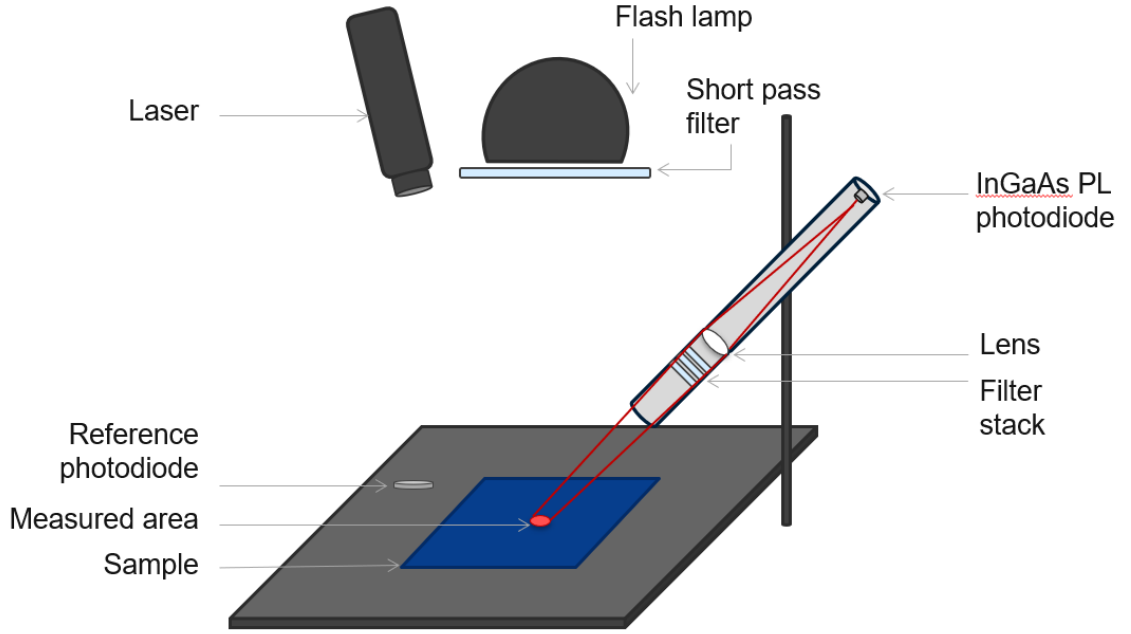
Fig. 3-4: Schematic diagram of QSSPL measurement system for metal surface recombination measurements.

3.3 CALIBRATION PROCEDURES

As discussed in Section 2.2.2.3, a raw QSSPL measurement consists of two relative measurement signals, i.e. the PL and the incident light intensities, respectively. The following calibration procedures are used in this thesis to convert these relative signals to useful measurands Δn_{av}, iV_{oc} (from PL) and G_{av} (from incident light intensity).

3.3.1 CONVERTING PL TO AVERAGE EXCESS CARRIER DENSITY

The PL signal was calibrated using the self-consistent method of Trupke *et al.* [15]. The calibration problem is the same as determining A_i in Eq. (2-24). N_{dop} was determined for each sample either from a separate PC measurement of the raw wafer before processing, or for the cells measured in Section 4.4, using the method of Hameiri *et al.* [82]. B_{rad} was known from a published model [25], [38]. Thus, Eq. (2-24) has two unknowns. A QSSPL measurement is made with a sinusoidally modulated laser pulse. Rearranging Eq. (2-24) in terms of Δn_{av} and substituting into Eq. (2-29), when A_i is correctly chosen, the calculated τ_{eff} is identical for the rising and falling part of the modulated pulse. Because of the $\frac{dn_{av}}{dt}$ term in the denominator of the right hand side of Eq. (2-29), when A_i is incorrect, the error in the calculated τ_{eff} is positive for one part of the pulse and negative for the other part of the pulse. This causes a visible hysteresis in the plot of τ_{eff} against

Δn_{av}. Thus, the correct A_i is found when the hysteresis is minimised. This effect is shown in Fig. 3-5.
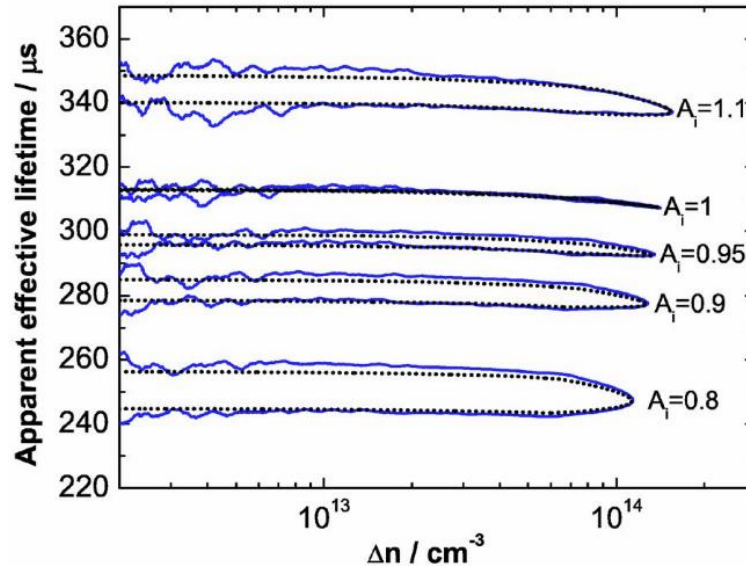
Fig. 3-5: Apparent τ_{eff} for various values of A_i as a function of Δn_{av} (reproduced from Ref. [15]).

The accuracy of the time response of the detection system is thus critical to the accuracy of the calibration. This was a critical factor for component selection. As discussed in Section 3.2.1.3, a fast InGaAs detector and transimpedance preamplifier were specifically chosen because of their frequency response. For each sample, calibration measurements were repeated at different gain levels on the preamplifiers to ensure that the same A_i was obtained. That is, that the preamplifier response time was not the limiting factor on the response time of the detector system.

The laser used in this thesis is only capable of an intensity up to approximately one sun so a high intensity flash lamp was used to obtain measurements up to 30 suns illumination intensity. The A_i determined from the laser calibration measurements was then also used to calibrate flash measurements. The error from this simplification is deemed small because the flash illumination is short-pass filtered (see Fig. 3-2) such that it has similar absorption depth to the laser illumination. Thus, both light sources would affect the depth profile of Δn in a similar way.

Dynamic calibration techniques (including self-consistent calibration) can result in erroneous calibration of lifetime data in the presence of high surface recombination velocity [83], [84]. Many samples in the experiments in Chapters 5 and 6 exhibit such high surface recombination velocity, however, it is noted that the calibration is performed using an excitation modulation rate that is of the same order as the sample τ_{eff} and at low

to intermediate injection level ($\Delta n_{av}/N_{dop} \leq 1$), where the surface recombination is low such that these effects are avoided, and the steady-state lifetime is obtained. Concerns related to the effects of non-uniform Δn on photon reabsorption are avoided by using the InGaAs PL sensor [39].

3.3.2 CONVERTING INCIDENT ILLUMINATION INTENSITY TO AVERAGE GENERATION RATE

The general expression for the average generation rate in a sample is given by

$$G_{av} = \frac{\varphi_{ph} a_{sample}}{W} \tag{3-1}$$

where φ_{ph} is the photon flux at the sample surface, a_{sample} is the optical absorptance of the sample. The sample thickness, W, is easily measured. But it is non-trivial to measure φ_{ph} and a_{sample} and the procedure for measuring each depends on whether a single wavelength light source (e.g. LED or laser) or a broadband light source (e.g. white flash lamp) is used.

3.3.2.1 SINGLE WAVELENGTH ILLUMINATION

The single wavelength illumination sources used in this study had wavelength 810 nm or lower, so the absorptance is easily obtained as

$$a_{sample} = 1 - r_\lambda \tag{3-2}$$

where r_λ is the sample reflectance at the illumination wavelength. r_λ is measured for each sample with a spectrophotometer.

To obtain φ_{ph}, the signal from the reference photodiode (ref. PD) that measures the incident light intensity is calibrated. Since φ_{ph} is independent of the sample, a separate calibration measurement is made to determine a calibration factor which is then applied to each measurement.

For the calibration measurement, a photodiode of known EQE at the illumination wavelength (cal. PD) was placed in the sample position and a measurement is performed with the illumination source illuminating the same pulse shape as a real measurement. Both PDs are connected to pre-amplifiers in current amplification mode. In this mode when PDs are operating in their linear ranges, the measured pre-amplifier output voltage (V_{out}) is linear with the PD short circuit current (I_{sc}) through the amplifier gain (g_{amp}) as $V_{out} = I_{sc}g_{amp}$. The cal. PD I_{sc} is also directly related to the incident photon flux as

$$I_{sc} = A_{cal}\varphi_{ph}qEQE_\lambda \tag{3-3}$$

where A_{cal} is the surface area of the cal. PD. Assuming both PDs are operating in their linear ranges, the ratio of the signals during the measurement pulse is a constant and a calibration factor (F_s) can be determined as

$$\varphi_{ph} = F_s \frac{V_{ref}}{g_{ref}} \tag{3-4}$$

where V_{ref} and g_{ref} are the measured voltage signal preamplifier gain of the ref. PD.

F_s is a lumped constant that equates the measured reference voltage with the photon flux at the sample surface. It accounts for both the geometry of the relative arrangement of the sample and ref. PD, and any obstacles in the optical path of the incident light (e.g. filters, lenses etc.). For a given light source, if any changes are made to the geometry or incident light optics, F_s must be recalibrated.

3.3.2.2   BROAD SPECTRUM ILLUMINATION

Broad wavelength spectrum illumination adds an additional complication to the calibration because the spectrum of the light is not well defined. For example, as a flash lamp gets hotter or ages its spectrum changes. Hence, the spectral dependence of the optical components in the system is not constant. Also, each sample has a spectral absorption that varies and is not as easily measured as at a single wavelength. Therefore, the following procedure is followed to account for these issues and calculate F_s.

In the experiments in this thesis, the purpose of using a broadband illumination source such as a flash lamp is to enable the highest illumination intensities to be achieved. In these experiments, a single wavelength measurement is first performed at one sun illumination intensity and then the flash lamp measurement is made such that the lower intensity part of the flash decay overlapped with the high intensity part of the single wavelength measurement. The F_s for the broadband illumination is then adjusted until the injection dependent lifetime or Suns-PL data from each light source match in the overlapping region.

Rather than an inherent property of the light source only related to the photon flux as in the single wavelength case, here F_s becomes a *sample-dependent* scaling factor for the measured reference voltage to the generation rate directly and incorporates both the incident photon flux and absorption of the sample. The implicit assumption of this method is that τ_{eff} or iV_{oc} and Δn_{av} do not differ in their dependence on the wavelength of the

illumination source. The flash lamp used in these experiments is filtered to block the IR radiation (see Fig. 3-2). Thus, all the illumination sources have wavelength such that most of the light is absorbed in the first few microns of a sample and would have similar effect on the depth profile of Δn.

3.3.3 CONVERTING QSSPL TO SUNS-PL

From the combination of Equations (2-22) and (2-8) it can be seen that the PL signal is proportional to the exponential of iV_{oc} and thus in the case where a simultaneous voltage measurement is possible, such as the experiment in Section 4.4, a direct conversion is possible. However, because the measurement is taken under QSS conditions, care was taken to ensure the equivalent steady-state illumination intensity, φ_{net} was used rather than φ_{ph}. This is calculated as

$$\varphi_{net} = \frac{qW[G_{av} - \frac{dn_{av}}{dt}]}{J_{sc,1sun}} \tag{3-5}$$

where $J_{sc,1sun}$ is an estimated one sun short circuit current density [41]. Importantly, such a conversion still relies on applying a calibration of the PL signal to Δn_{av} rather than directly relating PL intensity to iV_{oc}.

3.4 VALIDATION EXPERIMENTS

To ensure correct operation of each PL measurement setup and validate the self-consistent calibration procedure, samples are measured in each system and a comparable other system.

3.4.1 COMPARISON TO SUNS-V_{OC}

A completed solar cell was measured in the system with beam splitter setup described in Section 3.2.1. Both QSSPL and V_{oc} were measured simultaneously. The injection-dependent τ_{eff} was calculated independently using each of the V_{oc} and the PL signals. The τ_{eff} was calculated from PL using the self-consistent calibration procedure described in Section 3.3.1; and independently calculated from V_{oc} using Equations (2-18) and (2-29).

The measured sample was a standard 156 cm^2 PERC cell fabricated on a commercial grade 180 μm thick, 1.5 Ωcm p-type monocrystalline Si wafer. Due to limitations of the maximum sample size in the measurement set up, the cell was cut to 3×3 cm^2 for analysis. The results are shown in Fig. 3-6, with excellent quantitative agreement (in the range of 10 %) observed between τ_{eff} determined from QSSPL and QSSV_{oc}. It is

emphasised that the absolute calibration of the PL data was achieved independently using the self-consistent method, with no cross calibration against the V_{oc} based data.
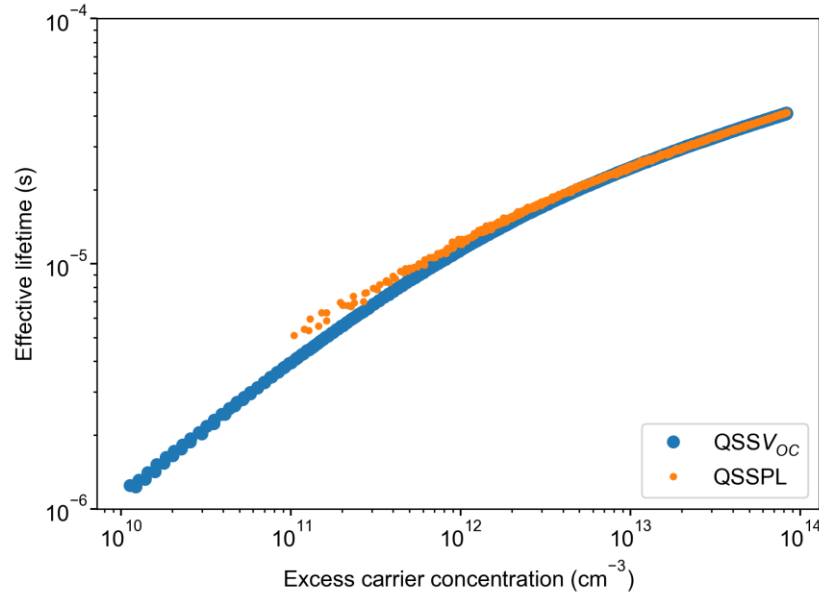
Fig. 3-6: Effective lifetime of validation sample measured by Suns-V_{oc} and QSSPL.

3.4.2 COMPARISON TO QSSPC

The full area illumination setup was validated by comparing the QSSPL measurements of the double side diffused and passivated experimental samples from Chapter 5 to separate QSSPC measurements of the same samples, made on a Sinton Instruments WCT-120 system [43]. The flash lamp on the Sinton system was filtered using the same KG-3 glass filter as the flash lamp from the QSSPL measurements so that the spectrum of incident light in each measurement was comparable. Refer to Section 5.2 for complete details of the samples.

Data from the QSSPC and QSSPL measurements of each sample are presented in Fig. 3-7. The lifetime data agree well (within 20 %) across the entire injection range for all samples. The small differences between the measurements are attributed to the difference in area of sensitivity between the systems. The QSSPL measurement area is approximately 0.63 cm^2 compared to the QSSPC measurement area, which is approximately 12.6 cm^2. The reduction in lifetimes in the lower injection range is attributed to edge recombination caused by the laser cleaving process.
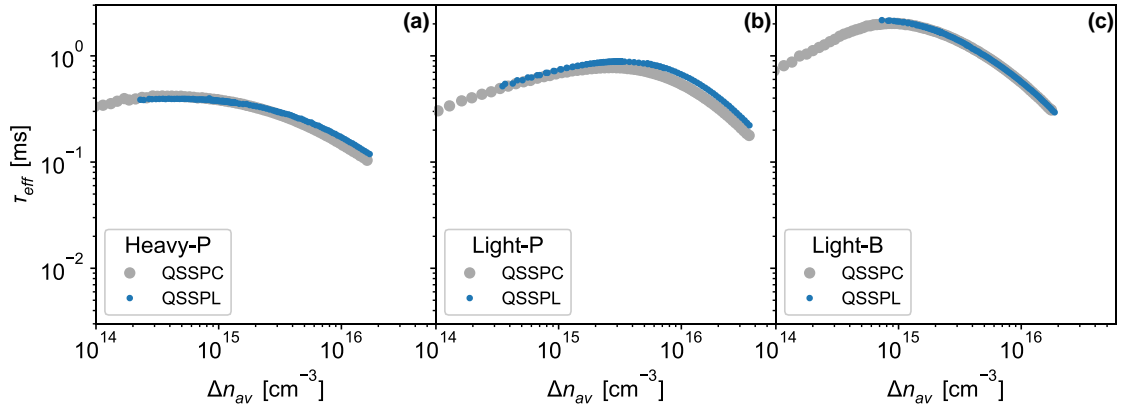
Fig. 3-7: Injection dependent τ_{eff} data measured by QSSPL and QSSPC for three double side diffused and passivated samples.

3.5 CHAPTER SUMMARY

QSSPL and Suns-PL are potentially useful techniques to study recombination of metallised surfaces because they are unaffected by the conductivity of the metal and can be applied to samples at any stage of processing. This chapter described the development of two different measurement setups that are used to perform experiments in this thesis. The second developed system presents a useful advance because it enables large illumination areas combined with PL detection from a local area of interest. Previous systems have used apertures to limit the area of local PL detection [76]. However, this is not appropriate for many of the metallised samples considered in this thesis because the high lateral conductivity provided by the metal would allow current to flow from illuminated to aperture shaded regions and cause errors. The lens and tube setup described in Section 3.2.2 avoids this problem.

The self-consistent calibration procedure was described, which enables simplified experiments compared to some other PL based work [12] because no comparison to a second sample or other measurement technique is required. Critical components in the measurement setup, which enable the calibration procedure to be applied accurately, were also described. These include an InGaAs photodiode and fast transimpedance pre-amplifier to enable accurate time response of the PL signal, and a laser illumination source that can be modulated.

Both measurement setups were validated experimentally against alternative measurement techniques and shown to be accurate.

CHAPTER 4: COMPARISON OF SUNS-V_{OC} AND SUNS-PHOTOLUMINESCENCE

Illumination intensity dependent open circuit voltage measurements, commonly known as Suns-V_{oc}, are often used to measure the current-voltage characteristic of a solar cell, without the impact of series resistance. Deviations at high illumination levels between Suns-V_{oc} measurements and contactless measurements, such as injection-dependent photoluminescence (Suns-PL), have previously been reported [53]. Using the system described in Section 3.2.1, these deviations are analysed in detail in this chapter and shown to cause significant errors when converting Suns-V_{oc} data to injection-dependent minority carrier lifetimes. This error is shown to be further propagated to calculations of J_{0s} if the Kane-Swanson method is applied to the erroneous lifetime data. Numerical modelling is used to identify shading and contact recombination as main causes of these deviations. Experimental data are used to demonstrate the magnitude of this effect for a range of different cell types.**

4.1 INTRODUCTION

From the discussion in Section 2.2.2 the class of dynamic characterisation techniques has been established. Contacted Suns-V_{oc} measurements and contactless lifetime measurements are two such techniques. Lifetime measurements can be converted to iV_{oc} [7]; and V_{oc} measurements can be used to determine the lifetime of the underlying material structure [8]. This conversion procedure is robust if: (a) the sample has a small fraction of voltage independent carriers [85]; and (b) Δn and thus the local diode voltage, is laterally uniform. This chapter focuses on the impact of the latter issue, which can result in large errors if not considered. The former issue, i.e. the impact of voltage independent carriers has recently been discussed by Juhl *et al.* [85].

Deviations of Suns-V_{oc} measurements from ideal diode behaviour have been studied previously. These deviations have been attributed to the impact of a Schottky diode at the rear of a cell [51], and the influence of non-uniform illumination, recombination and lateral series resistance [86]–[88]. Deviations between Suns-V_{oc} and iV_{oc} measurements of the same sample at high illumination intensities (1 to 10 suns) have previously been reported in the literature [50], [53], [57]. These reported deviations are explained in depth in this chapter using simulations.

** Note: This chapter is significantly based on the following peer-reviewed journal publication:
R. Dumbrell, M. K. Juhl, T. Trupke, and Z. Hameiri, "Comparison of terminal and implied open-circuit voltage measurements," *IEEE Journal of Photovoltaics*, vol. 7, no. 5, pp. 1376–1383, 2017.

Conversion from V_{oc} to τ_{eff} has recently been suggested as a means to estimate the effective J_{0s} of finished cells [89]. The conversion of Suns-V_{oc} data into injection-dependent lifetimes and subsequent analysis of the high injection data according to the Kane-Swanson method is problematic in this context, because this analysis is typically performed at high illumination intensities at which the above mentioned deviations are substantial.

In this chapter, using numerical modelling, it is demonstrated that deviations between Suns-PL and Suns-V_{oc} measurements at high illumination intensities result from finite lateral series resistance in combination with non-uniform lateral generation and/or recombination. Moreover, the modelling demonstrates that a Suns-PL measurement is a realistic upper limit for the obtainable V_{oc} of typical devices. On the other hand, the actual terminal voltage in conventional cell designs is limited by shading and contact recombination induced by the front metal grid in combination with lateral series resistances. The modelling is supported by measurements of a range of solar cell types that exhibit the above deviations at high illumination intensities. The errors resulting from subsequent extraction of J_{0s} from this data are also demonstrated.

4.2 THEORY

From comparison of Equations (2-29), (2-9) and (2-18), we note that conversion from τ_{eff} to iV_{oc} is possible and the reverse conversion V_{oc} to $\tau_{eff,i}$ is also possible. The first conversion is commonly used in the literature [34] and is uncontroversial because of the definition of iV_{oc}. It is a parameter that describes the maximum V_{oc} possible to obtain, on average, from a particular area of a sample. It follows directly from a measurement of Δn_{av} using QSSPC or QSSPL. Crucially though, it is not the same as V_{oc}, as discussed below.

The reverse conversion of a Suns-V_{oc} measurement from V_{oc} to $\tau_{eff,i}$, though, requires more explicit assumptions because it is a terminal based measurement. The measured V_{oc} is strictly defined at the probe point. The assumptions of the conversion to $\tau_{eff,i}$, an area averaged quantity, are thus:

1. Δn at the surface is not significantly different from Δn_{av}. That is, the excess carrier profile with depth is uniform.
2. Δn underneath the metal contact, is the same as Δn in non-metallised regions. That is, the lateral excess carrier profile is uniform.

Comparison of iV_{oc} and V_{oc}, or τ_{eff} and $\tau_{eff,i}$, will result in errors if either of these two assumptions fails. This chapter will show that the second assumption fails for standard front junction devices at high illumination intensities due to lateral variations in recombination and generation rates between the region under the metal grid compared to the non-metallised regions. Such variations cause lateral carrier flows and corresponding voltage drops across lateral series resistances. Under these conditions iV_{oc} overestimates V_{oc}, while the $\tau_{eff,i}$ derived from Suns-V_{oc} data will underestimate τ_{eff}. The magnitude of this voltage drop is strongly dependent on the illumination intensity. Thus, the deviations between τ_{eff} (as determined by bulk and surface recombination) and $\tau_{eff,i}$ increases with illumination intensity. The common Kane and Swanson analysis [59], which is based on measurements of τ_{eff} under high injection conditions, is therefore inaccurate if $\tau_{eff,i}$ is used.

4.3 MODELLING

The above deviations were investigated with Griddler 2.5 Pro, a two-dimensional finite element modelling software for solar cells [75]. The device modelled was a front junction, *p*-type base cell based on a published reference parameter set for a "Conventional Cell" [90]; the parameters of the base cell are summarised in Table 4-1.

Table 4-1: Base cell model design parameters.

Parameter (unit)	Value
Number of busbars	3
Busbar width (mm)	1.3
Number of fingers	75
Finger width (μm)	60
Cell area (mm^2)	156×156
Cell shape	Square
Resistivity (Ωcm)	2
Front non-metallised region saturation current density J_{0s} (fA/cm^2)	200
Front metallised region saturation current density J_{0m} (fA/cm^2)	600
Rear J_{0m} (fA/cm^2)	520
Emitter sheet resistance R_{sht} (Ω/□)	75
Front metal resistance R_{met} (mΩ/□)	3.75
Front metal contact resistance R_{con} (m$\Omega \cdot$cm^2)	0.012

In Griddler, the solar cell is simulated as a mesh of interconnected diodes. A terminal voltage and a PL image are output parameters. The PL image is determined from the local diode voltage at each node in the mesh. The terminal V_{oc} is calculated as the average diode voltage at the busbars. Simulations were performed with the device at open circuit under illumination intensities between 0.001 and 1000 suns, where one sun was defined as the incident light that generates current density of 39.6 mA/cm^2 in the unshaded regions of the cell. The optical transparency of the front metal was set to zero

so that there was no light generated current in these regions. The Suns-V_{oc} curve was calculated using data pairs of the reported terminal V_{oc} and the illumination intensity. The relative PL intensity (I_{PL}) was calculated as the mean value of the local PL intensity across the entire PL image. Following the discussion in Section 2.2.1.3, I_{PL} was converted to iV_{oc} with

$$iV_{oc} = \frac{kT}{q}\ln(C \cdot I_{PL}) \tag{4-1}$$

where C is a scaling factor. The scaling factor was determined for each simulation such that V_{oc} and iV_{oc} matched at 0.001 suns, and the same C factor was then used for all other data points at higher intensities. Combining the calculated iV_{oc} and the illumination intensity yielded the Suns-PL data. It is noted that the impact of voltage independent carriers usually has to be accounted for in the conversion of I_{PL} into iV_{oc}, as demonstrated in Ref. [91]. However, this is not required here, since Griddler simulations do not include that effect.

Fig. 4-1 shows the simulated Suns-V_{oc} and Suns-PL curve for the base cell with the absolute difference between iV_{oc} and V_{oc} plotted against the right hand side vertical axis. The simulation shows that at one sun intensity iV_{oc} is approximately 1 mV higher than V_{oc} and that this difference increases non-linearly towards higher illumination intensities. It is noted that at the highest intensity simulated here (equivalent to 1000 suns intensity) the difference reaches 26 mV, which corresponds to a substantial underestimation of the effective lifetime by more than a factor of two at room temperature according to the conversion procedure outlined in Section 4.2. It is also noted that these modelling results are qualitatively consistent with the experimental data of Trupke *et al.* [53], in which the discrepancy between terminal voltage and implied voltage from PL data was first observed.

The impact of specific cell parameters on the difference between iV_{oc} and V_{oc} is now investigated via simulations. These parameters include: the silicon-metal interface recombination, busbar width, front side series resistance and front surface recombination. The impact of each parameter is investigated by changing its value relative to the above base case scenario. Griddler simulates recombination using a two-diode model (see Eq. (2-16)) at each node. Separate J_{01} and J_{02} terms for the front and rear of the cell for both the illuminated and metallised regions are defined. For simplicity, all J_{02} values were set to zero and all rear surface and bulk parameters of the cell were kept constant for all simulations. Edge recombination parameters were also set to zero. Variations in front

surface recombination in the non-metallised and metallised regions were simulated by varying the respective J_{01} parameter for each region. These parameters are referred to in this study as J_{0s} and J_{0m}, respectively.
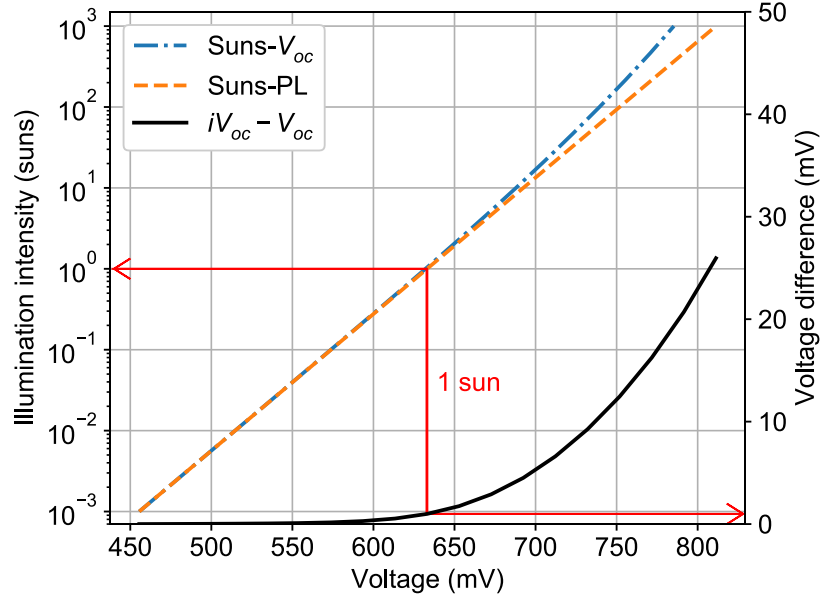
Fig. 4-1: Simulated Suns-V_{oc} and Suns-PL of the base cell model (left axis). The solid line represents the difference between iV_{oc} and V_{oc} as a function of iV_{oc} (right axis). Red arrows indicate one sun illumination intensity.

4.3.1 METAL RECOMBINATION AND SHADING

The front metal contact causes both non-uniform generation and non-uniform recombination. The shading by the metal results in practically no generation underneath the metal. In these simulations, zero generation rate underneath the contact is assumed, which thus represents a worst-case scenario. In reality, some generation will usually occur underneath the contact due to scattering of long wavelength light off the rear surface. At the same time, the metal-silicon interface typically has high surface recombination velocity compared to the non-metallised region of the front surface. In the base cell simulation, this is represented by J_{0m} being three times higher than J_{0s}. These two effects were studied in Griddler by varying J_{0m} of the front metallised region (as a proxy for the metal interface recombination saturation current density) and the busbar width (increasing the fraction of metal shading). The other simulation parameters were set to their base values. The results of the simulations are shown in Fig. 4-2.

When J_{0s} and J_{0m} are equal there is no lateral non-uniformity in recombination, only the effect of shading remains. This situation is represented in Fig. 4-2 (a) where both J_{0m} and J_{0s} were 200 fA/cm². Substantial deviations between iV_{oc} and V_{oc} are still observed in this case. The deviations increase with a doubling and tripling of the busbar width to 2.6 and

3.9 mm. Interestingly, the increased deviation is slightly non-linear. This can be explained by the increased busbar width being compensated by shorter fingers. Thus, although the imbalance between generation and recombination is changed linearly, the shorter finger length results in a smaller voltage drop than would be expected for constant finger lengths.
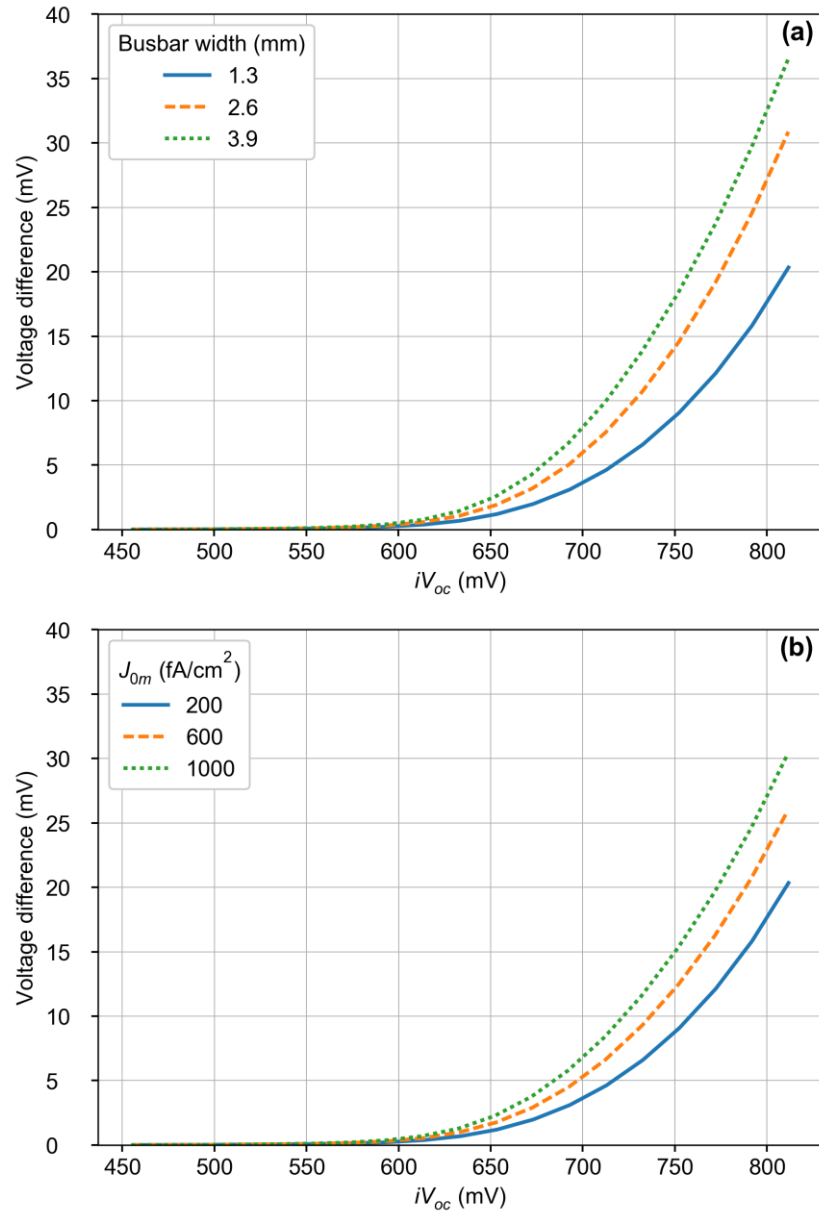
Fig. 4-2: The combined effects of shading and metal recombination on the *iV$_{oc}$-V$_{oc}$* difference. (a) Shading only simulation with *J$_{0s}$* and *J$_{0m}$* both 200 fA/cm²; increasing busbar width increases deviation. (b) Combined shading and metal recombination simulation with busbar width at base level (1.3 mm) and *J$_{0m}$* increased.

Increasing deviations are also found for constant busbar width and increasing *J$_{0m}$*, as shown in Fig. 4-2 (b). *J$_{0m}$* was increased from 200 fA/cm² to the base cell level of 600 fA/cm² and above that to 1000 fA/cm². These increases are small compared to the

difference induced by the shading alone though, which suggests that for the modelled base cell, the primary driver of the deviation is the shading rather than the metal-induced recombination.

4.3.2 RESISTANCE

In the presence of lateral differences in carrier generation or recombination the lateral series resistance determines the lateral diode voltage variations, as carriers flow laterally via the series resistance to equalise carrier density (or voltage) gradients. To simulate the effects of the lateral series resistance, the front metal resistance (R_{met}) and the front heavily doped region sheet resistance (R_{sht}) were varied from the base cell value, so that the effect of each parameter could be independently assessed. Note that metal resistances in Griddler are input as sheet resistances, with units $\Omega/\square$. These can be converted to a more easily measured quantity like metal line resistance in units of Ω/cm by dividing by the finger width (60 μm in Ref. [90]).

The impact of R_{sht} on the deviation between V_{oc} and iV_{oc} is shown in Fig. 4-3(a) with R_{met} set to the base value. For R_{sht} = 0 m$\Omega/\square$ there is practically no deviation for most of the range of iV_{oc}, with only a very small deviation at very high iV_{oc}, as shown by the solid blue curve. This is attributed to the finite contact resistance which becomes significant at such high carrier densities. This minimal deviation is expected because in this unrealistic case carriers flow unimpeded from all parts of the cell to the busbar bypassing the metal finger resistance. For R_{sht} values in the range used for typical cells (30–150 $\Omega/\square$) there is a deviation observed, but the magnitude of this deviation is nearly the same for all values of R_{sht}. This deviation is relatively insensitive to the simulated range of sheet resistances, demonstrating that the dominant voltage drop occurs over another resistive element within the cell. In these cases, the emitter resistance is much larger than the finger resistance and thus the magnitude of the deviation is dominated by the finger resistance.

The impact of varying R_{met} with R_{sht} set to the base value is shown in Fig. 4-3(b). For R_{met} = 0 m$\Omega/\square$ (solid blue curve) deviations are observed, which represent voltage drops caused by carriers flowing laterally through the emitter to get to the metal fingers. When R_{met} is increased to the range of realistic values (1.5–7.5 m$\Omega/\square$) the deviations increase, which represents a further voltage drop as carriers flow through the metal fingers. The deviations are more sensitive to the value of R_{met} than the value of R_{sht}. This shows that there is substantial lateral current flow in the metal grid at V_{oc} conditions.

Fig. 4-2 and Fig. 4-3 focused on the deviations between V_{oc} and iV_{oc}. Fig. 4-4 shows the actual Suns-V_{oc} and Suns-PL data for R_{sht} values of 0 and 75 $\Omega/\square$ and all other

parameters set to the base value. The V_{oc} data show the previously described behaviour, i.e. reduced voltage (by about 23 mV) for higher lateral resistance. In contrast, the inset of Fig. 4-4 shows that iV_{oc} is approximately 1 mV higher for $R_{sht} = 75$ Ω/□, compared to $R_{sht} = 0$. In the higher resistance case, the carriers which are unable to flow to the metal contact instead recombine in the illuminated region, thus increasing the measured iV_{oc} and decreasing the measured V_{oc}. Since the iV_{oc} shows a much weaker dependence on the resistance network, it is suggested that it can be used as an upper limit for the device's obtainable V_{oc}.
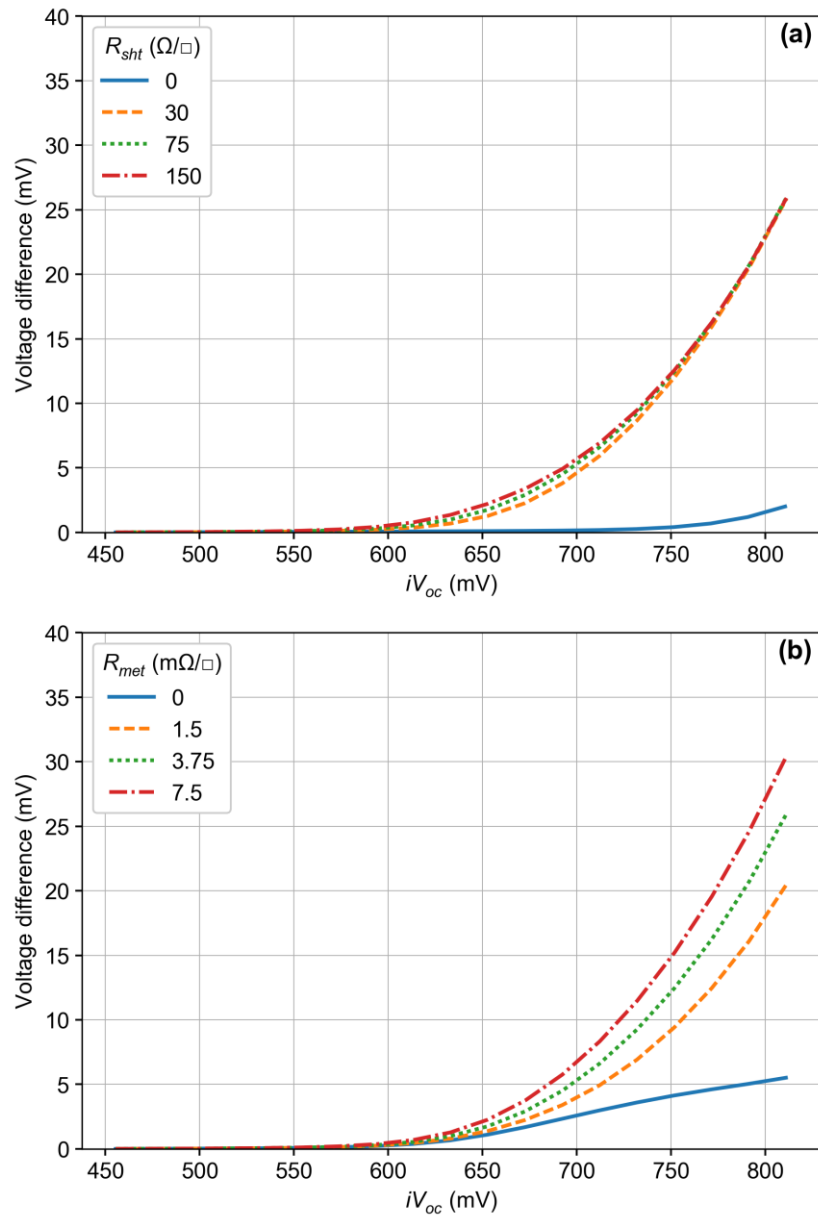
Fig. 4-3: iV_{oc}-V_{oc} **difference for: (a) Varied front emitter sheet resistance with** $R_{met} = 3.75$ mΩ/□**; and (b) varied front metal resistance with** $R_{sht} = 75$ Ω/□**.**
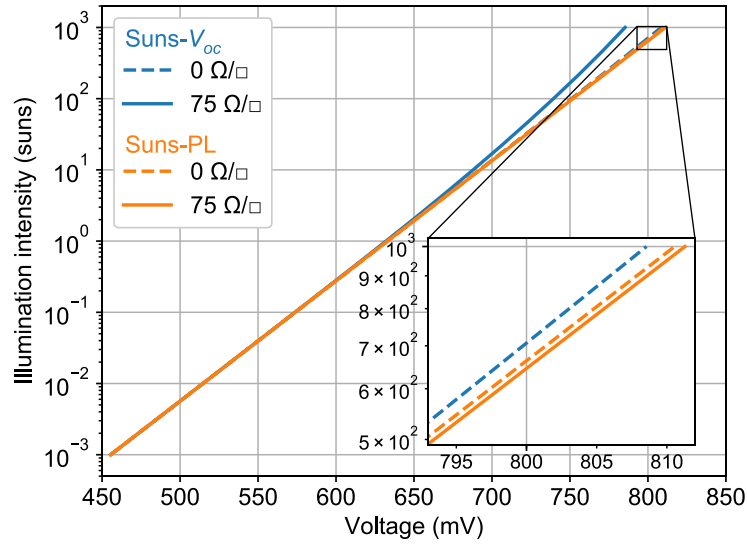
Fig. 4-4: Suns-V_{oc} and Suns-PL plots for R_{sht} = 0 Ω/□ and R_{sht} = 75 Ω/□. Inset: iV_{oc} is higher for higher R_{sht} because carriers are "trapped" by the lateral series resistance.

4.3.3 SURFACE RECOMBINATION

The impact of reduced surface recombination was simulated by varying J_{0s} from the baseline value of J_{0s} = 200 fA/cm^2 to 100 fA/cm^2 and 0 fA/cm^2, while all other parameters were held constant at the base cell values. The resulting deviations between iV_{oc} and V_{oc} are shown in Fig. 4-5. Compared to the previously discussed parameters, the voltage deviation is relatively insensitive to J_{0s}. Increasing J_{0s} changes both V_{oc} and iV_{oc} by approximately the same amount but has almost no effect on the voltage difference.
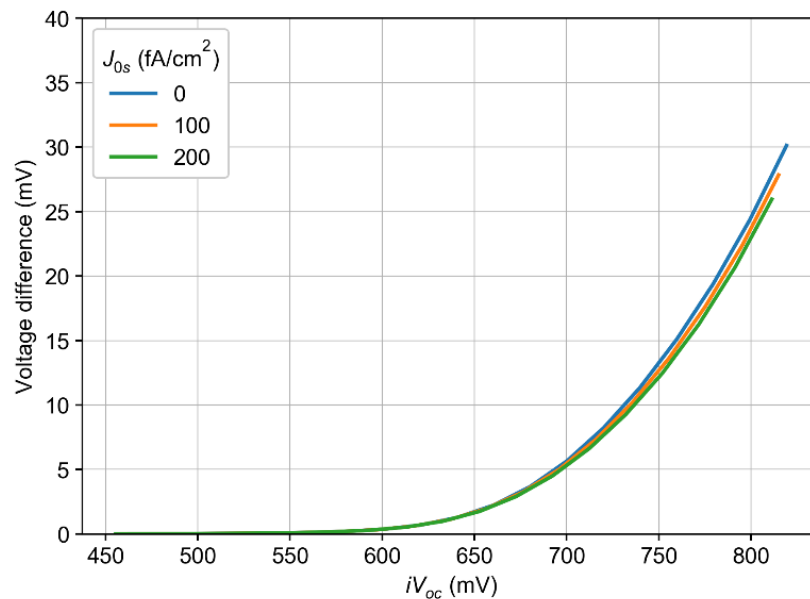
Fig. 4-5: The deviation of the V_{oc} from the iV_{oc} when J_{0s} was reduced while other parameters remained constant.

4.3.4 MODELLING CONCLUSIONS

This section explored the origins of previously reported differences between V_{oc} and iV_{oc} measurements at high illumination intensities. It was found that deviations occur for devices with laterally non-uniform generation or recombination rates in combination with finite lateral series resistances. Without laterally non-uniform generation or recombination, there is no Δn gradient to drive the lateral flow of carriers necessary to create the iV_{oc}-V_{oc} difference. The terminal voltage measurement then represents Δn and thus lifetime in the non-metallised regions. Similarly, if lateral series resistances are near zero then carriers flow unimpeded to equalise Δn gradients and no voltage difference is observed. Although in that case, the terminal voltage, and therefore $\tau_{eff,i}$, no longer represent the effective lifetime of the bulk and surfaces alone, but a convoluted lifetime that also includes the metal contact recombination and shading.

However, in the presence of lateral non-uniformity in the generation and recombination (as is the case in regular front and rear metallised solar cells), the result is a lower carrier density at the metal contact compared to the illuminated region, which is reflected in a lower V_{oc} compared to iV_{oc}. At one sun equivalent illumination, the deviations between V_{oc} and iV_{oc} are generally found to be small, which is expected, since cell designs are optimised to enable lateral transport of the corresponding photogenerated current densities without substantial voltage losses. However, at higher illumination intensity, at which J_{0s} analysis is typically carried out to separate bulk and surface recombination effects, the above deviations result in substantial errors. Ideally, an implied or measured voltage that is not affected at all by metal shading or recombination underneath metal contacts, which thus represents the bulk and surface recombination, would be used for that analysis. The data in Fig. 4-4 show that both terminal V_{oc} and iV_{oc} from PL are affected by lateral voltage loss in typical cells, but the resulting deviations from the ideal scenario are much stronger for terminal voltage measurements (up to 23 mV) than for the PL measurements (where they do not exceed 1mV even at 1000 Suns illumination intensity). The Suns-PL technique thus appears to be the best practical approach.

4.4 EXPERIMENT

The theoretically predicted deviations between V_{oc} and iV_{oc} are now demonstrated experimentally by measurements of different types of solar cells. The investigated cells are: a cell with non-optimised laser fired rear contacts (LFC) [92], causing a Schottky diode at the rear contact (obtained from Ref. [51]); a token cut from a commercially-produced passivated emitter and rear cell (PERC); and a token cut from a standard screen printed aluminium back surface field (Al-BSF) cell, as set out in Table 4-2.

Table 4-2: Experimental solar cell details

Sample name	Front grid shading fraction (%)	Rear design	Size
LFC	5.8	LFC PERC	2 cm × 2 cm laboratory solar cell
PERC	7.0	PERC	3 cm × 3 cm token
BSF	7.8	Al-BSF	3 cm × 3 cm token

The cells were measured with the measurement setup, which enables dynamic PL detection from the front side of metallised devices, as discussed in Section 3.2.1. The setup simultaneously measures terminal V_{oc}, I_{PL} and relative illumination intensity. iV_{oc} was calculated from the PL signal using Eq. (2-9), with Δn_{av} calculated from Eq. (2-24). A_i is calculated such that iV_{oc} matches the V_{oc} measurements at low light intensity. Note that the two step conversion of I_{PL} to Δn to iV_{oc} was used instead of a direct conversion to iV_{oc} so that G_{net} could be correctly calculated (see Eq. (2-29)).

The relative illumination intensity was converted to absolute units using a separate measurement of Suns-V_{oc} using a laser system for which the incident photon flux is known accurately. For simplicity, in this section one sun illumination intensity is defined identically to the simulations in Section 4.3. We estimate a relative error of ±10 % in the absolute illumination intensity. The illumination pulse time is short for all measurements such that the change in sample temperature has a negligible effect on the measured voltage.

4.4.1 RESULTS AND DISCUSSION

The Suns-V_{oc} and Suns-PL plots of the three solar cells are shown in Fig. 4-6. Strong deviation between V_{oc} and iV_{oc} are observed for all three solar cells at high light intensities. Even at one sun illumination intensity there is a 4 mV difference for the LFC and the PERC solar cells and a 2 mV difference for the BSF sample. This demonstrates that this effect is significant under open circuit conditions even at one-Sun intensity for the most common cell structures.

For all three measured cells, the Suns-PL curves can be modelled as a single diode with ideality factors m in the range 1.2-1.4. Only at very high voltages does the Suns-PL curve deviate from the single diode behaviour, possibly indicating the onset of the dominance of Auger recombination at high carrier injection levels [17]. The Suns-V_{oc} curves, however, are not readily modelled as single diodes. The deviations from the one diode model are an indication that carriers are no longer able to reach the metal contacts of the device without significant voltage losses.
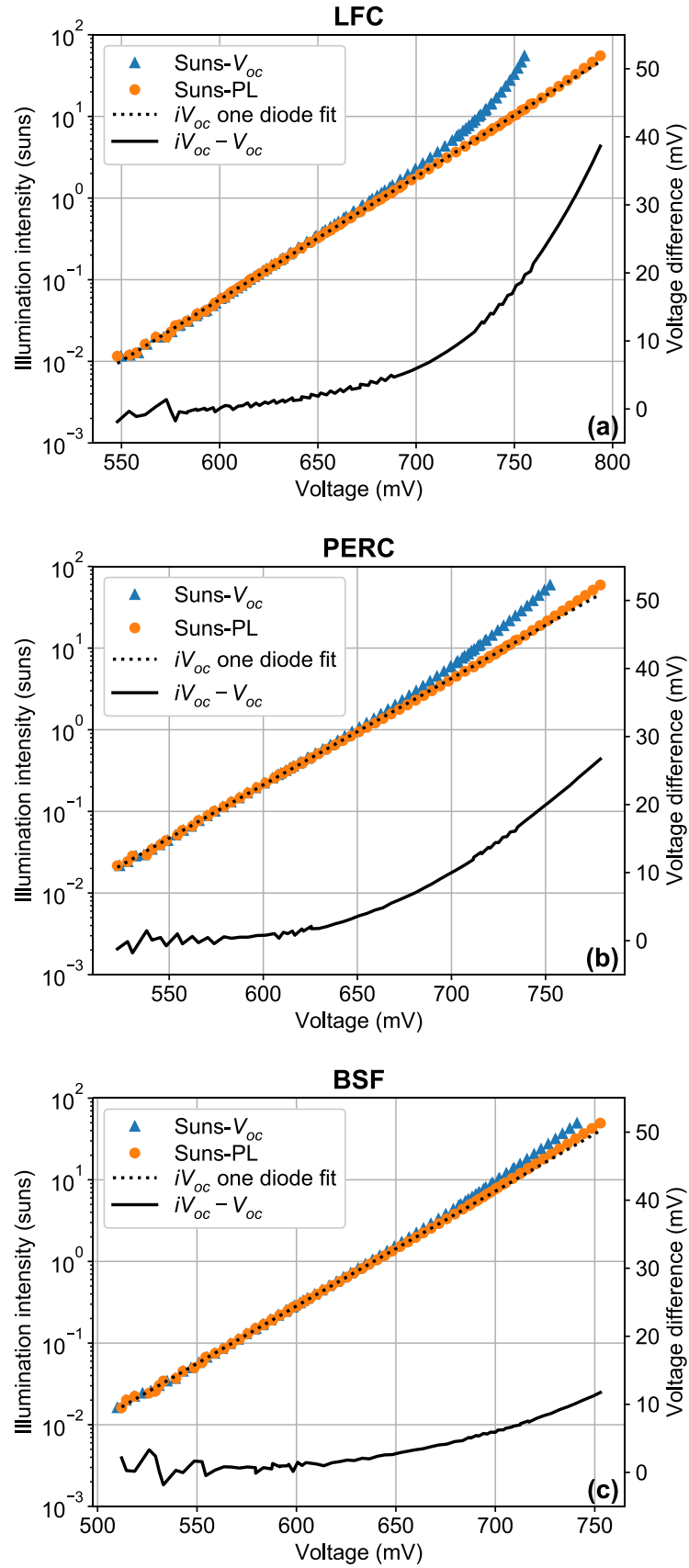
Fig. 4-6: Suns-V_{oc} and Suns-PL data measured on: (a) the LFC sample, (b) the PERC cell, (c) the BSF cell. The difference between iV_{oc} and V_{oc} (solid black line) is plotted on the right vertical axis against iV_{oc}.

The measurement of the LFC sample, shown in Fig. 4-6 (a), shows strong deviation between the iV_{oc} and V_{oc} at high illumination intensities. In the original study from which this sample was taken, some cells exhibited even more extreme behaviour, with a reduction in V_{oc} observed with increasing illumination intensity [51]. However, the Suns-PL data show that the recombination activity and the implied current-voltage (*I-V*) curve of the cell have normal behaviour. In this specific cell the deviations between V_{oc} and iV_{oc} are known to be strongly dominated by the presence of a Schottky contact on the rear surface [51], but it is noteworthy that an impact of the effects of lateral current flow as described above could not be ruled out based on this measurement alone.

The BSF sample and PERC sample are both cut from commercially manufactured cells. Because they are cut from a region that includes a segment of busbar, the metal shading area fraction is higher than for a typical full-size industrial cell. This is expected to exaggerate the shading effects discussed in Section 4.3. However, given that the shading fraction of the two samples is similar, a comparison between the two samples is still instructive of the difference between the two cell types. The difference between iV_{oc} and V_{oc} is higher for the PERC cell. This difference is attributed to the different rear contact design of the two cells. The BSF cell has a uniform full area alloyed Al rear contact, which forms a low resistance path across the entire rear of the device. Therefore, the voltage is uniformly distributed at the rear and no extra lateral currents flow. In contrast, the local rear contacts in the PERC cell create a laterally non-uniform resistance and rear surface recombination rate and therefore cause a voltage loss, which contributes to the increased deviation between iV_{oc} and V_{oc} that was measured. These measurements demonstrate that while the PERC structure reduces overall recombination to increase its V_{oc}, its improved contacting is not as efficient at reaching the maximum obtainable V_{oc}.

4.5 ERROR IN $J_{0s,TOT}$ CALCULATION

The deviations demonstrated in this paper are consequential when calculating J_{0s} from Suns-V_{oc} measurements, as has been suggested elsewhere [89]. In this method, the measured V_{oc} is converted into $\tau_{eff,i}$ by combining Equations (2-18) and (2-29), and $J_{0s,tot}$ is then determined by applying the modified Kane-Swanson method (see Section 2.3.1). Note that the calculated $J_{0s,tot}$ represents the combined front and rear surface recombination.

The above analysis procedure was applied to the Griddler-simulated Suns-V_{oc} and Suns-PL data of the base cell in Fig. 4-1. For the analysis of the simulated data, Auger lifetime correction and the injection dependence of $n_{i,eff}$ was neglected because Griddler

does not simulate those effects. $J_{0s,tot}$ extracted from the Suns-V_{oc} data was 3667 fA/cm^2 and 995 fA/cm^2 from the Suns-PL data, respectively. Using the Suns-V_{oc} data thus causes a more than threefold overestimation of the actual $J_{0s,tot}$. This shows that these effects have a significant effect on the accuracy of the extracted data.

The same analysis was then applied to the Suns-V_{oc} and Suns-PL measurements of the PERC and BSF cells discussed in Section 4.4. The τ_{eff} from the PL measurements is observed to be significantly higher (i.e. the inverse lifetime lower, as shown) at high injection levels than $\tau_{eff,i}$ from the V_{oc} measurement for both samples, in agreement with the previously discussed theory. The data used to extract $J_{0s,tot}$ for the PERC cell are shown in Fig. 4-7. The slopes of the linear fits clearly differ strongly for the iV_{oc} and V_{oc} data. The higher slope for the V_{oc} data results in an overestimation of J_{0s}. The extracted $J_{0s,tot}$ values for both samples are shown in Table 4-3. The $\tau_{eff,i}$ data from V_{oc} measurements provided $J_{0s,tot}$ values that are two to seven times larger than from the PL based method, demonstrating that the above artefacts can be very substantial.
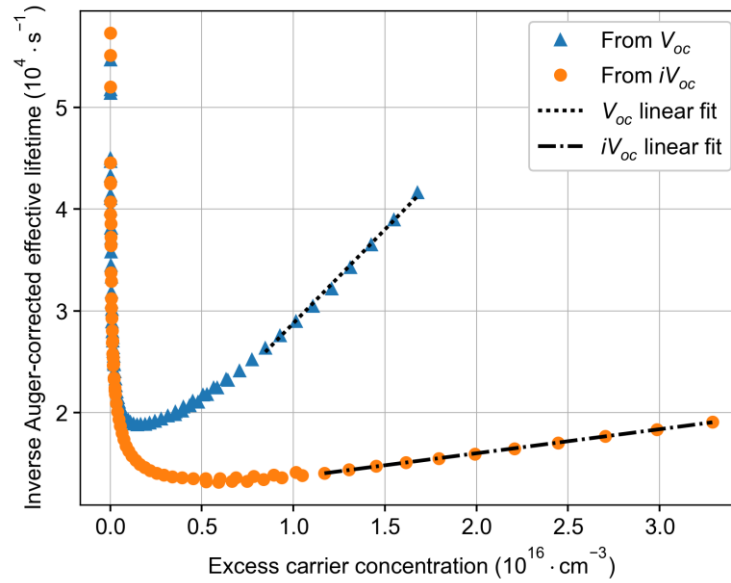
Fig. 4-7: Inverse Auger-corrected τ_{eff} extracted from V_{oc} and iV_{oc} measurements of the PERC cell with N_{dop} = 1.5 × 10^{16} cm^{-3}. Linear fits result in significantly different slopes and thus $J_{0s,tot}$ values.

It should be noted that strictly, the $J_{0s,tot}$ extraction method requires high injection level conditions which could not be achieved due to limitations of the experimental setup. The values obtained here are still indicative of the resulting relative errors that results from applying the method to V_{oc} based data as opposed to PL based iV_{oc} measurements.

The data in Table 4-3 show that significant errors can result when the terminal V_{oc} is converted to $\tau_{eff,i}$ and used to extract surface recombination parameters at high injection.

Table 4-3: Results of $J_{0s,tot}$ analysis of cell data

Sample	J_{0s} from iV_{oc} (fA/cm²)	J_{0s} from V_{oc} (fA/cm²)	Error
BSF	239	640	168 %
PERC	100	746	648 %

4.6 CONCLUSIONS

Deviations between the measured terminal V_{oc} and iV_{oc} from PL data at high illumination intensities were investigated. Through numerical modelling it was shown that the combination of lateral non-uniformity in generation rate and/or recombination rate in combination with a finite lateral series resistance can cause significant deviations between these measurement parameters. The higher the series resistance and the greater the lateral imbalance in generation or recombination between normal cell regions and metal contacted regions, the greater the observed deviations between the measurements. Through combined measurements of Suns-V_{oc} and Suns-PL this effect was observed experimentally on two typical cell structures. A third cell with a known Schottky contact was also observed to demonstrate the deviation. In general terms, deviations between iV_{oc} and terminal V_{oc} will likely be a combination of the effects discussed above and Schottky contact effects.

Interpretation of Suns-V_{oc} data in terms of injection-dependent minority carrier lifetime data and subsequent calculation of the surface recombination parameters based on the common Kane-Swanson analysis methodology resulted in relative errors up to a factor of seven when the terminal V_{oc} measurements were used compared to the PL measurements. This procedure is thus likely to result in significant errors for most typical cell designs because the lateral resistance network is optimised for one sun operation, but the measurement procedure requires illumination intensities greatly exceeding one sun to reach high carrier injection conditions. The combination of Suns-PL and Suns-V_{oc} appears to be an excellent combination. The Suns-PL data provide the basis for accurate injection-dependent lifetime data on cells, while Suns-V_{oc} can be used for accurate calibration of the PL data at low illumination intensities. The Suns-PL data were noted to provide a realistic upper limit for the Suns-V_{oc} data. Hence, comparison of the two data sets enables quantifying losses in V_{oc}, i.e. how much lower the actual voltage is at one sun illumination, compared to the voltage entitlement related to the bulk and surface properties.

CHAPTER 5: METAL CONTACT RECOMBINATION – FULL AREA METALLISATION

The surface recombination at metallised surfaces of a solar cell is of significant interest for cell process development, considering the limiting effect such recombination has on cell efficiency. As discussed in Section 2.3, this recombination is difficult to measure accurately, because the enhanced recombination at the metal contacts causes an inhomogeneous minority carrier profile, which limits the viability of conventional photoconductance-based recombination measurements. This inhomogeneity occurs as a function of depth into the wafer as well as laterally. This chapter exclusively explores the depth-based inhomogeneity, while the following Chapter 6 builds on the understanding developed in this chapter with the additional complexity of lateral non-uniformity. In this chapter, the developed full area illumination PL-based system (see Section 3.2.2) is used to measure the injection dependent effective lifetime of full area metallised samples. Several techniques to extract surface recombination parameters from these data are compared in detail. A simulation-based approach is shown to be superior to the modified Kane-Swanson methods, which are more commonly applied to data of this type, in the case where the depth profile of the minority carrier density is non-uniform. Further simulations and a detailed sensitivity analysis are used to support these conclusions.**

5.1 INTRODUCTION

As discussed in Section 2.3, accurate quantitative measurements of metal induced contact recombination losses are difficult to achieve because the enhanced recombination at the metallised surfaces compared to non-metallised surfaces causes non-uniformity in the local Δn. This chapter particularly focuses on investigating the impact of the non-uniform Δn with depth and the accompanying one-dimensional analysis.

Surface recombination of non-metallised samples is commonly determined from analysis of eddy current based PC carrier lifetime measurements, first demonstrated by Kane and Swanson [59]. The theory used to interpret such measurements has been improved since Kane and Swanson's original paper to account for Auger recombination and bandgap narrowing [61], and inhomogeneous minority carrier density profile [62]. However, this approach is difficult to apply to metallised samples accurately because

---

** Note: This chapter is significantly based on the following peer-reviewed journal publication:
R. Dumbrell, M. K. Juhl, T. Trupke, and Z. Hameiri, "Extracting metal contact recombination parameters from effective lifetime data," *IEEE Journal of Photovoltaics*, vol. 8, no. 6, pp. 1413–1420, 2018.

standard metal contacts dominate the measured PC signal. Thus, non-standard contacting schemes are required for PC measurements using these techniques [93].

Here, an alternative approach is established, which uses the developed front detection QSSPL measurement setup (See Section 3.2.2) to measure the injection dependent τ_{eff} of metallised samples. It is noted that recombination at the metallised surface is just a special case of surface recombination and thus, the commonly used Kane-Swanson analysis could potentially be applied to these QSSPL lifetime measurements. In this chapter, this analysis is compared to a more detailed modelling approach [94], which uses the curve fitting features of the simulation software Quokka version 2.5 [74]. It is shown that in many cases the frequently used Kane-Swanson analysis cannot be applied because the asymmetrical surface recombination causes a non-uniform Δn profile. Because the modelling approach accurately simulates the depth profile of Δn, the data extracted from the Quokka simulation are shown to be more accurate for measurements of this type. These issues are discussed in the context of metallised samples, but the conclusions are equally applicable to any case of significant non-uniformity in Δn profile, such as samples with low bulk lifetime under short wavelength illumination or significantly asymmetrical or high surface recombination.

5.2 EXPERIMENTAL METHODOLOGY

5.2.1 SAMPLE PREPARATION

To enable a useful comparison of the various analysis approaches, three samples were created with a simplified metallization procedure, so that a one-dimensional analysis could be applied. It is noted that most of the demonstrated limitations become even more pronounced when more complex metallization schemes, such as those for passivated emitter and rear contact cells, are considered.

The samples' details are summarised in Table 5-1. Two samples are 4 inch diameter p-type FZ Si wafers, symmetrically diffused with phosphorus (P) and symmetrically passivated with plasma-enhanced chemical vapor deposited (PECVD) silicon nitride (SiN$_x$). One sample had a heavy diffusion (90 Ω/□) on both sides, while a light diffusion (190 Ω/□) was applied on both surfaces of the other. The third sample is a 4 inch diameter n-type FZ Si wafer, symmetrically diffused with boron (150 Ω/□) and symmetrically passivated with 10 nm of atomic layer deposited (ALD) aluminium oxide (AlO$_x$) and capped with SiN$_x$. All three samples were annealed at 420 °C.

Table 5-1: Sample details

Name	Wafer	Diffusion sheet resistance ($\Omega/\square$)	Passivation
Heavy-P	*p*-type, 3 Ωcm, 280 µm	90	SiN_x
Light-P		190	
Light-B	*n*-type, 5 Ωcm, 710 µm	150	$AlO_x + SiN_x$

Each sample was cleaved into quarters and characterised using PL imaging [10]. The PL image was used to determine the quarter piece with the most laterally uniform Δn, and these samples were selected for subsequent analysis and processing. These pieces were measured with both the front detection QSSPL system and with a Sinton Instruments WCT-120 lifetime tester [43] for comparison and validation. The validation data are presented in Section 3.4.2. The dielectric layer was then removed from one side of each sample by masking the other side with photoresist and using a buffered oxide etch solution at room temperature. A 500 nm aluminium layer was then deposited on the bare Si surface by thermal evaporation. A second lifetime measurement was made with the QSSPL system after metallization.

5.2.2 EXPERIMENTAL SETUP

The QSSPL measurements were performed with the setup as described in Section 3.2.2. For these measurements, the 808 nm diode laser was pulsed up to approximately one sun equivalent illumination intensity to calibrate the PL signal self-consistently (see Section 3.3.1), and a xenon flash lamp with maximum intensity equivalent to approximately 30 suns was used to excite the samples to a higher injection level.

As discussed in Section 3.3.1, in the presence of high surface recombination velocity, dynamic calibration techniques (including self-consistent calibration) can result in erroneous calibration of lifetime data [83], [84]. In this experiment, the calibration is performed using an excitation modulation rate that is of the same order as the sample τ_{eff} and at low to intermediate injection level ($\Delta n / N_{dop} \leq 1$), where the surface recombination is low such that these effects are avoided, and the steady-state lifetime is obtained. Concerns related to the effects of non-uniform Δn on photon reabsorption are avoided by using the InGaAs PL sensor [39].

5.2.3 ANALYSIS APPROACH

The quantities obtained from the QSSPL measurements are G_{av} and Δn_{av}, and these can be combined to calculate τ_{eff}. As discussed in Section 2.3.1, a set of commonly used methods to extract J_{0s} from such lifetime data exist, based on the original method of Kane

and Swanson [59]. These methods extract $J_{0s,tot}$, the sum of the front and rear surface recombination and further assumptions about the samples structure must be made to infer J_{0s} of a particular surface. Importantly, they also assume that Δn is uniform in the sample such that the measured Δn_{av} can be assumed equal to Δn at the surface of interest. In this experiment the relevant parameter to extract from the data is J_{0m}, the saturation current density at the metallised surface. Thus, these assumptions have important consequences for interpreting the data. The discussion in Section 2.3.1 highlights a standard Kane-Swanson based method, as described by Blum *et al.* [61] and implemented in the Sinton Instruments WCT-120 lifetime tester, and an improved method, proposed by Kimmerle *et al.* [62], which attempts to account for finite Shockley-Read-Hall bulk lifetime (τ_{SRH}) and deviations from a uniform carrier profile resulting from a finite diffusion length. The metallised samples measured in this experiment do not meet the assumptions underlying these methods, thus both the standard approach and Kimmerle's approach are applied to establish the conditions where they can and cannot be accurately applied.

The general approach of these slope-based methods is to perform a linear fit to a plot of inverse corrected lifetime as a function of Δn_{av} at an injection level where τ_{eff} is dominated by surface recombination. Kane and Swanson suggested to use an injection level equivalent to ten times the doping density, though others have suggested five times the doping density can be more appropriate [65]. Below this injection level, τ_{eff} is heavily convolved with the impact of the bulk lifetime. However, when bulk doping densities of typical industrial Cz wafers are used, this range is impacted by a reduced diffusion length caused by Auger recombination preventing carrier recombination at the surface [62].

For both the Blum *et al.* and Kimmerle *et al.* methods, the quantity extracted is $J_{0s,tot}$. For the symmetrical samples measured before metallization, J_{0s} is assumed to be half of $J_{0s,tot}$. For the measurements after metallization, J_{0s} of the unmetallised surface is assumed to remain the same and J_{0m} is determined by subtracting that front J_{0s} from $J_{0s,tot}$. As will be shown, both techniques still incorporate assumptions that break down when attempting to apply them to the types of samples that are used to study metallised surface recombination.

As others have argued, analysis of surface recombination can potentially be improved by more detailed simulations [63], [94]–[96]. In the following analysis, we use Quokka v2.5 to fit simulated τ_{eff} data to our QSSPL measurements, following a similar approach to Janssen e*t al.* [94]. A simple one-dimensional structure was developed with a quasi-neutral bulk, and front and rear surfaces modelled as conductive boundaries. For each

sample, a generation rate profile was modelled in OPAL 2 [97] by combining the measured sample reflectance, flash lamp irradiance spectrum, and short pass filter transmission data. To analyse the symmetrically passivated sample data, an equal front and rear J_{0s} and a constant bulk lifetime (τ_{const}) were set as fit parameters. To fit the measured data from the metallised structure, the previously fitted front J_{0s} and τ_{const} were fixed in the model, and the rear J_{0m} was fitted.

All extraction techniques were applied using the same models for intrinsic recombination [17], mobility [98], and $n_{i,eff}$ using the bandgap narrowing model by Schenk [99]. Note that Quokka v2.5 uses a constant $n_{i,eff}$ calculated only from the doping dependence of the bandgap narrowing, but the Kane-Swanson based extraction techniques were implemented with the full injection level dependence.

5.3 RESULTS AND DISCUSSION

5.3.1 MEASUREMENTS

Lifetime data for each sample, measured before and after metallization are shown in Fig. 5-1 (a)-(c) and J_{0s} and J_{0m} extracted using the Kane-Swanson based techniques as a function of injection level are shown in Fig. 5-1 (d)-(f). The fitted Quokka data are also shown with the measured data in Fig. 5-1 (a)-(c). The J_{0s} and J_{0m} data extracted with each technique are summarised in Table 5-2 and Table 5-3, respectively.

Table 5-2: Apparent J_{0s} extracted with different methods before metallisation.

Sample	Blum	Kimmerle	Quokka	
	J_{0s} range (fA/cm^2)	J_{0s} range (fA/cm^2)	J_{0s} (fA/cm^2)	τ_{const} (µs)
Heavy-P	87-93	89-99	76	1262
Light-P	0-14	0-14	8	1281
Light-B	79-100	80-117	64	4577

Fig. 5-1 (d)-(f) shows the injection dependence of the apparent J_{0s} and J_{0m} that was extracted with the Kane-Swanson based techniques for each sample. The fitting range was limited to injection levels above the doping density. The extracted J_{0s} for sample Light-P was below zero (obviously a non-physical value) for Δn below approximately 4×10^{15} cm^{-3}, which highlights concerns in relation to the accuracy of the Kane-Swanson based extraction methods. This is attributed to the injection dependent lifetime exhibiting a maximum and the slope changing sign at this value. The apparent J_{0s} exhibited some injection dependence for all samples. The maximum range of extracted J_{0s} values was observed for sample Light-B, which ranged between 80 fA/cm^2 and 117 fA/cm^2, using
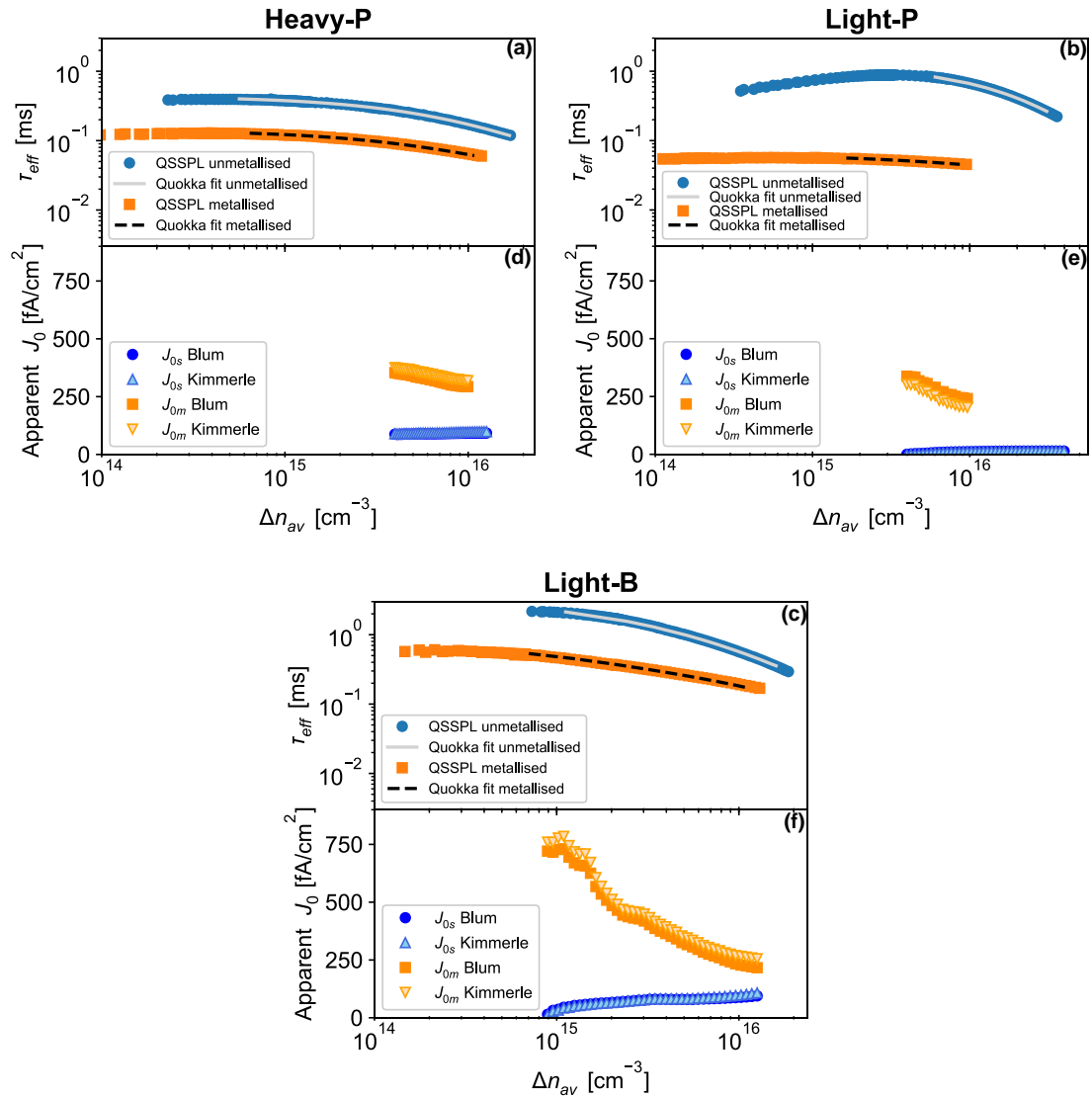
Fig. 5-1 (a)-(c) QSSPL measured τ_{eff} of each sample measured before and after metallization and Quokka fitted τ_{eff} . (d)-(f) Injection dependence of apparent J_{0s} and J_{0m} derived from the Kane-Swanson based techniques.

Kimmerle's method. As shown in Table 5-2, given the observed injection dependence of the Kane-Swanson based extracted J_{0s} values, there is good agreement with the J_{0s} values extracted using Quokka. For the Quokka fit of the non-metallised samples, two parameters were fitted to the data (J_{0s} and τ_{const}), while after metallization only a single fitting parameter was used (J_{0m}) using the fixed values obtained for J_{0s} and τ_{const} from the fits for the non-metallised samples. The Quokka fitting approach does not require assumptions about Δn being uniform with depth because the full depth dependence of the carrier distribution is simulated. The trade-off is that the accuracy of the extracted J_{0m} is more dependent on accurate knowledge of the illumination spectrum, sample optics and bulk lifetime. This study simplifies the bulk lifetime issue by including τ_{const} in the model and limiting the fit to an injection range above the maximum turning point in the lifetime data, where it is assumed that the bulk lifetime can be considered constant. This

assumption is also implicit in the Kane-Swanson based techniques because by taking the slope of the inverse lifetime, only the injection dependent components are attributed to surface recombination.

Table 5-3: Apparent J_{0m} extracted with different methods after metallisation.

Sample	Blum J_{0m} range (fA/cm^2)	Kimmerle J_{0m} range (fA/cm^2)	Quokka J_{0m} (fA/cm^2)
Heavy-P	287-363	314-388	613
Light-P	241-388	202-355	1987
Light-B	217-731	255-784	1658

Compared to the J_{0s} values, the apparent J_{0m} extracted using Kane-Swanson based techniques show a much stronger injection dependence for all samples (see Fig. 5-1 (d)-(f)). The fitted values span a range of 76 fA/cm^2 for Heavy-P, 147 fA/cm^2 for Light-P and 514 fA/cm^2 for Light-B. This injection dependence is largely caused by the assumption of uniform Δn with sample depth not being fulfilled. These samples have high recombination at the rear metallised surface and low recombination at the front passivated surface. This asymmetrical recombination and the resulting lower effective diffusion length cause a strongly non-symmetrical carrier profile, with Δn at the metallised surface significantly lower than Δn_{av} in the bulk. This effect is exacerbated by using shorter wavelength illumination (as all PL-based techniques do), so most carriers are generated close to the front surface of the sample and must diffuse to the high recombination rear surface. The method of Blum *et al.* assumes symmetrical surfaces and infrared illumination (thus uniform generation), and therefore has severe limitations when used for metallised samples or using short wavelength illumination. As discussed in Section 2.3.1, the method of Kimmerle *et al.* includes a correction for carrier diffusion, but the correction still assumes uniform generation rate and symmetrical surfaces, thus is also inaccurate. These issues must be considered for all PL-based measurements of surface recombination [12], [13]. The importance of uniform Δn profile for analysis of this type is explored further using simulations in Section 5.3.2.

In contrast, the Quokka model fitted the measured data well for measurements both before and after metallisation for all samples (see Fig. 5-1 (a)-(c)). It is noted that for all three samples the values for J_{0m} obtained from the Quokka analysis are substantially higher compared to the data from the Kane-Swanson based analyses (see Table 5-3). Because Quokka simulates the depth profile of Δn and can fit the data well over a large range, the higher values obtained from the Quokka fits are believed to be more accurate. An explanation for this discrepancy between values extracted by the different methods

is shown using simulations in Section 5.3.2 and the quality of the Quokka fit is further evaluated in Section 5.3.3.

The J_{0s} and J_{0m} values obtained from the Quokka fits are also in accordance with expectations given the respective sample preparations. For the unmetallised samples, Heavy-P has higher J_{0s} than Light-P, however, after metallization the trend is reversed with Light-P having higher J_{0m} than Heavy-P. As anticipated, the higher surface doping density formed by the heavy diffusion provides a better passivation of the metallised surface. In contrast, before metallization, Auger recombination in the heavier diffusion dominates J_{0s}. Light-B has higher J_{0s} than Light-P before metallization but after metallization they have a similar J_{0m}. This suggests Light-B has poorer surface passivation initially, but the surface recombination is dominated by the metal-Si interface after metallization for both samples.

5.3.2 QUANTIFYING KANE-SWANSON BASED J_0 EXTRACTION ERRORS

Both the strong asymmetry in surface recombination and the asymmetry in generation caused by using short wavelength illumination contribute to the error in the extracted parameters from the Kane-Swanson based techniques. In this section, further Quokka simulations are performed to demonstrate the relative importance of these factors. A one-dimensional model of a 200 μm thick wafer was used to simulate τ_{eff} as a function of Δn_{av} with $J_{0,front} = 1$ fA/cm^2, constant $\tau_{bulk} = 1$ ms and $J_{0,rear}$ varied between 1, 10, 100 and 1000 fA/cm^2. The generation profile was simulated using Quokka's internal 1D monochromatic illumination model with an illumination wavelength of 550 nm for asymmetrical generation and 1100 nm for uniform generation, respectively. The Kane-Swanson based extraction techniques of Blum *et al.* and Kimmerle *et al.* were applied to the simulated lifetime data in the injection level range 10^{15} cm^{-3} < Δn < 3×10^{16} cm^{-3}. These methods were modified to use the same constant $n_{i,eff}$ as the simulations, rather than the injection dependent models used in the analysis of the measurements in Section 5.3.1 so that a comparison could be made. The extracted $J_{0s,tot}$ values and the sum of the input values for $J_{0,front}$ and $J_{0,rear}$ are shown in Fig. 5-2.

For both illumination wavelengths, the apparent $J_{0s,tot}$ extracted using Kane-Swanson based methods match the modelled values very well for the low $J_{0,rear}$ simulations where the asymmetry of the surface recombination is low. For example, for the simulation of a sample with $J_{0,rear} = 1$ fA/cm^2 we expect $J_{0s,tot} = 2$ fA/cm^2 for the total saturation current density, which is close to the simulated values shown in Fig. 5-2. The small differences for the completely symmetrical sample can be explained by Auger recombination at high injection and slightly different implementations of the Auger model at low injection.

As expected, when $J_{0,rear}$ is increased to 100 and 1000 fA/cm^2, the extracted $J_{0s,tot}$ deviates from the modelled value. For $J_{0,rear}$ = 100 fA/cm^2 (i.e. $J_{0,rear}$ is 100 times higher than $J_{0,front}$), $J_{0s,tot}$ is underestimated by 19 % for 550 nm illumination and 11 % for 1100 nm illumination at Δn = 10^{16} cm^{-3}, representing a significant error in the extracted value. For $J_{0,rear}$ = 1000 fA/cm^2 this underestimation increases to 73 % for 550 nm illumination and 62 % for 1100 nm illumination (at Δn = 10^{16} cm^{-3}). Thus, the deviation is slightly higher for 550 nm than 1100 nm illumination wavelength, but is substantial in both cases, which indicates that the asymmetrical recombination is the dominant factor.
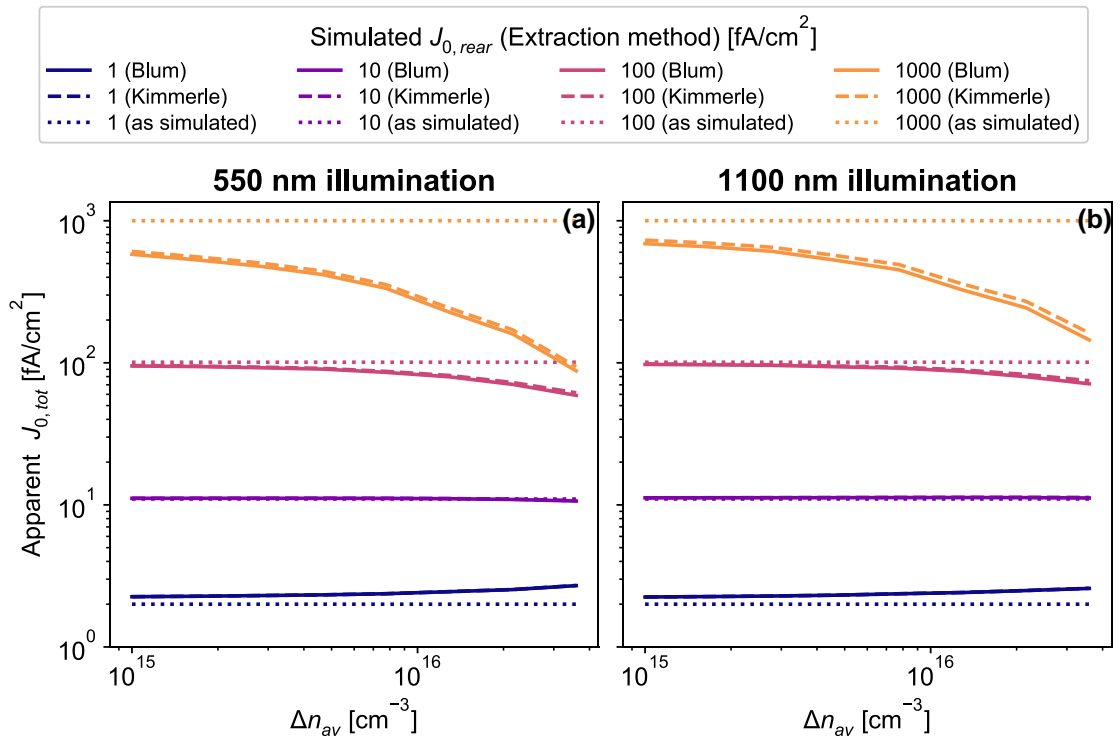
Fig. 5-2: Apparent $J_{0s,tot}$ extracted using the slope-based methods of Blum *et al.* and Kimmerle *et al.* as a function of Δn_{av} for (a) 550 nm illumination and (b) 1100 nm illumination. Horizontal dotted lines indicate the sum of the simulated $J_{0,front}$ and $J_{0,rear}$.

As discussed in Section 5.3.1, this deviation is caused principally by the non-uniform carrier profile. This is shown explicitly in Fig. 5-3, which shows the resultant normalised carrier profiles across the simulated thickness generated in these simulations for the symmetrical case where $J_{0,front}$ = $J_{0,rear}$ = 1 fA/cm^2, and the most extreme asymmetrical case where $J_{0,rear}$ = 1000 fA/cm^2. The carrier profiles are shown at both simulated illumination wavelengths for Δn_{av} = 10^{15} cm^{-3} and Δn_{av} = 10^{16} cm^{-3}.

Strong deviations between Δn at the surface and Δn_{av} are observed in the simulations of asymmetrical surface recombination for both short and long wavelength illumination. The Δn at the rear surface is 29 % lower than Δn_{av} for 550 nm illumination and still 22 % lower for 1100 nm illumination at Δn_{av} = 10^{16} cm^{-3}. It can be seen from the definition in Eq. (2-12)

that at high injection, J_0 is proportional to the inverse square of Δn. Thus, the relatively modest overestimation of Δn at the rear surface results in significant underestimation of the apparent $J_{0,total}$ extracted from the simulated data. These deviations are also found to increase with injection level. This means that the errors introduced by the deviations increase with injection and would thus cause further error in calculating J_{0m} by the slope-based methods, which are commonly applied at high injection. Such a strong deviation in carrier density violates a key assumption of the slope-based analysis techniques, and this is believed to be the origin of the strong injection dependence of the apparent J_{0m} of these samples observed in Fig. 5-1 (d)-(f).

In comparison, the data from the symmetrical simulations showed less than 1 % deviation between Δn at the rear surface and Δn_{av}. These simulations, in which the bulk lifetime is high, the surface recombination is low and symmetric, and the generation is uniform, represent the case where deviations are low. Thus, the assumptions of the slope-based techniques are met, and they work sufficiently well. The short wavelength illumination has practically zero effect in this case because the effective diffusion length is high.

It is also noted that the sample width plays an important role in the presence of the observed errors. A rule of thumb stated in Kane and Swanson's original paper [59], is that the Δn profile becomes non-uniform when the effective surface recombination velocity at the rear surface exceeds the diffusion velocity, defined as D_{amb}/W, where D_{amb} is the ambipolar diffusivity. The samples measured for this study were somewhat thicker than typical silicon cells (280 μm and 710 μm thick) and thus this condition is more readily satisfied. However, the simulations (200 μm thick) show that these effects are still present for samples with more typical thickness.

Overall the data presented above shows that asymmetrical surface recombination is the dominant factor determining whether the Δn profile is uniform. Although the short wavelength illumination required for the PL measurement does contribute to a non-uniform excess carrier profile, it does not significantly affect the range where this assumption is fulfilled for a standard sample thickness. When the assumption is not fulfilled, the data needs to be corrected for non-uniform Δn by, for example, numerical simulations.
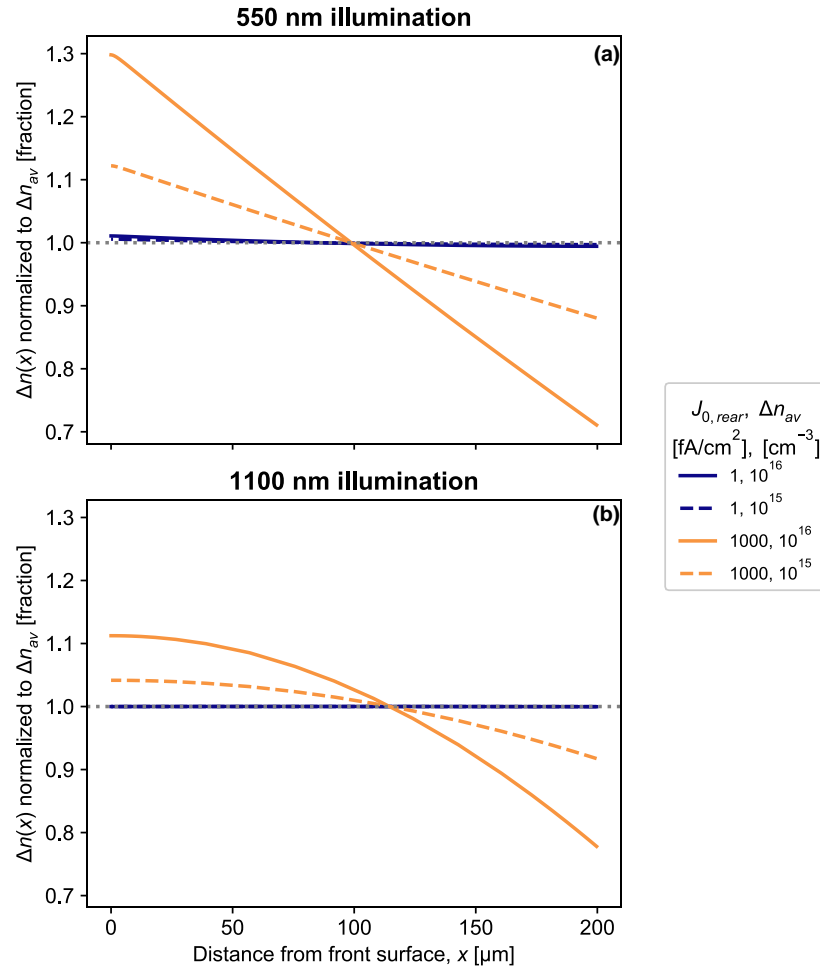
Fig. 5-3: Simulated Δ*n* profiles for symmetrical and asymmetrical surface recombination with illumination (a) 550 nm and (b) 1100 nm, normalised to Δ*n*av. Horizontal dotted grey line indicates Δ*n*av.

5.3.3 CURVE FITTING SENSITIVITY ANALYSIS

The parameter of interest from the Quokka-based fitting procedure described in Section 5.2.3 is J_{0m}, obtained from the second fit to data measured on the samples with one metallised surface. However, the uncertainty of the second fit is dependent on the uncertainty of the two parameters obtained from the first fit, J_{0s} and τ_{const}, performed on the symmetrical non-metallised samples. To assess the uncertainty of the overall procedure and the sensitivity of J_{0m} to the first fit, the following evaluation procedure was followed. First, J_{0s} and τ_{const} were each individually re-fit to the unmetallised data while fixing the respective other parameter to a perturbed value 10 % higher or lower than the initially obtained optimum value from the analysis in Section 5.3.1. Then, J_{0m} was re-fitted to the metallised lifetime data using the obtained re-fitted J_{0s} and τ_{const} values as fixed inputs.

The data obtained from the first part of this analysis for sample Heavy-P are shown in Table 5-4. It is observed that the root-mean-square error (RMSE) of the fit increased for

all the re-fits. This gives high confidence in the initial two-parameter fit. The error increased by a factor of three when J_{0s} was perturbed. However, it only increased by approximately half when τ_{const} was perturbed. The data also show that +10 % perturbation of J_{0s} resulted in approximately +40 % change in τ_{const} (-25 % for perturbation of -10 %), whereas the same perturbation of τ_{const} resulted in only approximately ±3 % change in J_{0s}. This indicates that the fit is significantly more sensitive to J_{0s} than τ_{const}. An important assumption of this fitting method is that the bulk lifetime is assumed to be constant. Some error is introduced if the sample does not fulfil this assumption. However, the demonstrated relative insensitivity of the fit to τ_{const} shows that the model is robust against this error for these samples.

Table 5-4: Individually re-fitted J_{0s} and τ_{const} after ±10 % perturbation for Heavy-P. Fitted value shown in *bold italics*.

J_{0s} (fA/cm^2)	τ_{const} (μs)	RMSE (μs)	Description
84	***1790***	6.6	J_{0s} fixed +10 %, τ_{const} fitted
78	1388	3.1	J_{0s} fitted, τ_{const} fixed +10 %
76	***1262***	2.1	Baseline case: both parameters fitted (Table 5-2)
74	1136	3.4	J_{0s} fitted, τ_{const} fixed -10 %
69	***959***	6.6	J_{0s} fixed -10 %, τ_{const} fitted

The re-fitted J_{0s} and τ_{const} then served as upper and lower bounds of the error in the first fit, which were used as fixed inputs in re-fits of J_{0m} to the lifetime data after metallization. The resulting data are shown in Table 5-5. The maximum change in J_{0m} was observed to be less than ±5 % for all simulated cases. In the simulations where τ_{const} was fixed to a lower value than the baseline case, the RMSE was slightly reduced compared to the initial fit, which indicates that the fit was slightly better. However, these small differences in fit error can be expected given that the fitting ranges of the measurements before and after metallization are slightly different (see Fig. 5-1 (a)-(c)). J_{0m}, the parameter of most interest, is shown to be relatively insensitive to the fixed inputs, which gives high confidence in the data obtained and the usefulness of the method for these samples.

Table 5-5: Change of re-fitted J_{0m} for varied fixed J_{0s} and τ_{const} for Heavy-P. Fitted value shown in *bold italics*.

J_{0s} (fA/cm^2)	τ_{const} (μs)	J_{0m} (fA/cm^2)	Change (%)	RMSE (μs)	Description
74	959	***594***	-3.1	0.8	J_{0s} ↓, τ_{const} ↓
74	1790	***640***	4.3	1.3	J_{0s} ↓, τ_{const} ↑
76	1262	***613***	0.0	1.2	Baseline case
78	959	***586***	-4.4	1.0	J_{0s} ↑, τ_{const} ↓
78	1790	***631***	3.0	1.5	J_{0s} ↑, τ_{const} ↑

5.4 CONCLUSIONS

A QSSPL-based measurement setup was used to measure the injection dependent τ_{eff} of full area metallised Si samples. The wide injection range and high density of data points enables several possible extraction techniques for J_{0s} and J_{0m}. The methods based on the modified Kane-Swanson approach all rely on the assumption of uniform Δn. It was shown that this assumption is invalid for these measurements and indeed generally for metallised samples, because strongly asymmetrical surface recombination causes Δn to vary strongly with depth in the sample. The short wavelength illumination, which is required by most PL-based techniques, enhances this non-uniformity by a small amount, but is not the dominant factor for samples with high surface recombination. An alternative extraction technique based on simulating the Δn profile and fitting the resulting lifetime data overcomes this limitation and results in more accurate parameters.

CHAPTER 6: METAL CONTACT RECOMBINATION – PARTIAL METALLISATION

In the previous chapter, the problem of measuring J_{0m} of full area metal contacts was investigated. Such contacts are commonly used on the rear of a cell, but how does the situation change for partial metal contacts, such as front-side "H" pattern busbar and finger designs or rear-side finger or point contacts? The laterally non-uniform surface recombination introduced by such contacts introduces complexity which must be accounted for in both the sample design and analysis of measurements. Although a wide variety of characterisation methodologies have been used, they address the increased complexity in different ways, and no clear answer to this question has been provided. This chapter aims to answer this question.

This chapter presents a detailed simulation study and assessment of several reported methodologies, and analysis of experimentally measured Suns-PL data using the published methodologies as well as the Quokka based analysis technique presented in Chapter 5. Of the assessed methods, the approach based on varying the metal area fraction (f_{met}) and using Suns-PL measurements is shown to be the most accurate, while methods based on Suns-V_{oc} measurements or Kane-Swanson analysis are shown to be less accurate. The experimental data appear to support the conclusions of the simulation study but further experimental improvements are required to compare accuracy against the Quokka based curve-fitting approach of Chapter 5 or other full device modelling approaches [12], [13].

6.1 INTRODUCTION

Practically all solar cells require some form of partial metallisation. This can take the form of a partial front side contact, so that sunlight may enter the absorber [32]; a rear side contact in the case of a bifacial and/or PERC cell design [5]; all rear contacted devices need two partial metal contacts to contact the different polarity regions of the device [100]. It follows that accurate and reliable measurement of J_{0m} for such contacts is important and useful.

Analysis of partial metal contacts is more complicated than the one-dimensional analysis of full area contacts discussed in Chapter 5. Partial contacts typically introduce lateral non-uniformity in the surface recombination, which can affect the validity of the assumptions of many traditional surface recombination measurement approaches [59]. The effect of laterally non-uniform surface recombination on Suns-V_{oc} and Suns-PL

measurements was explored in detail in Chapter 4 above, with reference to their applicability to surface recombination measurements in general. In this chapter, that work is put into the specific context of metal surface recombination measurements.

In the review of the literature on metal surface recombination in Section 2.3, three categories of measurement approaches were discussed: analytical approaches, approaches based on varying f_{met}, and full device model based approaches. The analytical approaches appear to rely on several unrealistic assumptions. Full device model approaches are complex and time consuming. The f_{met}-varying methods are interesting because they are simpler and use the partial contact property as an advantage. However, the application of these techniques varies widely in terms of the characterisation technique used, sample design, and type of sample. Given the previously discussed complexity of the laterally non-uniform surface recombination it is unknown how the different choices affect the accuracy of the approach.

Therefore, this chapter comprises a detailed simulation based study of this parameter space to answer this question. A common set of measurements from a cell and a test structure are simulated and analysed using the different f_{met} based methods to understand and compare their accuracy. Measurements of a typical f_{met}-varying test structure are also made using Suns-PL and analysed using the f_{met} based methods as well as the Quokka curve fitting method introduced in Chapter 5, for comparison to the simulated cases.

6.2 MODELLING

The review of recent literature in Section 2.3 showed that there are several published techniques to obtain J_{0m} but there are significant differences between sample design, characterisation technique and extraction method across the literature. In this section, particular attention is paid to the class of techniques which rely on varying f_{met} to extract J_{0m}. Several of these methods are applied to a simulated data set that was generated with a common set of parameters in Quokka version 2 [74]. The resulting extracted J_{0m} values are compared between the methods for accuracy and explanations for the observed differences are given.

6.2.1 MODELLING METHODOLOGY

As discussed in Section 2.3.3, many J_{0m} extraction methods rely on a sample design where multiple samples of the same design are created with varying metal contact fraction. To demonstrate the limitations of these methods two sets of simulations were performed. First, a two-dimensional cell structure was created based on a standard

screen printed cell design. The simulation parameters and model design are shown in Fig. 6-1. This structure was simulated using Quokka's Suns-V_{oc} functionality, which simulates the cell under varied illumination levels with open circuit terminals. Quokka's internal monochromatic illumination model was used with illumination wavelength 808 nm. V_{oc}, Δn_{av}, and τ_{eff} are output at each illumination level. A series of simulations of this cell structure were performed with f_{met} varied between 0.005-0.25 by both changing the finger width and the finger pitch. For finger width varied simulations, the unit cell width was fixed to 850 μm and the front contact width varied between 4.25, 8.5, 42.5, 85, 127.5, 170 and 212.5 μm. For the pitch varied simulations, the front contact width was fixed to 42.5 μm and the contact pitch was varied by changing the width of the solution domain (see p_{con} in Fig. 6-1) between 170, 213.5, 283, 425, 850, 4250, 8500 μm. Note that the $f_{met} = 0.05$ case is identically simulated in both the width varied and pitch varied simulations. Three methods to extract J_{0m} from these simulations are compared:

- The V_{oc} method of Fellmeth *et al.* [72],
- The iV_{oc} method of Comparotto *et al.* [11], and
- A newly introduced method based on the modified Kane-Swanson method [101].**
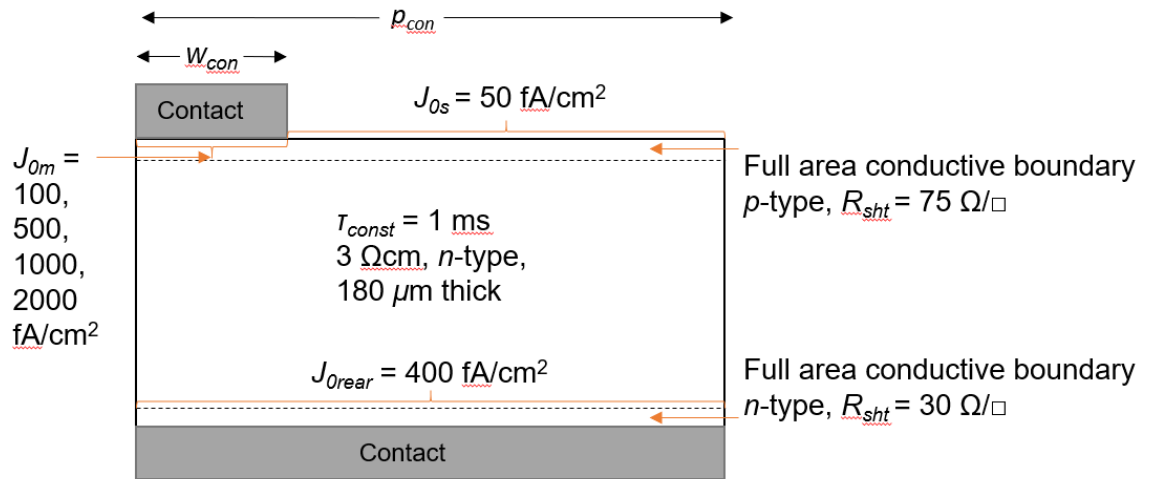
Fig. 6-1: Schematic diagram of two-dimensional cell structure and parameters simulated in Quokka 2.

All three methods follow a similar pattern where first a measurement of total recombination is made for each test sample. It is reasoned that the only source of recombination that varies between samples is the recombination at the metal contact (due to its changing area fraction) and thus a fit of total recombination against f_{met} yields

---

** Note: The method was first introduced by the present author in the cited publication, however the analysis and experimental data in this chapter are new in this thesis.

J_{0m}. For the V_{oc} method, the metric for total recombination is assumed to be J_{01}, extracted from Suns-V_{oc} data at one sun illumination intensity, assuming unity ideality factor such that the one diode model (see Eq. (2-30)) can be applied. Since f_{met} changes for each sample, the shading fraction and thus the generation rate at one sun illumination intensity changes as well. In the simulations, J_{01} was extracted at a constant generation rate of 38 mA/cm². Note that this assumption was not consistently applied in previous studies but can influence the results. The model applied to this data is

$$J_{01} = J_{0,bulk} + J_{0,rear} + f_{met}J_{0m} + [1 - f_{met}]J_{0s} \qquad (6\text{-}1)$$

where $J_{0,bulk}$ and $J_{0,rear}$ are constant for all samples and thus a linear fit of J_{01} against f_{met} yields J_{0m} from the slope when J_{0s} is independently known from a separate measurement.

The iV_{oc} method is identical to the V_{oc} method, except J_{01} is obtained from Suns-PL data instead of Suns-V_{oc} data. For these simulations, iV_{oc} was obtained by applying Eq. (2-9) using Δn_{av}, N_{dop}, and constant $n_{i,eff}$ output by Quokka. Similar to the simulations in Chapter 4, this simulates an area averaged iV_{oc} measurement like that which is obtained from a QSSPL measurement.

The modified Kane-Swanson approach is similar to the voltage based approaches, but takes $J_{0s,tot}$ as the metric representing total recombination. In the simulations, $J_{0s,tot}$ was extracted from the injection dependent τ_{eff} data as described in Section 2.3.1 using the method of Blum *et al.* [61], at the injection level that is equivalent to the constant generation rate used to extract J_{01} for the other voltage-based methods. Since $J_{0s,tot}$ refers to the total surface recombination, the following model applies

$$J_{0s,tot} = J_{0,rear} + [1 - f_{met}]J_{0s} + f_{met}J_{0m} \qquad (6\text{-}2)$$

where the parts pertaining to the metallised surface are the same as in Eq. (6-1) but the constant $J_{0,bulk}$ term is missing.

Note that the implicit assumption for all three methods of the analysis is that the bulk and passivated surface recombination are constant across all samples and thus the only variable between regions with different metal fraction is f_{met} and thus the recombination at that interface.

The second simulated structure was based on a type of test structure reported by several authors [11], [13], [102]. As shown in Fig. 6-2, it consists of a symmetrically diffused and passivated wafer with metal contacts applied on one side of the wafer with varied f_{met}. Since this structure is usually measured using PL, it is referred to as the PL test structure

throughout this chapter. It is noted that because Quokka requires opposite polarity contact types for the front and rear surfaces, the simulated structure contained a *p*-type conductive boundary at the metallised rear surface, an *n*-type bulk and an *n*-type conductive boundary at the front surface instead of *p*-type as would be the case in a real symmetrically diffused *n*-type wafer with boron diffusions. This means that the effects of the lateral R_{sht} discussed below are expected to be even more significant on real devices than the simulated data.
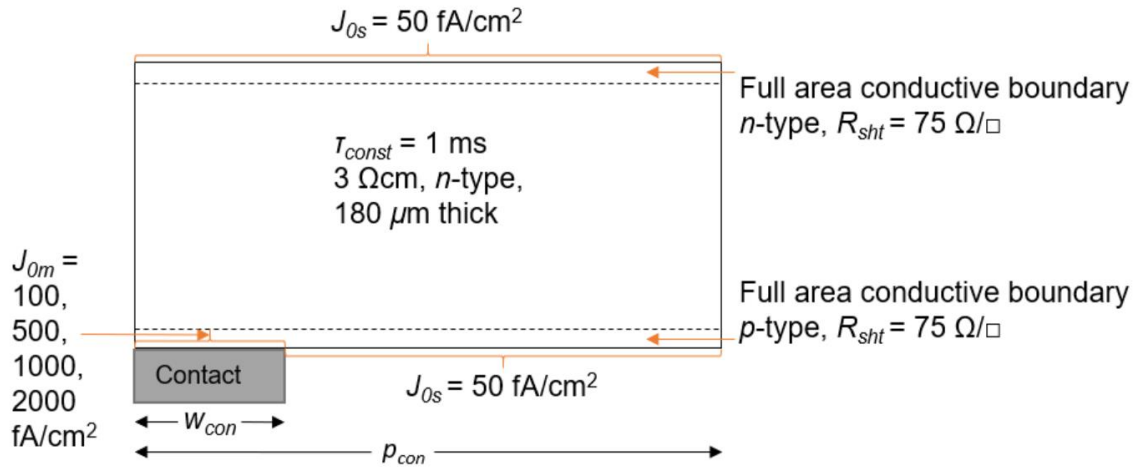
Fig. 6-2: Schematic diagram of two dimensional PL test structure and parameters used in Quokka simulations.

As with the cell simulations, the PL test structure was simulated with varied contact width and contact pitch using the Suns-V_{oc} feature of Quokka. The illumination was identical to the cell simulations. The dimensions of the contact width and pitch variation were also identical to the cell simulations, except that the contact was on the rear side. For the PL test structure, though, only the iV_{oc} method and modified Kane-Swanson method were applied since a contacted V_{oc} measurement of this structure would not be possible. It is noted that because the contact is on the rear of the PL test structure there is no shading issue for these simulations. Therefore, J_{01} and $J_{0s,tot}$ were extracted at one sun generation current (38 mA/cm²) for all simulations, which is the same generation current as the cell simulations. J_{0m} was then extracted from the J_{01} and $J_{0s,tot}$ data using Equations (6-1) and (6-2) for the iV_{oc} and modified Kane-Swanson methods respectively.

6.2.2 MODELLING RESULTS AND DISCUSSION

6.2.2.1 CELL SIMULATIONS

The cell structure in Fig. 6-1 was simulated with J_{0m} at the front contact varied between 100, 500, 1000 and 2000 fA/cm² and f_{met} changed by varying the contact width or pitch. The apparent J_{0m} extracted from each simulation using the V_{oc}, iV_{oc}, and modified Kane-Swanson methods are listed in Table 6-1. The relative errors are shown in Fig. 6-3.

Table 6-1: Apparent J_{0m} extracted using the V_{oc}, iV_{oc}, and modified Kane-Swanson methods from cell simulations.

Simulated J_{0m} [fA/cm^2]	Width			Pitch		
	V_{oc}	iV_{oc}	Mod. K-S	V_{oc}	iV_{oc}	Mod. K-S
100	178	108	102	44	119	113
500	638	519	447	428	566	559
1000	1179	998	786	897	1107	1085
2000	2201	1888	1276	1826	2165	2065
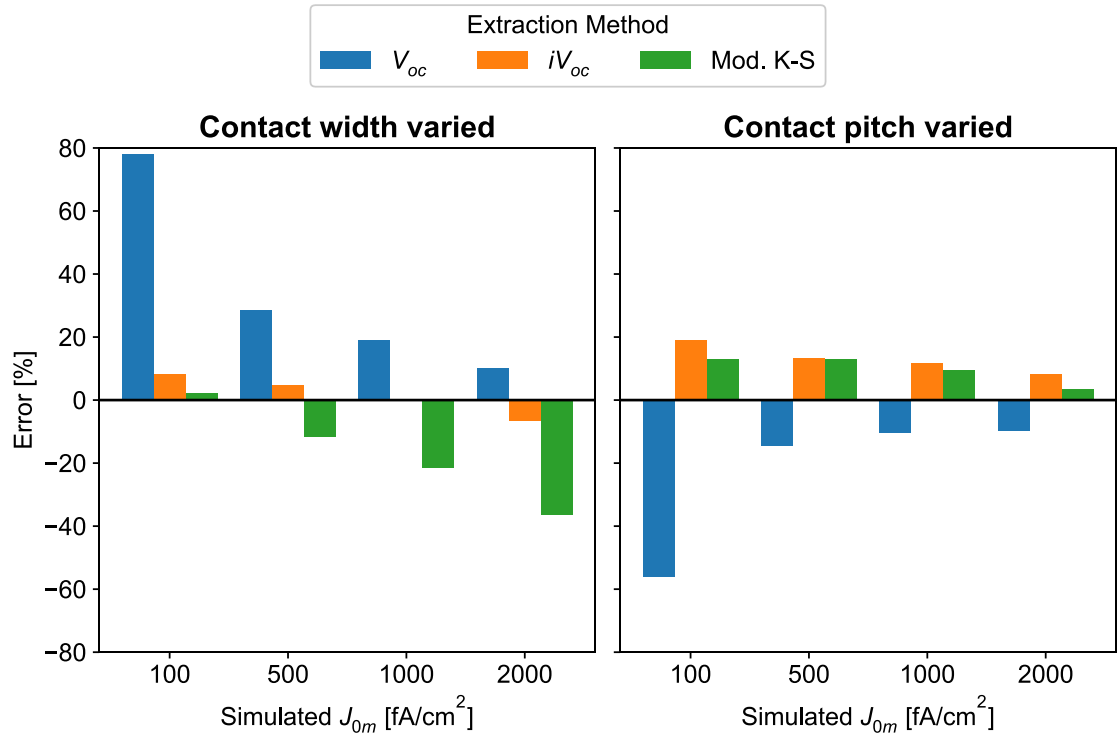
Fig. 6-3: Fractional error of extracted J_{0m} compared to simulated J_{0m} extracted using V_{oc}, iV_{oc} and modified Kane-Swanson methods applied to cell simulations with the contact width varied (left) and with the contact pitch varied (right).

Fig. 6-3 shows that none of the extraction methods perfectly extract the simulated J_{0m}. For simulations where f_{met} was varied by changing the contact width: the V_{oc} method of extraction overestimated the simulated J_{0m}; the iV_{oc} method overestimated the simulated J_{0m} for J_{0m} = 100 fA/cm^2 and 500 fA/cm^2 and underestimated for J_{0m} = 1000 fA/cm^2 and 2000 fA/cm^2, though the error was less than 10 % for all simulations; while the modified Kane-Swanson method underestimated significantly for all simulations except J_{0m} = 100 fA/cm^2, which was slightly overestimated. For simulations where f_{met} was varied by changing the contact pitch the trend was reversed. The V_{oc} method resulted in underestimation of the simulated J_{0m}, while both the iV_{oc} method and modified Kane-Swanson method resulted in overestimation of the simulated J_{0m}.
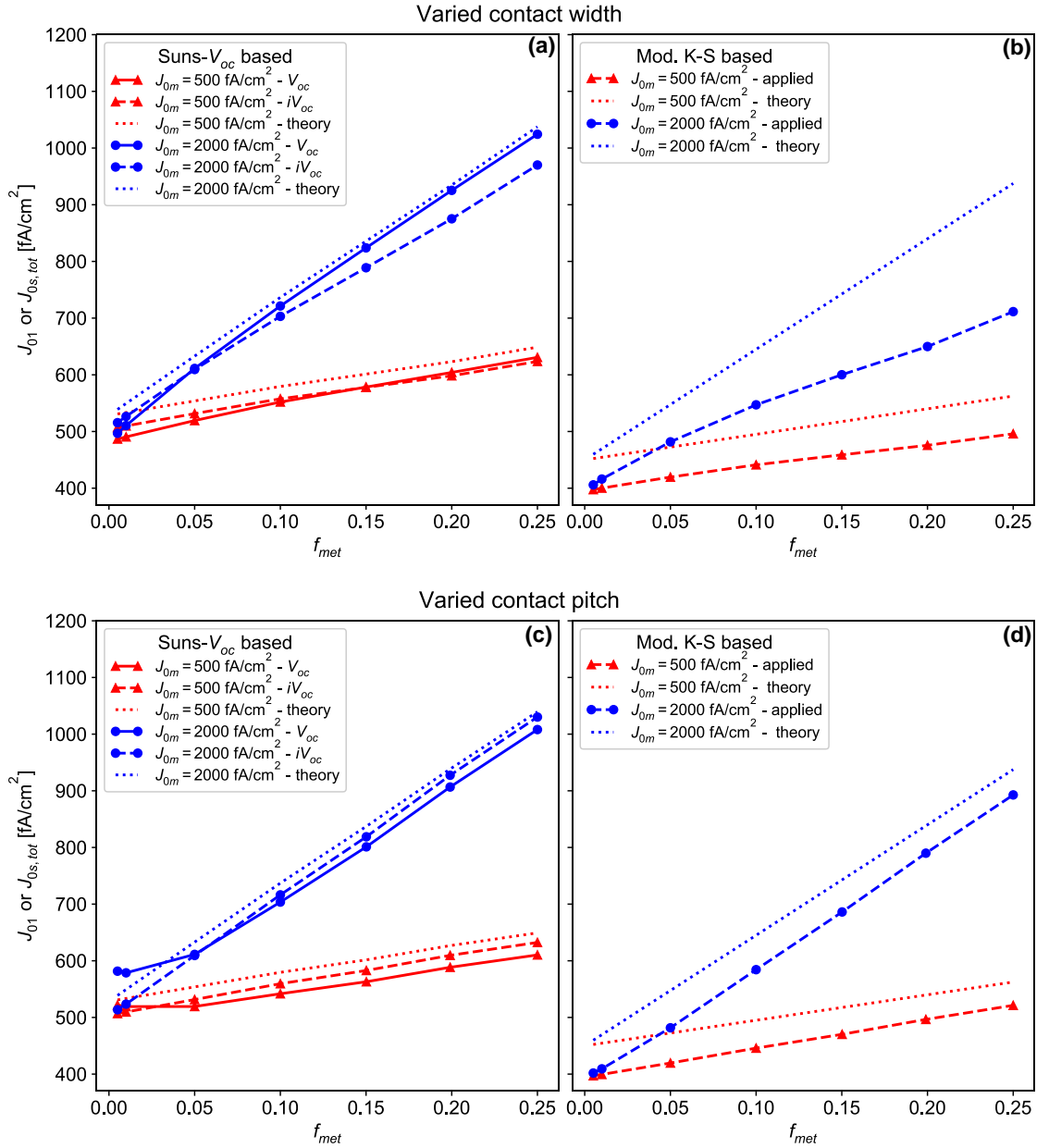
Fig. 6-4: Extracted J_{01} and $J_{0s,tot}$ from various methods plotted against f_{met} varied by changing the contact width or pitch for cell structures. Specifically, (a) J_{01} from voltage based analysis with contact width varied; (b) $J_{0s,tot}$ from K-S based analysis with contact width varied; (c) J_{01} from voltage based analysis with contact pitch varied; (d) $J_{0s,tot}$ from K-S based analysis with contact pitch varied. Theoretical lines calculated from Eq. (6-1) for (a) and (c) and Eq. (6-2) for (b) and (d). Connecting lines are a guide for the eye.

The presented inaccuracies in the extraction methods are best explained with reference to the plots of J_{01} against f_{met} and $J_{0s,tot}$ against f_{met} that were used for the extractions. These are shown for the cases of $J_{0m} = 500$ and 2000 fA/cm² in Fig. 6-4, where the other cases are omitted for clarity. Also included in these plots is the "theoretical" data, which was created by substituting the known simulation parameters into Eq. (6-1) for the voltage based methods and Eq. (6-2) for the modified Kane-Swanson method. It is noted that because Eq. (6-2) does not include a $J_{0,bulk}$ term, the absolute values of the modified

Kane-Swanson theoretical data are lower than the theoretical data of the voltage based methods, however the slopes are the same.

The V_{oc} data shows strong non-linearity for both width-varied and pitch-varied simulations, however, the shape of the non-linearity differs for the different cases. Noting that according to Eq. (6-1), the extraction will be accurate if the slope of the data matches the slope of the theoretical line, for the width-varied simulations the V_{oc} data show curvature across the range of simulated f_{met} with a slope that is higher than that of the theoretical line. However, for the pitch-varied simulations the slope of the V_{oc} data is lower than the theoretical line for $f_{met} \leq 0.1$ and approximately parallel for $f_{met} > 0.1$.

On the other hand, the iV_{oc} and modified Kane-Swanson data appears to be linear across the full f_{met} range for both width and pitch varied simulations, with the slope of the data differing from the theoretical line as would be expected given the errors shown in Fig. 6-3.

Interestingly, the data from all three methods deviate from the theoretical J_0 at $f_{met} = 0.005$. These simulations, where f_{met} is close to zero, are closest to the one-dimensional case discussed in Chapter 5. This indicates an overall offset of the extracted J_0 data from all methods across the full range of f_{met}. The cause of this offset is the same as the errors discussed in Section 5.3.2. The high $J_{0,rear}$ of the simulated cell and short wavelength illumination act to cause non-uniformity of Δn with depth. The discussion in Chapter 5 established that this causes an underestimation error in the calculation of $J_{0s,tot}$ from the modified Kane-Swanson method (see Fig. 5-2) and this same offset is observed in Fig. 6-4 (b) and (d). This non-uniformity also causes an underestimation error in the V_{oc} and iV_{oc} methods.

In addition to the offset discussed above, there is a non-linearity to the V_{oc} data that is readily explained by the influence of the lateral series resistance in the front conductive layer. Following the discussion in Chapter 4, we know that V_{oc} measurements are by their nature local and that V_{oc} only represents the average recombination behaviour of a device when carriers that are generated away from the contacts can easily be transported to the contacts. Therefore, R_{sht} has a strong modulating effect on the V_{oc}. This explains the V_{oc} data in Fig. 6-4 (c). For the pitch-varied data, the contact size remains the same in each simulation, but the distance between contacts changes. For $f_{met} \geq 0.1$ the contacts are closer than a typical cell so the effective R_{sht} is small and the loss is negligible. Thus, the V_{oc} data appear parallel to the theoretical line. However, for lower f_{met}, the contacts are much further apart than a typical cell, resulting in a very high

effective R_{sht}. For example, $f_{met} = 0.01$ has five times the pitch and thus five times the effective R_{sht}. The higher R_{sht} results in a higher resistive loss, causing a lower voltage at the contact and thus artificially high J_{01}, as observed in the data.

The influence of R_{sht} is also the cause of the non-linear V_{oc} data for the simulations with contact width variation. For these simulations the length of the lateral transport does not vary as much, but the size of the contact varies significantly across the range of f_{met}. This means that as f_{met} increases, the area of contact recombination must be serviced by a smaller non-contacted region. To maintain constant average generation rate in the structure across each value of f_{met} for the extraction of J_{01} the illumination intensity is increased. This also increases the local current density in the front conductive layer, which increases the resistive loss through a current crowding effect. The larger the contact the greater the lateral current flow required and thus the greater the voltage loss.
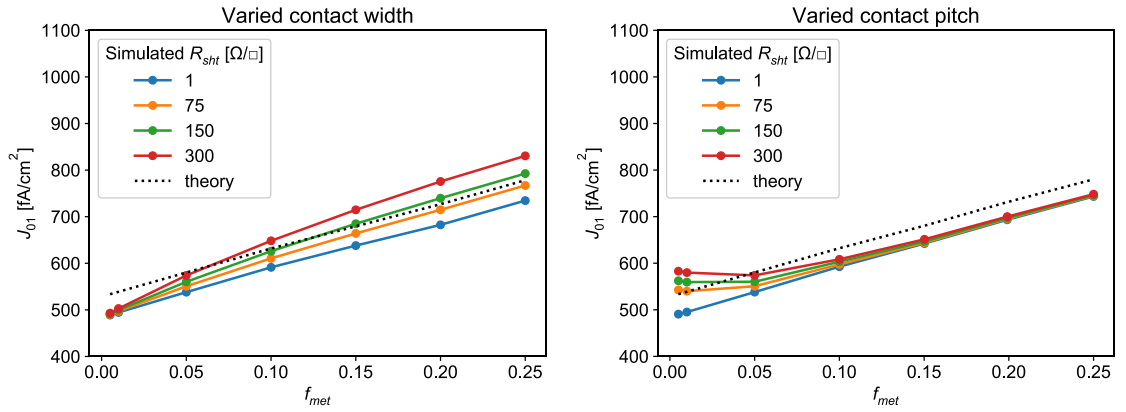
Fig. 6-5: Extracted J_{01} from Suns-V_{oc} measurements as a function of f_{met} for varied front R_{sht} and fixed $J_{0m} = 1000$ fA/cm^2 with contact width varied (left) and contact pitch varied (right).

To illustrate these non-linearities in the V_{oc} data, a second set of simulations was performed using identical parameters to the first set, but with J_{0m} fixed to 1000 fA/cm^2 and R_{sht} varied between 1 Ω/□, 75 Ω/□, 150 Ω/□ and 300 Ω/□. Only the V_{oc} method was applied to these simulations with the resulting plots of J_{01} against f_{met} shown in Fig. 6-5 for the width-varied and pitch-varied cases. Both figures indicate that the degree of curvature is increasing for increased R_{sht}. In both cases when $R_{sht} = 1$ Ω/□ (the lowest available R_{sht} in Quokka version 2) the data appear linear and the line is parallel to the theoretical data. The remaining offset is explained by the one dimensional underestimation of J_{01} caused by the high rear recombination as discussed above. This demonstrates that when the lateral conductivity is high, excess carriers can easily diffuse to anywhere in the device and thus the voltage at the contact is equal to the implied voltage elsewhere in the device and reflects the average amount of recombination

occurring across the device. It also shows that higher R_{sht} is the cause of the non-linear V_{oc} data.

The remaining errors in the J_{0m} extracted from the iV_{oc} and modified Kane-Swanson methods are similar to the errors found in the analysis of the PL test structures in the following section.
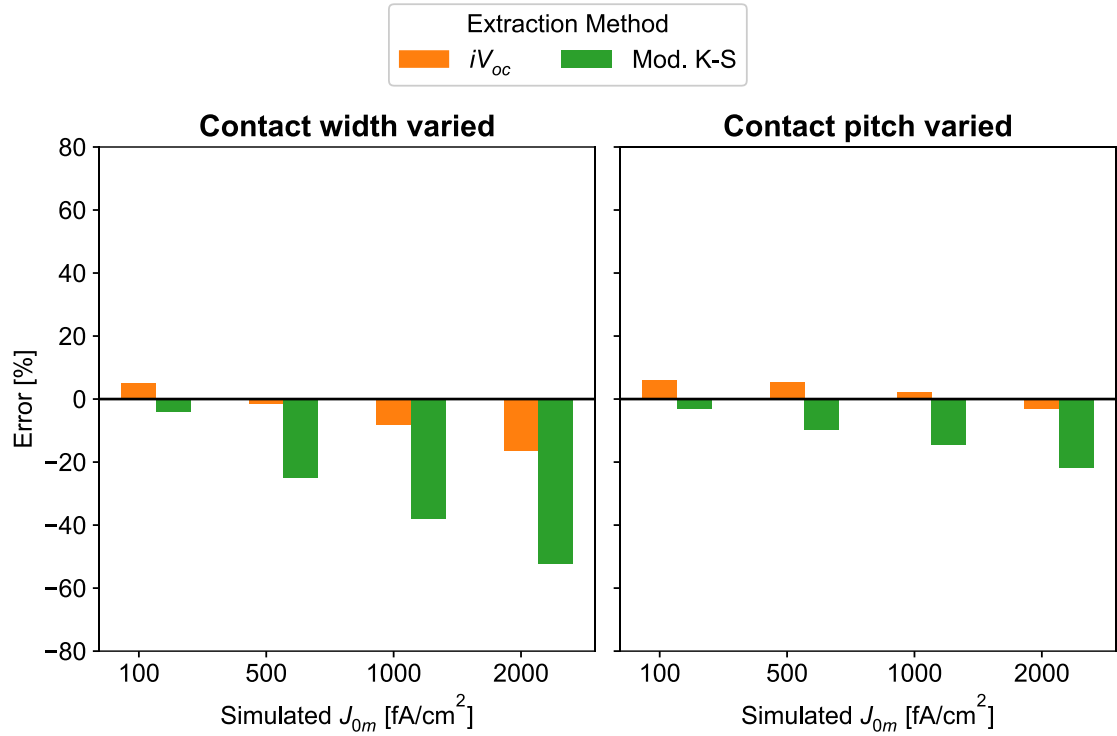
6.2.2.2 PL TEST STRUCTURE SIMULATIONS

PL test structures were simulated similarly to the cell structures with J_{0m} at the front contact varied between 100, 500, 1000 and 2000 fA/cm^2 and f_{met} changed by varying the contact width or pitch. The PL test structures had identical bulk and front surface properties to the cells, but on the opposite side to the partial metal contact it had a passivated and diffused surface that was identical to the passivated part of the front surface. The structure was also simulated with the metal contact on the rear side relative to the illumination source, as would be the case for a PL measurement. A contacted V_{oc} measurement of this structure is not possible, thus only the iV_{oc} and modified Kane-Swanson methods were applied to the simulated data. The extracted J_{0m} data are shown in Table 6-2. The relative errors in the extracted data by comparison to the simulated J_{0m} are shown in Fig. 6-6.

Overall, the errors for the modified Kane-Swanson method are larger than for the iV_{oc} method. For the iV_{oc} method, the deviation of the extracted J_{0m} is less than 10 % for both width and pitch varied simulations in all cases, except for J_{0m} = 2000 fA/cm^2 in the width varied case. On the other hand, the modified Kane-Swanson method underestimates J_{0m} for all simulated cases. The underestimation is more severe for the contact width varied simulations, where the error exceeds 50 % for the J_{0m} = 2000 fA/cm^2 case. In the contact pitch varied simulations, the underestimation error for the same J_{0m} is approximately 20 %.

Table 6-2: Apparent J_{0m} extracted using the iV_{oc}, and modified Kane-Swanson methods from PL test structure simulations.

| Simulated J_{0m} [fA/cm^2]	Width		Pitch	
	iV_{oc}	Mod. K-S	iV_{oc}	Mod. K-S
100	105	96	106	97
500	493	376	526	451
1000	919	622	1020	854
2000	1674	958	1941	1569

Fig. 6-6: Fractional error of extracted J_{0m} compared to simulated J_{0m} extracted using iV_{oc} and modified Kane-Swanson methods applied to PL test structure simulations.

These errors are best explained with reference to the plots that were used to extract J_{0m}, which are shown in Fig. 6-7 for $J_{0m} = 500$ fA/cm^2 and 2000 fA/cm^2 (the other data excluded for clarity) with theoretical data also shown where Equations (6-1) and (6-2) were applied using the simulated parameters only. Unlike the cell simulations, there is no offset between the simulated and extracted data at $f_{met} = 0.005$ for any of the methods. This is because the non-metallised side has a relatively well-passivated surface with $J_{0s} = 50$ fA/cm^2 compared to the metallised rear of the cell that was simulated with $J_{0,rear} = 400$ fA/cm^2. The overall recombination in the structure is lower and thus the carrier profile is flatter so minimal error is expected. The simulations for $f_{met} = 0.005$ are very similar to the one-dimensional case discussed in Chapter 5. As shown in Fig. 5-2, the Kane-Swanson method is most accurate when both surfaces have low recombination.

Unlike the V_{oc} method, the iV_{oc} and modified Kane-Swanson methods are just two different ways of interpreting the same measurement, an area-averaged illumination intensity dependent PL measurement. Thus, the different degree of error in the J_{0m} extracted using each method can be explained by the different underlying assumptions. As discussed in Section 5.3.2, the Kane-Swanson approach explicitly requires Δn at the surface of interest to be equal to Δn_{av}, which is the measured quantity. Importantly, this is a requirement for each individual sample. It is observed that for low f_{met} both surfaces
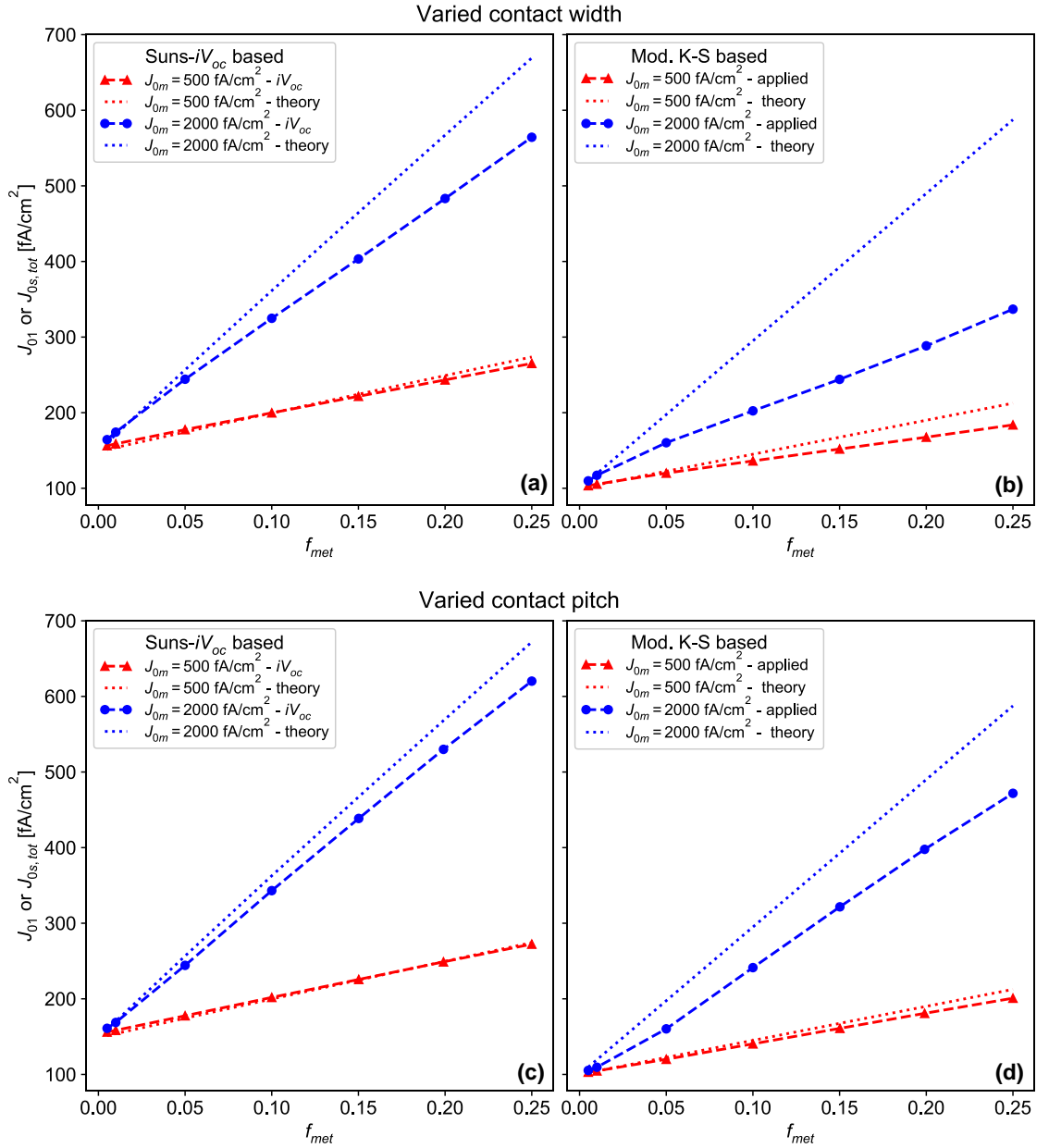
Fig. 6-7: Extracted J_{01} and $J_{0s,tot}$ from iV_{oc} and Blum methods plotted against f_{met} for passivated test structures. In (a) J_{01} from iV_{oc} based analysis with contact width varied; (b) $J_{0s,tot}$ from K-S based analysis with contact width varied; (c) J_{01} from iV_{oc} based analysis with contact pitch varied; (d) $J_{0s,tot}$ from K-S based analysis with contact pitch varied. Theoretical lines calculated from Eq. (6-1) for (a) and (c) and Eq. (6-2) for (b) and (d). Connecting lines are a guide for the eye.

of the PL test structure have low surface recombination and as f_{met} increases, the surface recombination gets progressively worse on the metallised surface, which increases the deviation of Δn at the surface from Δn_{av} and thus increases the underestimation of $J_{0s,tot}$. Therefore, the theoretical and extracted $J_{0s,tot}$ data converge for low f_{met} and diverge as f_{met} increases.

The iV_{oc} method on the other hand makes no assumptions about Δn_{av} at the surface. The method only requires that the change in recombination current as f_{met} increases has

unity ideality. From Eq. (6-1) it is observed that this is the same as requiring that the recombination at the metal interface and the passivated surface on the metallised side has unity ideality. However, some divergence of the extracted J_{01} data from the theoretical data is still observed for the J_{0m} = 1000 fA/cm^2 and 2000 fA/cm^2 cases with increasing f_{met}, albeit to a lesser degree than the modified Kane-Swanson data. The degree of divergence, and therefore the underestimation of J_{0m}, is greater for the contact width varied simulations than the contact pitch varied simulations. This is caused by a lateral resistance effect as discussed below.

The degree of underestimation of J_{01} and $J_{0s,tot}$ in these simulations is modulated by R_{sht}. The simulations for J_{0m} = 1000 fA/cm^2 were repeated with front and rear R_{sht} = 1 Ω/□ and R_{sht} = 10,000 Ω/□. The latter very high value was chosen to simulate a sample without a full area diffusion (e.g. laser doped point contacts [103]) and the former to "turn off" the effect of the lateral resistance. The resulting data are shown in Fig. 6-8 for both extraction methods and for both contact width varied and contact pitch varied simulations. R_{sht} has a stronger effect on the width varied data than the pitch varied data.

For the iV_{oc} method, when R_{sht} = 1 Ω/□, the data nearly match the theoretical data. This is because the low sheet resistance easily allows excess carriers to flow laterally and equalise the voltage in the entire structure. Therefore, the average iV_{oc} is reflective of the recombination in the whole device. The opposite is true for the R_{sht} = 10,000 Ω/□ simulations. In this case the high recombination contact region is isolated from the rest of the structure.

These effects are much more significant for the width varied than the pitch varied case. In the width varied case, the increasing contact size necessitates an increasing absolute recombination current into the contact through the conductive boundary and thus, a higher resistive loss for increased f_{met}. For the pitch varied case though, the absolute recombination current into the contact is the same for each simulation so there is less resistive loss.

The modified Kane-Swanson extracted data follow similar trends to those discussed for the iV_{oc} method, except that the R_{sht} = 1 Ω/□ data are still significantly divergent from the theoretical data. This is caused by the remaining one-dimensional effect of non-uniform Δn as discussed above.
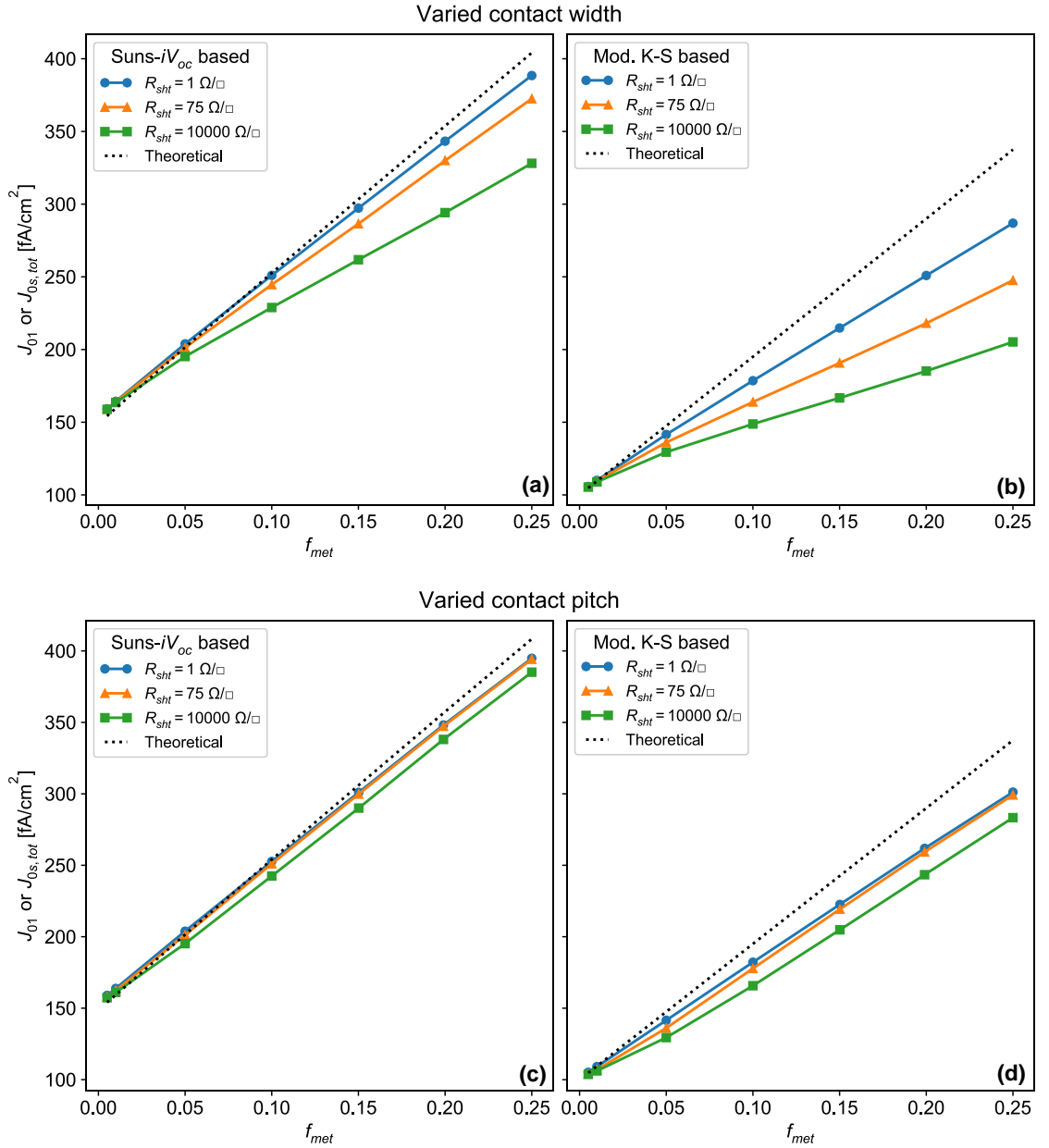
Fig. 6-8: J_{01} or $J_{0s,tot}$ **plotted against** f_{met} **for varied conductive boundary** R_{sht} **and fixed** J_{0m} = 1000 fA/cm². **Theoretical lines calculated from Eq. (6-1) for (a) and (c) and Eq. (6-2) for (b) and (d). Connecting lines are a guide for the eye.**

Both methods of J_{0m} extraction can be arbitrarily performed at any point on the Suns-PL curve, or equivalently the injection dependent τ_{eff} curve. The voltage based methods are usually performed at one sun illumination intensity as stated in the literature [72], but this choice is somewhat arbitrary. Arguably, 0.1 suns illumination intensity is closer to the maximum power point of an operating cell and in any case, the extra recombination that occurs in a cell structure compared to the PL test structure means that even the one sun excess carrier density of a completed device under operation will be considerably lower than the one sun operating conditions of the test structure. To better understand the injection level dependence of each extraction method, the methods were applied across

the full range of illumination intensities from 10^{-2} - 10^3 suns for both the width varied and pitch varied cases. The resulting extracted J_{0m} data are shown as a function of illumination intensity for the same four simulated values of J_{0m} in Fig. 6-9 and Fig 6-10. The simulated J_{0m} data are shown as horizontal dotted lines in the figures.
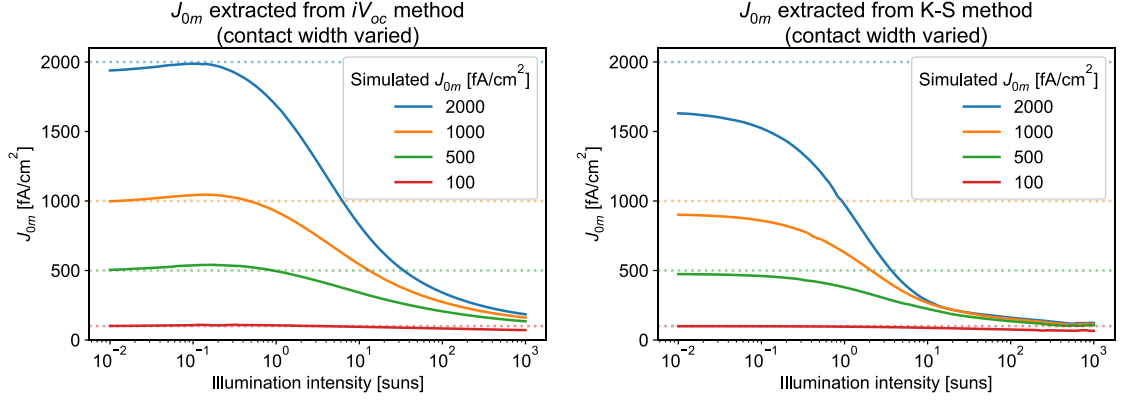
Fig. 6-9: Illumination intensity dependence of apparent J_{0m} extracted by the (left) iV_{oc} and (right) modified Kane-Swanson methods, for simulations with varied contact width. Dotted lines indicate the simulated values.
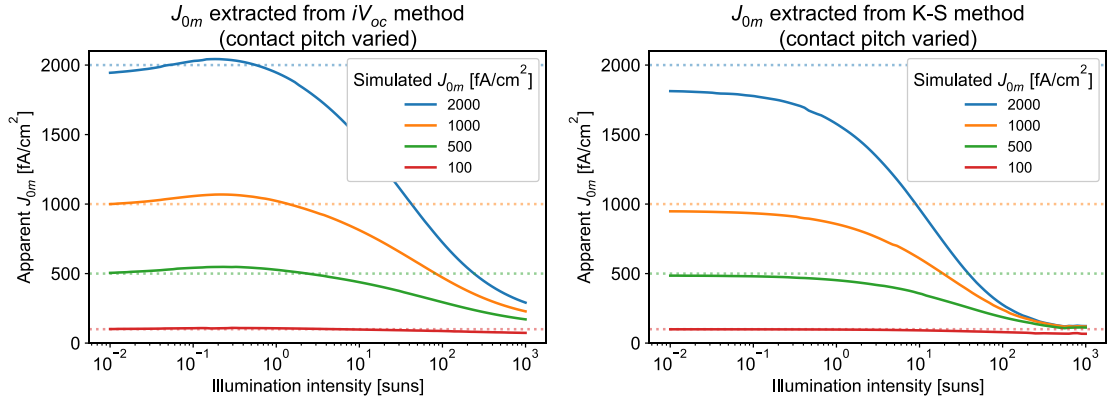
Fig. 6-10: Illumination intensity dependence of apparent J_{0m} extracted by the (left) iV_{oc} and (right) modified Kane-Swanson methods, for simulations with varied contact pitch. Dotted lines indicate the simulated values.

It is first observed that both methods fail severely at illumination intensities above one sun. The higher currents at these illumination intensities exacerbate the R_{sht} losses discussed above and thus it would not be sensible to extract the value at these points, though it might be tempting to if the traditional instruction to perform the Kane-Swanson extraction at $\Delta n = 10 N_{dop}$ is followed.

Below one sun, the iV_{oc} method appears to approximate the simulated J_{0m} value quite well, even for the very high J_{0m} = 2000 fA/cm^2 simulations. The pitch based simulations extract J_{0m} well for illumination intensities of one sun and below, while the more accurate width based extractions occur from approximately 0.1 suns and lower.

The modified Kane-Swanson method overall underestimates J_{0m} more severely than iV_{oc}. For moderate J_{0m} up to 500 fA/cm^2, extraction error is minimal for illumination intensities 0.1 suns and lower. However, for any higher J_{0m} value or illumination intensity higher than 0.1 suns the underestimation error is quite severe. The underestimation is worse for the width varied compared to the pitch varied simulations, which is the same pattern as the iV_{oc} method extractions.

It is also noted that these simulations did not include an injection dependent bulk lifetime, and this would likely affect the accuracy of both extraction methods at lower illumination intensities.

6.2.3 MODELLING CONCLUSIONS

The simulations in this section have explored three different methods of J_{0m} extraction that rely on variation of f_{met}. The factors considered were the magnitude of J_{0m}, the influence of R_{sht}, whether the sample is a cell or passivated test structure, whether f_{met} was varied by changing the pitch or width of the metallisation. The simulations have shown that there are several potential problems with the accuracy of these techniques.

The iV_{oc} method applied to the PL test structure, with pitch varied f_{met} is the most accurate. It contains the least assumptions in the model and by using pitch variation minimises the effect of R_{sht} changing as f_{met} increases.

The modified Kane-Swanson method is less accurate overall, particularly for higher J_{0m}. This owing to the more complex assumptions in the method, particularly that Δn at the surface must be equal to Δn_{av}.

The V_{oc} method is inaccurate for the cell simulations because of the inherently local nature of V_{oc} measurements and the influence of R_{sht}. The inaccuracy is worst for low f_{met}, so the error could potentially be somewhat mitigated by using $f_{met} \geq 0.1$. iV_{oc} is preferable across all simulations because it is area-averaged.

The extracted data from simulations with pitch varied f_{met} are more accurate than from width varied data across all the methods and structures. Width varied structures increase the local recombination current and thus increase the R_{sht} loss as a function or f_{met}, which causes the inaccuracy.

Finally, by applying each extraction method at a range of illumination intensities it was shown that the extractions are potentially more accurate at approximately 0.1 suns rather than 1 sun because there is less influence of R_{sht} when the current is lower. More

investigation is needed though because, for example, these simulations did not include an injection dependent bulk lifetime.

6.3 EXPERIMENT

The simulated data in Section 6.2 were generated by accurate modelling of the distribution of Δ*n* in a sample using known recombination parameters (within the limits of Quokka). Thus, following the same arguments as the one-dimensional case presented in Chapter 5, it is expected that this procedure is reversible. Fitting real measured data with an accurate Quokka model is expected to yield the most accurate J_{0m} extraction. Accuracy of the extracted J_{0m} is expected to be improved if the actual distribution of Δ*n* in a sample during a measurement can be modelled accurately. In this section, using measured data of actual samples, a Quokka-based extraction method is demonstrated. The previously discussed alternative methods are also applied to the measurements and the error in the extracted J_{0m} from the different methods is discussed.

6.3.1 EXPERIMENTAL METHODOLOGY

The investigated sample is an *n*-type, 3 Ωcm, 170 *μ*m thick, 156 × 156 cm² monocrystalline Si wafer symmetrically diffused with boron with R_{sht} of approximately 150 Ω/□ and passivated with a stack of AlO$_x$ and SiN$_x$. Silver paste was screen-printed onto one side of the sample in seven rectangular regions with varied f_{met} in the range 2-25 %. Importantly, the metallised fraction was varied by changing the contact width, with the contact pitch fixed at 1.8 mm. The open circuit PL image in Fig. 6-11 shows the layout of the sample and f_{met} for each metallised region.

Each metallised area and the non-metallised area marked as $f_{met} = 0$ % in Fig. 6-11 were individually measured using the QSSPL measurement setup described in Section 3.2.2. The PL measurement was self-consistently calibrated using a laser at lower illumination intensity and a subsequent high intensity flash lamp measurement was used to capture measurement data at high intensity. The calibration and data matching procedure are described in detail in Section 3.3.

The modified Kane-Swanson method and iV_{oc} method were then applied to the measured data. The Kane-Swanson method was applied directly to the injection dependent τ_{eff} data obtained for each metallised area. Suns-PL data were obtained by converting Δn_{av} to iV_{oc} using the known N_{dop} and Eq. (2-9), and converting G_{net} to suns assuming one sun generation current of 38 mA/cm². The methods were applied in the same way as Section 6.2 with J_{01} extracted from the Suns-PL data at one sun and Eq. (6-1) fitted to resulting plot of J_{01} against f_{met} for the iV_{oc} method, and $J_{0s,tot}$ extracted from

the τ_{eff} data at the same illumination intensity and Eq. (6-2) applied to the resulting plot of $J_{0s,tot}$ against f_{met} for the modified Kane-Swanson method.
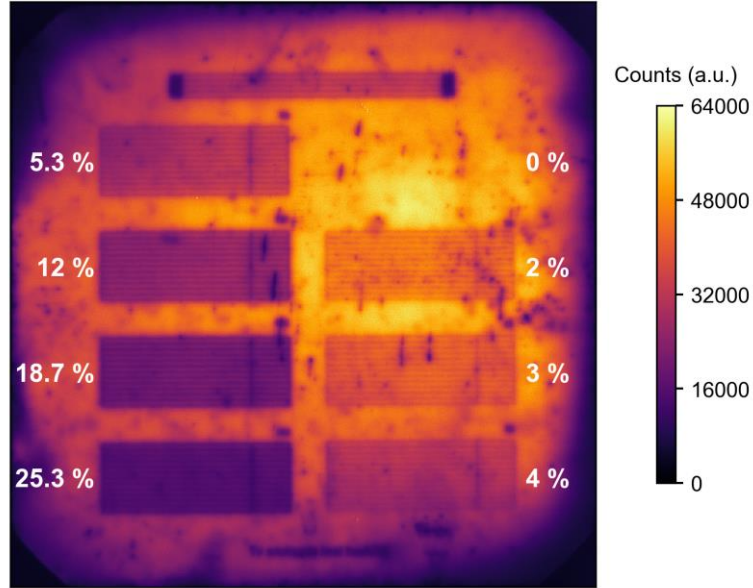
Fig. 6-11: Open circuit PL image of the test sample with varying contact fraction areas. Metal contact area fractions indicated on figure in white text.

Measured τ_{eff} data for each metallised area were also independently fitted with J_{0m} using Quokka version 2 following a similar procedure to Section 5.2.3. A two dimensional Quokka model with the same geometry as the test sample was created for each metallised area as well as a symmetrically passivated structure to simulate the non-metallised region. The injection dependent τ_{eff} data of the symmetrically passivated region were then fit using the curve fit function of Quokka with a constant bulk lifetime, τ_{const} and identical front and rear J_{0s} as free parameters. The τ_{eff} data from the metallised areas were then similarly fit with the obtained τ_{const} and J_{0s} fixed for the bulk lifetime and passivated surfaces, and a single J_{0m} for the contact area was fitted as a free parameter. There are several limitations to this fitting procedure that are discussed in Section 6.3.2.3.

6.3.2 EXPERIMENT RESULTS AND DISCUSSION

6.3.2.1 VARIED F_{MET} METHODS

J_{0m} extracted from the iV_{oc} data at one sun was 2,211 fA/cm². Using the modified Kane-Swanson method the extracted J_{0m} was 717 fA/cm² at one sun and 280 fA/cm² at $\Delta n_{av} = 10 N_{dop}$ (1.55 × 10¹⁶ cm⁻³). The data are shown in Fig. 6-12.
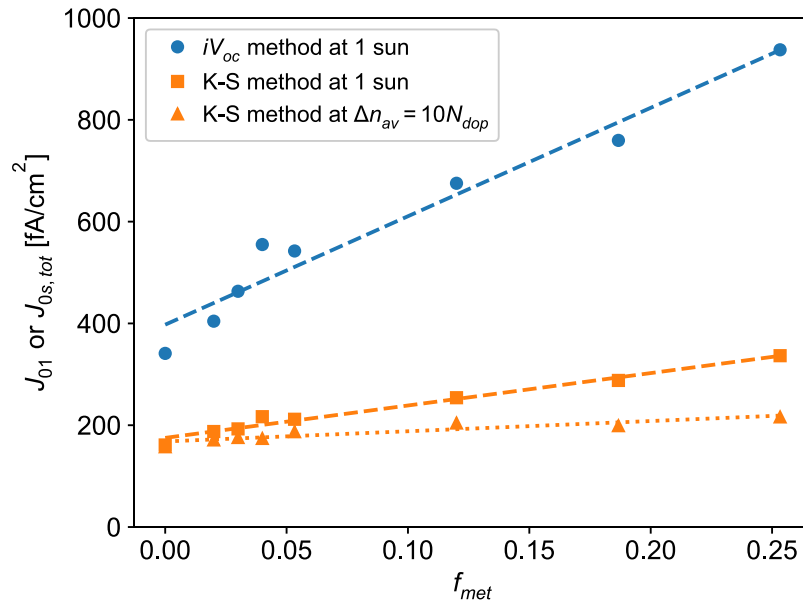
Fig. 6-12: J_{01} **and** $J_{0s,tot}$ **extracted from QSSPL measurements of the passivated and metallised test structure as a function of** f_{met}**.** J_{01} **was extracted at 1 sun for the** iV_{oc} **method and** $J_{0s,tot}$ **was extracted at 1 sun and** $\Delta n_{av} = 10N_{dop}$ **for the modified Kane-Swanson method. Dashed lines indicate linear fits.**

The trends are similar to the modelling in Section 6.2. The J_{01} extracted using the iV_{oc} method shows a steeper slope compared to $J_{0s,tot}$ extracted from the lifetime data at both injection levels. Comparing the slopes of the $J_{0s,tot}$ data, the data at the lower injection level (one sun) shows a steeper slope than the higher injection level ($10N_{dop}$). This is consistent with the explanation in Section 5.3.2, which showed that the higher the injection level, the stronger the difference between Δn at the metallised surface and Δn_{av}, and thus, the stronger the underestimation of the true J_{0m} when extracting data using the modified Kane-Swanson method.

Clearly there is a large difference between the extracted J_{0m} from the two used methods. From the modelling in Section 6.2 it is expected that the iV_{oc} method will be more accurate, so the Kane-Swanson extracted value can be discarded. It was also shown, though, that even when using the iV_{oc} method, J_{0m} is likely to be underestimated when measured using samples with width varied f_{met}, particularly when J_{0m} is high. For example, Fig. 6-6 shows 16 % underestimation for width varied f_{met} compared to 3 % underestimation for pitch varied f_{met}. The measured sample had R_{sht} approximately double that of the simulations (75 Ω/□ for simulations, 150 Ω/□ for measurement), so the error is expected to be even greater for the measurement. Thus, it is expected that $J_{0m} = 2,211$ fA/cm^2 is a 15 - 20 % underestimation.

6.3.2.2   QUOKKA FITTING METHOD

The initial fit was performed on the τ_{eff} data from the non-metallised region, as described in Section 5.2.3. This procedure resulted in τ_{const} = 330 μs and J_{0s} = 66 fA/cm². These parameters were assumed constant across the entire sample and thus were kept constant for all subsequent simulations of the metallised regions. Each metallised region was simulated independently with the injection-dependent τ_{eff} data simulated by Quokka fitted to the measured QSSPL lifetime data by varying the J_{0m} parameter in Quokka. The extracted J_{0m} for each metallised region is shown in Table 6-3 with the RMSE of the fit in Quokka. These data are also shown graphically in Fig. 6-13 with the J_{0m} obtained in Section 6.3.2.1 above for the iV_{oc} and modified Kane-Swanson methods also shown for comparison.

Table 6-3: *J_{0m}* extracted by independently fitting the lifetime data for each metallised region.

f_{met}	*J_{0m}* [fA/cm²]	*RMSE* [μs]
0.02	2,523	1.8
0.03	3,390	2.1
0.04	5,234	2.1
0.0533	3,804	1.8
0.12	3,109	1.2
0.1867	2,481	2.4
0.2533	2,576	2.5
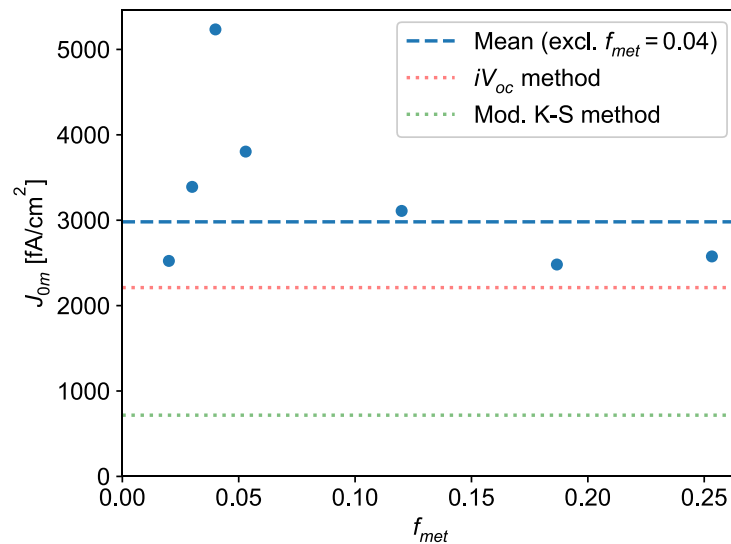
Fig. 6-13: *J_{0m}* data extracted from Quokka fits to *τ_{eff}* measurements for each metallised area in the test sample. Note that each *J_{0m}* datum is extracted from an independent *τ_{eff}* measurement. The *J_{0m}* extracted from the same data using the *iV_{oc}* method and the modified Kane-Swanson method are also shown as dotted lines.

Clearly there is considerable variation amongst the extracted J_{0m} data, which ranges from 2,481 – 5,234 fA/cm^2, nearly a factor of two difference. The maximum data point, obtained from the f_{met} = 0.04 metallised region could be excluded as an outlier, though, depending on what criteria are used. Exclusion of this point is also supported by the J_{01} data extracted with the iV_{oc} method for this metallised region. As shown in Fig. 6-12, the J_{01} for this metallised region lies far from the trend line. After excluding this point, the agreement between each independent measurement is not great, though the arithmetic mean of the remaining data is 2,981 fA/cm^2, approximately 35 % higher than the J_{0m} obtained from the iV_{oc} method. This is not inconsistent with the expected error in the iV_{oc} method. However, there are several improvements that could be made to increase the accuracy and reliability of the measurement. These are discussed in the next section.

6.3.2.3   LIMITATIONS OF THE EXPERIMENT

All three methods that were applied to extract J_{0m} from the measurements have some limitations which affect the reliability of the data.

All the methods assume that J_{0s} and τ_{bulk} are uniform across the whole sample. This assumption is unlikely to be strictly met given the observed non-uniformity of the PL response in the PL image in Fig. 6-11.

The design of the sample itself potentially limits the accuracy of the data. Since the sample contains full area diffusions on the front and rear, there is an electrical path for carriers to move between metallised regions. There are also carriers that are generated in the non-metallised regions that will "leak in" to the metallised regions, given that they are regions of higher recombination. It is also noted that the edges of the sample remain electrically connected to the other regions of the sample. Thus, any edge recombination also acts as a potential sink for carriers which could affect the accuracy of the extraction procedures. None of these effects are accounted for in any of the methods applied in this section. Potentially a full cell model approach [13] could account for these effects using the current sample design. Or, an alternative experimental design could be considered, where multiple samples are used and the QSSPL lifetime is measured before and after metallisation. This would follow a similar design to the experiment in Chapter 5.

In the f_{met} dependent extraction methods the model is applied to measurements of multiple metallised regions and only the change in the response is considered. This provides some statistical robustness against outliers. However, because width-varied f_{met} was used, the method is limited as it assumes that J_{0m} is independent of the contact

width (i.e. it is constant for all f_{met}). Void formation in screen-printed local Al-BSF contacts, for example, has been shown to have some dependence on the contact width [104]. Although it is uncertain that this affects front Ag metallisation in the same way, this is a seemingly unnecessary assumption that could be mitigated by using contact pitch variation instead of width variation. In that case the exact contact size of the final cell could be used in the test sample. Furthermore, the simulations in Section 6.2 also show that, all else being equal, pitch varied samples are expected to yield more accurate J_{0m} data because the varying lateral resistive loss is mitigated.

On the other hand, the Quokka fit method treats each metallised region entirely independently. This removes the restriction on J_{0m} being dependent on the contact width but ignores any extra statistical benefit of having multiple metallised regions. If indeed J_{0m} is not contact width dependent, or if the sample used pitch variation instead, this information would still be lost by using this method. A simple improvement would be to make repeat samples, which would increase the statistical power of the experiment so each J_{0m} would be extracted with greater certainty. Alternatively, the full cell model fitting procedures of Fell *et al.* [12] or Shanmugam *et al.* [13] are also able to make use of multiple samples of different f_{met}, though they do also assume that J_{0m} is independent of f_{met}.

6.4 CONCLUSIONS

This chapter has explored measurement techniques to extract J_{0m} of partial metal contacts. The class of techniques which rely on varying f_{met} were studied using simulated data and measurements. It is shown that the technique which uses J_{01} extracted from Suns-PL data is most accurate because it is area averaged, so is better able to account for lateral effects. It also minimises the number of assumptions about a particular sample and uses the change in recombination between samples as the key indicator of J_{0m}.

The Suns-V_{oc} based technique for cells suffers from being a local measurement and inaccurate when lateral transport losses are significant, such as when the pitch is wide or R_{sht} is high.

The modified Kane-Swanson based method is also less accurate than the iV_{oc} method. Although it is area-averaged, the strong assumption that Δn is uniform for each measurement causes errors. This is especially true when J_{0m} is significantly higher than the J_{0s}.

A further interesting conclusion from the modelling is that all of the methods tend to yield more accurate J_{0m} when f_{met} is varied by changing the pitch of a fixed contact size, rather than changing the size of the contact. This has the added advantage of not requiring an assumption that J_{0m} is independent of contact size.

Finally, simulations of the injection dependence of the J_{0m} extraction techniques suggest that accuracy is improved for lower illumination intensities, though further work is required to determine if this is true for practical samples which include an injection dependent τ_{bulk}.

Measurements of one sample showed data that agreed qualitatively with the conclusions of the modelling about the iV_{oc} and modified Kane-Swanson method. A Quokka based fitting method also yielded J_{0m} data that were consistent with the modelling and potentially more accurate. However, several limitations of the experiment would have to be overcome to make stronger conclusions about accuracy.

CHAPTER 7: SUMMARY AND OUTLOOK

The principal aim of this thesis is to investigate the use of dynamic PL measurements for measuring recombination of metallised test structures and cells. Two dynamic PL measurement setups were constructed, and experiments and simulations were performed to this aim.

The developed systems were shown to be more easily applied to metallised samples than traditional QSSPC measurements, and in many important use cases, more accurate than Suns-V_{oc} measurements. The comparatively simple system design and dynamic calibration makes them an attractive alternative to PL imaging systems for quantitative analysis of metallised samples. An important advance highlighted in Chapter 3 is the addition of a lens in front of the PL detector in the measurement setup. This allows large samples to be fully illuminated with PL detected from only a smaller area of interest. Previously described systems could only achieve focused detection through use of apertures [76]. This is important in the context of measuring metallised samples because the metal increases the lateral conductivity, which enables current to flow parasitically to shaded regions of the sample during measurements if an aperture is used.

In Chapter 4, previously observed deviations at high illumination intensities between Suns-V_{oc} and Suns-PL measurements were investigated. Detailed simulations showed that lateral non-uniformity in generation rate and/or recombination rate in combination with a finite lateral series resistance leads to laterally non-uniform Δn, which causes these deviations. In contrast to the earlier work, our new measurement set up enables PL detection from the illuminated front side, thereby allowing this type of experiments to be performed on a wider range of cell types. Simultaneous measurements of Suns-V_{oc} and Suns-PL were made of two typical cell structures and the same previously reported deviations were observed. A third cell with a known Schottky contact was also observed to demonstrate the deviation. In general terms, these findings highlight a fundamental difference between Suns-V_{oc} measurements, which measure the voltage locally at the cell contacts, and Suns-PL measurements which are area-averaged. The effects discussed above and Schottky contact effects both act to reduce the voltage at the contact without significantly reducing the average local voltage across the entire cell. As a result of this fundamental difference, it was shown that large errors are associated with using Suns-V_{oc} data for conversion to injection-dependent minority carrier lifetime data and subsequent calculation of $J_{0s,tot}$ using the modified Kane-Swanson method. This procedure was shown to result in significant errors for most typical cell designs because

the lateral resistance network is optimised for one sun operation, but the measurement procedure requires illumination intensities greatly exceeding one sun to reach high carrier injection conditions. A combination of Suns-PL and Suns-V_{oc} appears to be an excellent combination. The Suns-PL data provide the basis for accurate injection-dependent lifetime data on cells, while Suns-V_{oc} can be used for accurate calibration of the PL data at low illumination intensities.

Having established the usefulness of dynamic PL measurements for measuring the average recombination in a sample, Chapters 5 and 6 thoroughly investigated applying dynamic PL measurements to measure the surface recombination at metallised surfaces. In Chapter 5, Injection dependent τ_{eff} measurements of full area metallised Si samples were analysed using two methods based on the modified Kane-Swanson approach, and also using software simulations. The Kane-Swanson based methods rely on the assumption of uniform Δn, and it was shown that this assumption is invalid for these measurements and indeed generally for metallised samples, because strongly asymmetrical surface recombination causes Δn to vary strongly with depth in the sample. The short wavelength illumination, which is required by most PL-based techniques, enhances this non-uniformity by a small amount, but is not the dominant factor. The simulation based extraction technique simulates the Δn profile, which overcomes this limitation and results in more accurate parameters. Simulations were used to quantify the errors caused by applying the Kane-Swanson based approach. A methodology was also provided to assess the sensitivity of the simulation based curve fitting approach.

A comprehensive review of reported J_{0m} extraction methodologies in Chapter 2 revealed a wide variety of approaches that had previously been applied to different types of samples. An investigation into the class of techniques based on varying f_{met} is presented in Chapter 6. Simulated data and measurements showed that the technique which uses J_{01} extracted from Suns-PL data is most accurate because it is area averaged and therefore more accurately accounts for lateral effects. As was concluded in Chapter 4, the Suns-V_{oc} based technique for cells suffers from being a local measurement and is therefore inaccurate when lateral transport losses are significant, such as when the pitch is wide, or the sheet resistance is high. The modified Kane-Swanson based extraction method is also less accurate than the iV_{oc} method for both fully processed cells and for specific PL test structures. Although it is area-averaged, the key assumption that Δn is uniform for each measurement causes errors. This is especially true when J_{0m} is significantly higher than J_{0s}. This result corroborates well with the findings from the one-dimensional analysis in Chapter 5.

A further conclusion from the modelling in Chapter 6 is that all of the methods tend to yield more accurate J_{0m} when f_{met} is varied by changing the pitch of a fixed contact size, rather than changing the size of the contact. This has the added advantage of not requiring an assumption about J_{0m} being independent of contact size, which can be a problem, for example when measuring some types of screen-printed contacts [104]. Both f_{met} variation approaches are found in the literature without reference to the relevance of the choice, which highlights the significance of this contribution.

Overall, it has been shown that PL measurements are well suited for quantitative measurements of the average or overall recombination of a device, in the context of measuring recombination of metal contacts. Dynamic PL measurements allow a more simplified experimental setup to be used, though care must be taken to accurately calibrate the PL data. Metal contact recombination also presents a particular challenge because it typically introduces non-uniformity to the surface recombination, either depth-wise as in the full rear metallisation of Chapter 5, or laterally as is the case for partially metallised samples, the latter analysed in Chapter 6. This non-uniform surface recombination tends to cause non-uniform excess carrier distribution throughout the sample, which limits the accuracy of J_{0m} extraction methods that assume uniform carrier density such as the modified Kane-Swanson method. Generally, techniques which are based on simulations of the full device geometry such as the method presented in this thesis can better account for the non-uniformity and are thus more accurate.

7.1 FUTURE WORK

There are several opportunities for further study resulting from the contributions in this thesis.

The simulations in Chapter 4 showed that shading and metal recombination can cause deviations between Suns-V_{oc} and Suns-PL curves, but also pointed out that Schottky contacts can cause a similar deviation. It is unclear, however, whether the comparison between Suns-PL and Suns-V_{oc} can provide quantitative information about the underlying cause of experimentally observed deviations in a sample. For example, this deviation should be related to R_{sht} if the deviation is caused by the lateral series resistance. Fitting an appropriately adjusted cell model to the Suns-V_{oc} and Suns-PL data could yield such information. Alternatively, a voltage calibrated PL image could yield quantitative information about the lateral differences in the local voltage that could also be used.

Quokka based J_{0m} extraction from the measurements in Chapter 6 could be further improved by better utilising the fact that each metallised region of interest is not independent of the other. As discussed in Section 2.3.4, Fell *et al.* [12] show how this can be achieved by fitting the simulated recombination current at each contact to the same diode model, however they do not account for lateral current flow between regions of interest. The Griddler based approach of Shanmugam *et al.* [13] does account for lateral current flow but does not simulate the Δn distribution in the device to the same level of detail. It appears that a combination of both approaches would lead to the most accurate results.

The simulations in Chapter 6 show that all of the f_{met} based J_{0m} extraction methods yield more accurate J_{0m} when f_{met} is varied by changing the pitch of a fixed contact size rather than changing the width of the contact. Experimental verification of this result will be the subject of a future study.

Finally, it was concluded in Chapter 6 that the J_{0m} derived from fitting the f_{met} model to J_{01} data from the Suns-PL curves was more accurate than fitting it to the $J_{0s,tot}$ data from the injection dependent τ_{eff} curves, because of the less stringent assumptions. Given the ubiquity of the modified Kane-Swanson method for measurements of J_{0s} and J_{0e} in non-metallised applications, there is potential to investigate further if this approach can be expanded to include those cases.

APPENDIX: PUBLICATION LIST

PEER-REVIEWED JOURNAL PUBLICATIONS

R. Dumbrell, M. K. Juhl, T. Trupke, and Z. Hameiri, "Comparison of terminal and implied open-circuit voltage measurements," *IEEE Journal of Photovoltaics*, vol. 7, no. 5, pp. 1376–1383, 2017.

R. Dumbrell, M. K. Juhl, T. Trupke, and Z. Hameiri, "Extracting metal contact recombination parameters from effective lifetime data," *IEEE Journal of Photovoltaics*, vol. 8, no. 6, pp. 1413–1420, 2018.

CONFERENCE CONTRIBUTIONS

R. Dumbrell, M. K. Juhl, M. Li, T. Trupke, and Z. Hameiri, "Effective lifetime of full rear metallized cells by quasi-steady-state photoluminescence," in *26th International Photovoltaic Science and Engineering Conference*, 2016.

R. Dumbrell, M. K. Juhl, T. Trupke, and Z. Hameiri, "On the use of voltage measurements for determining carrier lifetime at high illumination intensity," in *44th IEEE Photovoltaic Specialists Conference*, 2017.

R. Dumbrell, M. K. Juhl, M. Li, T. Trupke, and Z. Hameiri, "Metal induced contact recombination measured by quasi-steady-state photoluminescence," in *44th IEEE Photovoltaic Specialists Conference*, 2017.

R. Dumbrell, M. K. Juhl, T. Trupke, and Z. Hameiri, "Extracting surface saturation current density from lifetime measurements of samples with metallized surfaces," in *7th World Conference on Photovoltaic Energy Conversion*, 2018.

REFERENCES

[1]   VDMA, "International Technology Roadmap for Photovoltaic (ITRPV)," 2019.

[2]   International Energy Agency (IEA), "World Energy Outlook 2018," 2018.

[3]   W. Deng, F. Ye, R. Liu, Y. Li, H. Chen, Z. Xiong, Y. Yang, Y. Chen, Y. Wang, P. P. Altermatt, Z. Feng, and P. J. Verlinden, "22.61% efficient fully screen printed PERC solar cell," in *44th IEEE Photovoltaic Specialists Conference*, 2017.

[4]   P. Saint-Cast, S. Werner, J. Greulich, U. Jäger, E. Lohmüller, H. Höffler, and R. Preu, "Analysis of the losses of industrial-type PERC solar cells," *Physica Status Solidi (A) Applications and Materials Science*, vol. 214, no. 3, p. 1600708, 2017.

[5]   M. A. Green, "The passivated emitter and rear cell (PERC): From conception to mass production," *Solar Energy Materials and Solar Cells*, vol. 143, pp. 190–197, 2015.

[6]   J. Benick, A. Richter, R. Müller, H. Hauser, F. Feldmann, P. Krenckel, S. Riepe, F. Schindler, M. C. Schubert, M. Hermle, A. W. Bett, and S. W. Glunz, "High-efficiency n-type HP mc silicon solar cells," *IEEE Journal of Photovoltaics*, vol. 7, no. 5, pp. 1171–1175, 2017.

[7]   R. A. Sinton and A. Cuevas, "Contactless determination of current – voltage characteristics and minority carrier lifetimes in semiconductors from quasi-steady-state photoconductance data," *Applied Physics Letters*, vol. 69, no. 17, pp. 2510–2512, 1996.

[8]   R. A. Sinton and A. Cuevas, "A quasi-steady-state open-circuit voltage method for solar cell characterization," in *16th European Photovoltaic Solar Energy Conference*, 2000, pp. 1152–1155.

[9]   T. Trupke and R. A. Bardos, "Photoluminescence: A surprisingly sensitive lifetime technique," in *31st IEEE Photovoltaic Specialists Conference*, 2005, pp. 903–906.

[10]   T. Trupke, R. A. Bardos, M. C. Schubert, and W. Warta, "Photoluminescence imaging of silicon wafers," *Applied Physics Letters*, vol. 89, no. 4, p. 044107, 2006.

[11]   C. Comparotto, J. Theobald, J. Lossen, and V. D. Mihailetchi, "Understanding contact formation on n-PERT-RJ solar cells," in *33rd European Photovoltaic Solar*

Energy Conference and Exhibition, 2017, pp. 832–836.

[12]   A. Fell, D. Walter, S. Kluska, E. Franklin, and K. Weber, "Determination of injection dependent recombination properties of locally processed surface regions," *Energy Procedia*, vol. 38, pp. 22–31, 2013.

[13]   V. Shanmugam, T. Mueller, A. G. Aberle, and J. Wong, "Determination of metal contact recombination parameters for silicon wafer solar cells by photoluminescence imaging," *Solar Energy*, vol. 118, pp. 20–27, 2015.

[14]   H. Nagel, C. Berge, and A. G. Aberle, "Generalized analysis of quasi-steady-state and quasi-transient measurements of carrier lifetimes in semiconductors," *Journal of Applied Physics*, vol. 86, no. 11, p. 6218, 1999.

[15]   T. Trupke, R. A. Bardos, and M. D. Abbott, "Self-consistent calibration of photoluminescence and photoconductance lifetime measurements," *Applied Physics Letters*, vol. 87, p. 184102, 2005.

[16]   S. M. Sze and K. K. Ng, *Physics of Semiconductor Devices*, 3rd ed. Hoboken, New Jersey: John Wiley & Sons, Inc., 2007.

[17]   A. Richter, S. W. Glunz, F. Werner, J. Schmidt, and A. Cuevas, "Improved quantitative description of Auger recombination in crystalline silicon," *Physical Review B*, vol. 86, no. 16, p. 165202, 2012.

[18]   W. Shockley and W. T. Read, "Statistics of the Recombination of Holes and Electrons," *Physical Review*, vol. 87, no. 46, pp. 835–842, 1952.

[19]   R. N. Hall, "Electron-hole Recombination in Germanium," *Physical Review*, vol. 87, p. 387, 1952.

[20]   A. McEvoy, T. Markvart, and L. Castañer, *Solar Cells: Materials, Manufacture and Operation*, 2nd ed. Elsevier, 2013.

[21]   A. A. Istratov, T. Buonassisi, R. J. McDonald, A. R. Smith, R. Schindler, J. A. Rand, J. P. Kalejs, and E. R. Weber, "Metal content of multicrystalline silicon for solar cells and its impact on minority carrier diffusion length," *Journal of Applied Physics*, vol. 94, no. 10, pp. 6552–6559, 2003.

[22]   H. J. Möller, C. Funke, M. Rinio, and S. Scholz, "Multicrystalline silicon for solar cells," *Thin Solid Films*, vol. 487, no. 1–2, pp. 179–187, 2005.

[23] D. K. Schroder, *Semiconductor Material and Device Characterization*, 3rd ed. Hoboken, New Jersey: John Wiley & Sons, Inc., 2006.

[24] M. A. Green, *Silicon Solar Cells: Advanced Principles & Practice*. Sydney, NSW: University of New South Wales, 1995.

[25] T. Trupke, M. a. Green, P. Würfel, P. P. Altermatt, A. Wang, J. Zhao, and R. Corkish, "Temperature dependence of the radiative recombination coefficient of intrinsic crystalline silicon," *Journal of Applied Physics*, vol. 94, no. 8, p. 4930, 2003.

[26] "PV Lighthouse Recombination Calculator." [Online]. Available: https://www2.pvlighthouse.com.au/calculators/Recombination calculator/Recombination calculator.aspx. [Accessed: 26-May-2019].

[27] A. A. Istratov, H. Hieslmair, and E. R. Weber, "Iron and its complexes in silicon," *Applied Physics A*, vol. 69, no. 1, pp. 13–44, 1999.

[28] J. A. del Alamo and R. M. Swanson, "The physics and modeling of heavily doped emitters," *IEEE Transactions on Electron Devices*, vol. 31, no. 12, pp. 1878–1888, 1984.

[29] A. G. Aberle, *Crystalline Silicon Solar Cells: Advanced Surface Passivation and Analysis*. Sydney, NSW: University of New South Wales, 1999.

[30] K. R. McIntosh and L. E. Black, "On effective surface recombination parameters," *Journal of Applied Physics*, vol. 116, no. 1, 2014.

[31] A. Cuevas, "The Recombination Parameter J0," *Energy Procedia*, vol. 55, pp. 53–62, 2014.

[32] M. A. Green, *Solar Cells: Operating Principles, Technology and System Applications*. Kensington, NSW: University of New South Wales, 1992.

[33] Martin Wolf & Hans Rauschenbach, "Series resistance effects measurements," *Advanced Energy Conversion*, vol. 3, no. 2, pp. 455–479, 1963.

[34] R. A. Sinton, A. Cuevas, and M. Stuckings, "Quasi-steady-state photoconductance, a new method for solar cell material and device characterization," in *25th IEEE Photovoltaic Specialists Conference*, 1996, pp. 457–460.

[35] P. Würfel, "The chemical potential of radiation," *Journal of Physics C: Solid State Physics*, vol. 15, pp. 3967–3985, 1982.

[36] T. Fuyuki, H. Kondo, T. Yamazaki, Y. Takahashi, and Y. Uraoka, "Photographic surveying of minority carrier diffusion length in polycrystalline silicon solar cells by electroluminescence," *Applied Physics Letters*, vol. 86, p. 262108, 2005.

[37] T. Trupke, R. A. Bardos, F. Hudert, P. Würfel, J. Zhao, A. Wang, and M. A. Green, "Effective excess carrier lifetimes exceeding 100 milliseconds in float zone silicon determined from photoluminescence," in *19th European Photovoltaic Solar Energy Conference*, 2004, pp. 758–761.

[38] P. P. Altermatt, F. Geelhaar, T. Trupke, X. Dai, A. Neisser, and E. Daub, "Injection dependence of spontaneous radiative recombination in crystalline silicon: Experimental verification and theoretical analysis," *Applied Physics Letters*, vol. 88, no. 26, p. 261901, 2006.

[39] T. Trupke, "Influence of photon reabsorption on quasi-steady-state photoluminescence lifetime measurement on crystalline silicon," *Journal of Applied Physics*, vol. 100, p. 063531, 2006.

[40] K. Bothe and D. Hinken, "Chapter Five - Quantitative Luminescence Characterization of Crystalline Silicon Solar Cells," in *Advances in Photovoltaics: Part 2*, vol. 89, G. P. Willeke and E. R. Weber, Eds. Elsevier, 2013, pp. 259–339.

[41] M. J. Kerr, A. Cuevas, and R. A. Sinton, "Generalized analysis of quasi-steady-state and transient decay open circuit voltage measurements," *Journal of Applied Physics*, vol. 91, no. 1, pp. 399–404, 2002.

[42] J. A. Giesecke, S. W. Glunz, and W. Warta, "Understanding and resolving the discrepancy between differential and actual minority carrier lifetime," *Journal of Applied Physics*, vol. 113, no. 7, 2013.

[43] "WCT-120 – The standard offline wafer-lifetime tool." [Online]. Available: https://www.sintoninstruments.com/products/wct-120/. [Accessed: 31-May-2019].

[44] S. Rein, P. Lichtner, W. Warta, and S. W. Glunz, "Advanced defect characterization by combining temperature- and injection-dependent lifetime spectroscopy (TDLS and IDLS)," in *29th IEEE Photovoltaic Specialists Conference*, 2002, pp. 190–193.

[45] B. Hoex, S. B. S. Heil, E. Langereis, M. C. M. Van De Banden, and W. M. M. Kessels, "Ultralow surface recombination of c-Si substrates passivated by plasma-assisted atomic layer deposited Al2O3," *Applied Physics Letters*, vol. 89, no. 4, pp. 9–12, 2006.

[46] J. Lindroos and H. Savin, "Review of light-induced degradation in crystalline silicon solar cells," *Solar Energy Materials and Solar Cells*, vol. 147, pp. 115–126, 2016.

[47] D. H. Macdonald and A. Cuevas, "Trapping of minority carriers in multicrystalline silicon," *Applied Physics Letters*, vol. 74, no. 12, p. 1710, 1999.

[48] M. Bail, M. Schulz, and R. Brendel, "Space-charge region-dominated steady-state photoconductance in low-lifetime Si wafers," *Applied Physics Letters*, vol. 82, no. 5, p. 757, 2003.

[49] J. Deckers, M. Debucquoy, I. Gordon, R. Mertens, and J. Poortmans, "Avoiding parasitic current flow through point contacts in test structures for QSSPC contact recombination current measurements," *IEEE Journal of Photovoltaics*, vol. 5, no. 1, pp. 276–281, 2015.

[50] J. Wong, S. Raj, J. W. Ho, J. Wang, and J. Lin, "Voltage loss analysis for bifacial silicon solar cells: Case for two-dimensional large-area modeling," *IEEE Journal of Photovoltaics*, vol. 6, no. 6, pp. 1421–1426, 2016.

[51] S. W. Glunz, J. Nekarda, H. Mäckel, and A. Cuevas, "Analyzing back contacts of silicon solar cells by Suns-Voc measurements at high illumination densities," in *22nd European Photovoltaic Solar Energy Conference and Exhibition*, 2007, pp. 849–853.

[52] J. A. Giesecke, M. C. Schubert, D. Walter, and W. Warta, "Minority carrier lifetime in silicon wafers from quasi-steady-state photoluminescence," *Applied Physics Letters*, vol. 97, no. 9, 2010.

[53] T. Trupke, R. A. Bardos, M. D. Abbott, and J. E. Cotter, "Suns-photoluminescence: Contactless determination of current-voltage characteristics of silicon wafers," *Applied Physics Letters*, vol. 87, p. 093503, 2005.

[54] J. Wong, S. Duttagupta, R. Stangl, B. Hoex, and A. G. Aberle, "A systematic loss analysis method for rear-passivated silicon solar cells," *IEEE Journal of*

Photovoltaics, vol. 5, no. 2, pp. 619–626, 2015.

[55] J. A. Giesecke, M. C. Schubert, and W. Warta, "Self-sufficient minority carrier lifetime in silicon from quasi-steady-state photoluminescence," *Physica Status Solidi (A) Applications and Materials Science*, vol. 209, no. 11, pp. 2286–2290, 2012.

[56] J. Giesecke, *Quantitative Recombination and Transport Properties in Silicon from Dynamic Luminescence*. Switzerland: Springer International Publishing, 2014.

[57] J. A. Giesecke, M. C. Schubert, and W. Warta, "Carrier lifetime from dynamic electroluminescence," *IEEE Journal of Photovoltaics*, vol. 3, no. 3, pp. 1012–1015, 2013.

[58] I. Zafirovska, M. K. Juhl, J. W. Weber, O. Kunz, and T. Trupke, "Module inspection using line-scanning photoluminescence imaging," in *32nd European Photovoltaic Solar Energy Conference*, 2016, pp. 1826–1829.

[59] D. E. Kane and R. M. Swanson, "Measurement of the emitter saturation current by a contactless photoconductivity decay method," in *18th IEEE Photovoltaic Specialists Conference*, 1985, pp. 578–583.

[60] R. R. King, R. A. Sinton, and R. M. Swanson, "Studies of diffused phosphorus emitters: saturation current, surface recombination velocity, quantum efficiency," *IEEE Transactions on Electron Devices*, vol. 37, no. 2, pp. 365–371, 1990.

[61] A. L. Blum, J. S. Swirhun, R. A. Sinton, and A. Kimmerle, "An updated analysis to the WCT-120 QSSPC measurement system using advanced device physics," in *28th European Photovoltaic Solar Energy Conference and Exhibition*, 2013, pp. 1521–1523.

[62] A. Kimmerle, J. Greulich, and A. Wolf, "Carrier-diffusion corrected J0-analysis of charge carrier lifetime measurements for increased consistency," *Solar Energy Materials and Solar Cells*, vol. 142, pp. 116–122, 2015.

[63] H. Mäckel and K. Varner, "On the determination of the emitter saturation current density from lifetime measurements of silicon devices," *Progress in Photovoltaics: Research and Applications*, vol. 21, pp. 850–866, 2013.

[64] A. B. Sproul, "Dimensionless solution of the equation describing the effect of

surface recombination on carrier decay in semiconductors," *Journal of Applied Physics*, vol. 76, no. 5, pp. 2851–2854, 1994.

[65] B. Min, A. Dastgheib-Shirazi, P. P. Altermatt, and H. Kurz, "Accurate determination of the emitter saturation current density for industrial P-diffused emitters," in *29th European Photovoltaic Solar Energy Conference and Exhibition*, 2014, pp. 463–466.

[66] J. Müller, K. Bothe, S. Herlufsen, H. Hannebauer, R. Ferré, and R. Brendel, "Reverse saturation current density imaging of highly doped regions in silicon: A photoluminescence approach," *Solar Energy Materials and Solar Cells*, vol. 106, no. 4, pp. 76–79, Nov. 2012.

[67] J. Müller, K. Bothe, S. Herlufsen, T. Ohrdes, and R. Brendel, "Reverse saturation current density imaging of highly doped regions in silicon employing photoluminescence measurements," *IEEE Journal of Photovoltaics*, vol. 2, no. 4, pp. 473–478, 2012.

[68] B. Fischer, "Loss analysis of crystalline silicon solar cells using photoconductance and quantum efficiency measurements," Universitat Konstanz, 2003.

[69] J. Müller, K. Bothe, S. Gatz, F. Haase, C. Mader, R. Brendel, J. Müller, K. Bothe, S. Gatz, F. Haase, C. Mader, and R. Brendel, "Recombination at laser-processed local base contacts by dynamic infrared lifetime mapping," *Journal of Applied Physics*, vol. 108, no. 12, p. 124513, Dec. 2010.

[70] J. Müller, K. Bothe, S. Gatz, H. Plagwitz, G. Schubert, and R. Brendel, "Contact formation and recombination at screen-printed local aluminum-alloyed silicon solar cell base contacts," *IEEE Transactions on Electron Devices*, vol. 58, no. 10, pp. 3239–3245, 2011.

[71] K. Ramspeck, S. Reissenweber, J. Schmidt, K. Bothe, and R. Brendel, "Dynamic carrier lifetime imaging of silicon wafers using an infrared-camera-based approach," *Applied Physics Letters*, vol. 93, no. 10, 2008.

[72] T. Fellmeth, A. Born, A. Kimmerle, F. Clement, D. Biro, and R. Preu, "Recombination at metal-emitter interfaces of front contact technologies for highly efficient silicon solar cells," *Energy Procedia*, vol. 8, pp. 115–121, 2011.

[73] D. Inns and D. Poplavskyy, "Measurement of metal induced recombination in solar

cells," in *42nd IEEE Photovoltaic Specialists Conference*, 2015.

[74]   A. Fell, "A free and fast three-dimensional/two-dimensional solar cell simulator featuring conductive boundary and quasi-neutrality approximations," *IEEE Transactions on Electron Devices*, vol. 60, no. 2, pp. 733–738, 2013.

[75]   J. Wong, "Griddler: Intelligent computer aided design of complex solar cell metallization patterns," in *39th IEEE Photovoltaic Specialists Conference*, 2013, pp. 933–938.

[76]   J. A. Giesecke, B. Michl, F. Schindler, M. C. Schubert, and W. Warta, "Minority carrier lifetime of silicon solar cells from quasi-steady-state photoluminescence," *Solar Energy Materials and Solar Cells*, vol. 95, no. 7, pp. 1979–1982, 2011.

[77]   J. A. Giesecke and W. Warta, "Microsecond carrier lifetime measurements in silicon via quasi-steady-state photoluminescence," *Progress in Photovoltaics: Research and Applications*, vol. 20, no. 2, pp. 238–245, 2012.

[78]   J. S. Swirhun, R. A. Sinton, M. K. Forsyth, and T. Mankad, "Contactless measurement of minority carrier lifetime in silicon ingots and bricks," *Progress in Photovoltaics: Research and Applications*, vol. 19, no. 3, pp. 313–319, 2011.

[79]   "PVLighthouse Spectrum Library." [Online]. Available: https://www2.pvlighthouse.com.au/resources/optics/spectrum library/spectrum library.aspx. [Accessed: 26-May-2019].

[80]   Thorlabs, "SM05PD5A - Mounted InGaAs Photodiode." [Online]. Available: https://www.thorlabs.com/thorproduct.cfm?partnumber=SM05PD5A. [Accessed: 26-May-2019].

[81]   Femto, "Variable Gain Low Noise Current Amplifier DLPCA-200." [Online]. Available: https://www.femto.de/en/products/current-amplifiers/variable-gain-up-to-500-khz-dlpca.html. [Accessed: 31-May-2019].

[82]   Z. Hameiri, T. Trupke, N. Gao, R. A. Sinton, and J. W. Weber, "Effective bulk doping concentration of diffused and undiffused silicon wafers obtained from combined photoconductance and photoluminescence measurements," *Progress in Photovoltaics: Research and Applications*, vol. 21, no. 5, pp. 942–949, 2013.

[83]   R. A. Sinton and T. Trupke, "Limitations on dynamic excess carrier lifetime

calibration methods," *Progress in Photovoltaics: Research and Applications*, vol. 20, no. 2, pp. 246–249, 2012.

[84] J. A. Giesecke and W. Warta, "Understanding carrier lifetime measurements at nonuniform recombination," *Applied Physics Letters*, vol. 104, no. 8, p. 082103, 2014.

[85] M. K. Juhl and T. Trupke, "The impact of voltage independent carriers on implied voltage measurements on silicon devices," *Journal of Applied Physics*, vol. 120, no. 16, 2016.

[86] A. Cuevas and S. López-Romero, "The combined effect of non-uniform illumination and series resistance on the open-circuit voltage of solar cells," *Solar Cells*, vol. 11, no. 2, pp. 163–173, 1984.

[87] N. P. Harder, A. B. Sproul, T. Brammer, and A. G. Aberle, "Effects of sheet resistance and contact shading on the characterization of solar cells by open-circuit voltage measurements," *Journal of Applied Physics*, vol. 94, no. 4, pp. 2473–2479, 2003.

[88] J. Greulich, M. Glatthaar, A. Krieg, G. Emanuel, and S. Rein, "JV characteristics of industrial silicon solar cells: Influence of distributed series resistance and Shockley Read Hall recombination," in *24th European Solar Energy Conference and Exhibition*, 2009, pp. 2065–2069.

[89] A. L. Blum, R. A. Sinton, W. Dobson, H. Wilterdink, and J. H. Dinger, "Lifetime and substrate doping measurements of solar cells and application to in-line process control," in *43rd IEEE Photovoltaic Specialists Conference*, 2016, pp. 3534–3537.

[90] A. Fell, K. R. McIntosh, P. P. Altermatt, G. J. M. Janssen, R. Stangl, A. Ho-baillie, H. Steinkemper, J. Greulich, M. Müller, B. Min, K. C. Fong, M. Hermle, I. G. Romjin, and M. D. Abbott, "Input Parameters for the Simulation of Silicon Solar Cells in 2014," *IEEE Journal of Photovoltaics*, vol. 5, no. 4, pp. 495–496, 2015.

[91] T. Trupke, E. Pink, R. A. Bardos, and M. D. Abbott, "Spatially resolved series resistance of silicon solar cells obtained from luminescence imaging," *Applied Physics Letters*, vol. 90, no. 9, pp. 1–4, 2007.

[92] E. Schneiderlöchner, R. Preu, R. Lüdemann, and S. W. Glunz, "Laser-fired rear contacts for crystalline silicon solar cells," *Progress in Photovoltaics: Research*

and Applications, vol. 10, no. 1, pp. 29–34, 2002.

[93]   J. Deckers, X. Loozen, N. Posthuma, B. O'Sullivan, M. Debucquoy, S. Singh, M. Aleman, M. Recaman Payo, I. Gordan, P. J. Verlinden, R. Mertens, and J. Poortmans, "Injection dependent emitter saturation current density measurement under metallized areas using photoconductance decay," in *28th European Photovoltaic Solar Energy Conference and Exhibition*, 2013, pp. 806–810.

[94]   G. J. M. Janssen, Y. Wu, K. C. J. J. Tool, I. G. Romijn, and A. Fell, "Extraction of recombination properties from lifetime data," *Energy Procedia*, vol. 92, pp. 88–95, 2016.

[95]   A. F. Thomson, N. E. Grant, K. F. Chern, and T. Kho, "Improved diffused-region recombination-current pre-factor analysis," *Energy Procedia*, vol. 55, pp. 141–148, 2014.

[96]   P. P. Altermatt, J. O. Schumacher, A. Cuevas, M. J. Kerr, S. W. Glunz, R. R. King, G. Heiser, and A. Schenk, "Numerical modeling of highly doped Si:P emitters based on Fermi-Dirac statistics and self-consistent material parameters," *Journal of Applied Physics*, vol. 92, no. 6, pp. 3187–3197, 2002.

[97]   K. R. Mcintosh and S. C. Baker-finch, "OPAL 2 : Rapid optical simulation of silicon solar cells," in *38th IEEE Photovoltaic Specialists Conference*, 2012, pp. 265–271.

[98]   D. B. M. Klaassen, "A unified mobility model for device simulation - I. Model equations and concentration dependence," *Solid-State Electronics*, vol. 35, no. 7. pp. 953–959, 1991.

[99]   A. Schenk, "Finite-temperature full random-phase approximation model of band gap narrowing for silicon device simulation," *Journal of Applied Physics*, vol. 84, no. 7, pp. 3684–3695, 1998.

[100] E. Franklin, K. C. Fong, K. R. McIntosh, A. Fell, A. Blakers, T. Kho, D. Walter, D. Wang, N. Zin, M. Stocks, E.-C. Wang, N. E. Grant, Y. Wan, Y. Yang, X. Zhang, Z. Feng, and P. J. Verlinden, "Design, fabrication and characterisation of a 24.4% efficient interdigitated back contact solar cell," *Progress in Photovoltaics: Research and Applications*, vol. 24, no. 4, pp. 411–427, Apr. 2016.

[101] R. Dumbrell, M. K. Juhl, M. Li, T. Trupke, and Z. Hameiri, "Metal induced contact recombination measured by quasi-steady-state photoluminescence," in *44th IEEE*

Photovoltaic Specialists Conference, 2017.

[102] M. Li, J. Wong, N. Chen, A. G. Aberle, and R. Stangl, "Determination of metallization-induced recombination losses of screen-printed silicon solar cell contacts and their dependence on the doping profile," *IEEE Journal of Photovoltaics*, vol. 8, no. 6, pp. 1470–1477, 2018.

[103] M. Ernst, A. Fell, E. Franklin, and K. J. Weber, "Characterization of recombination properties and contact resistivity of laser-processed localized contacts from doped silicon nanoparticle ink and spin-on dopants," *IEEE Journal of Photovoltaics*, vol. 7, no. 2, pp. 471–478, 2017.

[104] J. Chen, Z. H. J. Tey, Z. R. Du, F. Lin, B. Hoex, and A. G. Aberle, "Investigation of screen-printed rear contacts for aluminum local back surface field silicon wafer solar cells," *IEEE Journal of Photovoltaics*, vol. 3, no. 2, pp. 690–696, 2013.